Coherent Soft X-Ray Magnetic Scattering and Lensless Imaging

vorgelegt von
Diplom-Physiker
Marcus Lörgen
aus Eschweiler

Von der Fakultät II - Mathematik- und Naturwissenschaften
der Technischen Universität Berlin
zur Erlangung des akademischen Grades
Doktor der Naturwissenschaften
Dr. rer. nat.

genehmigte Dissertation

Promotionsausschuss:

Vorsitzender: Prof. Dr. rer. nat. E. Sedlmayr
Berichter/Gutachter: Prof. Dr. rer. nat. Dr. h.c. W. Eberhardt
Berichter/Gutachter: Prof. Dr. rer. nat. P. Zimmermann

Termin der mündlichen Prüfung: 30.03.2004

Berlin 2004
D 83

Contents

Acronyms

AFM	Atomic Force Microscope or Microscopy
ER	Error Reduction algorithm
EUV	Extreme Ultraviolet
FIB	Focussed Ion Beam
HIO	Hybrid Input-Output algorithm
MFM	Magnetic Force Microscope or Microscopy
PLD	Path Length Difference
PSD	Power Spectral Density
SAS	Small Angle Scattering
SEM	Scanning Electron Microscope
STM	Scanning Tunneling Microscope
SXR	Soft X-Rays
TXM	Transmission X-ray Microscope or Microscopy
XMCD	X-ray Magnetic Circular Dichroism
XMLD	X-ray Magnetic Linear Dichroism
XPCS	X-ray Photon Correlation Spectroscopy
XUV	Extended Ultra-Violet radiation

Table 1: Acronyms used throughout the thesis in alphabetical order.

List of Symbols

Δs	Path length difference
$\hat{\mathbf{e}}, \hat{\mathbf{e}}'$	Initial and final polarization vector
θ	Grazing angle of incidence
θ'	Scattering angle
k	Wavenumber ($k = 2\pi/\lambda$)
λ	Wavelength
ξ_l	Longitudinal coherence length
ξ_{tr}	Transverse coherence length
p_I	Probability density of intensity I
$\mathbf{P}, \mathbf{P}'$	Initial and final STOKES vector of polarization
$\hat{\mathbf{q}}, \hat{\mathbf{q}}'$	Initial and final wavevector
$\Re$	Real part of complex number
$\Im$	Imaginary part of complex number
$\hat{\mathbf{U}}_i$	Unit vectors of the scattering geometry
Z	Atomic number

Table 2: List of mathematical symbols.

Abstract

The work presented here demonstrates the first imaging of ferromagnetic nanostructures that is obtained from their coherent soft X-ray scattering intensity pattern. This lensless imaging technique is performed in two steps: first, the coherent scattering pattern from the magnetic domain structure is recorded. Then, an established reconstruction procedure is applied to calculate the lateral structure of the magnetic domains from the scattering intensity.

The experimental setup simply consists of a set of pinholes to achieve coherent conditions of monochromatic soft X-rays and a detector that allows for the two-dimensional position resolving photon detection of the scattering pattern. Effort must be put into the preparation of the sample as well as into the provision of sufficient magnetic scattering intensity at the detector site. The magnetic $CoPt$ multilayers are sputtered onto a transparent SiN membrane to permit transmission geometry. The magnetic domains reveal an anisotropy that is perpendicular to the film surface. Further, the sample is laterally confined on a micrometer length scale to allow for coherent illumination. The magnetic small angle scattering is enhanced in intensity by exploiting the X-ray magnetic circular dichroism. The dichroism effect increases the contrast of oppositely magnetized domains that yields higher scattering intensity of magnetic origin. The energy and polarization dependence of the magnetic scattering pattern is investigated and appropiate results are shown in the thesis.

The feasibility of the reconstruction procedure is tested with a non-magnetic sample that consists of variously shaped apertures in a gold-film. From the diffraction pattern of the coherently illuminated sample its lateral structure is retrieved. Various experimental influences on a successful reconstruction like a beamblock applied to prevent radiation damage of the detector are investigated. The application of a reference hole in the sample plane simplifies the reconstruction and gives first hints of a possibly successful Fourier transform holography in the soft X-ray regime. Further, the lensless imaging of a magnetic domain test sample is performed to demonstrate the technique to be applicable to magnetic structures.

Finally, the recovering of the lateral domain structure of previously unknown magnetic sample is shown. The sample is consecutively exposed to external magnetic fields to demonstrate the domain reconfiguration after each exposure.

The lensless imaging technique presented could be used to increase the spatial resolution of established transmission X-ray microscopes. In principle, the spatial resolution in the scattering pattern can be increased by recording of high scattering angles. A combination of an microscopy image of the appropiate sample and the reconstruction procedure that uses a high angle scattering pattern as input could successfully enhance the resolution of the microscope image. Further, the lensless imaging technique works also with a scattering pattern that is acquired in a single shot of sufficiejt intensity as it will be provided by future free-electron laser sources. This could allow for time-resolved experiments that are not accessible to common microscopes.

Zusammenfassung

Die vorliegende Arbeit zeigt die erste Abbildung magnetischer Nanostrukturen, die aus dem Streuintensitätsmuster kohärenter weicher Röntgenstrahlung berechnet ist. Diese linsenlose Abbildungstechnik wird in zwei Schritten durchgeführt: erstens wird das kohärente Streumuster der magnetischen Domänenstruktur aufgenommen. Dann wird eine bereits erprobte Rekonstruktionsprozedur angewendet, um die laterale Struktur der magnetischen Domänen aus ihrer Streuintensität zu berechnen.

Der einfache experimentelle Aufbau besteht aus Lochblenden, um kohärente Bedingungen der monochromatischen weichen Röntgenstrahlung zu schaffen, und aus einem Detektor, der die zwei-dimensionale ortsauflösende Photonendetektion des Streumusters erlaubt. Sowohl die Präparation der Probe als auch das Erreichen einer ausreichenden magnetischen Streuintensität am Ort des Detektors erfordert einen großen Aufwand. Die magnetischen $CoPt$ Multilagen werden auf eine transparente SiN Membran aufgetragen und erlauben so eine Transmissionsgeometrie. Die magnetischen Domnen bilden eine Anisotropie aus, die senkrecht zur Filmoberfläche ausgerichtet ist. Ausserdem wird die Probe auf einer Mikrometer Längenskale lateral eingeschränkt, sodass sie kohärent ausgeleuchtet werden kann. Die magnetische Kleinwinkelstreuung wird in ihrer Intensität durch Ausnutzung des magnetischen Röntgen-Zirkulardichroismus verstärkt. Der Dichroismuseffekt erhöht den Kontrast gegensätzlich magnetisierter Domänen, was zu erhöhter Streuintensität führt, die ausschliesslich magnetischen Ursprungs ist. Die Energie- und Polarisationsabhängigkeit des magnetischen Streumusters wird untersucht und die entsprechenden Ergebnisse werden in dieser Arbeit präsentiert.

Die Machbarkeit der Rekonstruktionsprozedur wird anhand einer nichtmagnetischen Probe getestet, die aus unterschiedlich geformten Öffnungen in einem Goldfilm besteht. Aus dem Beugungsbild der kohährent ausgeleuchteten Probe wird die laterale Struktur wiederhergestellt. Verschiedene experimentelle Einflüsse auf eine erfolgreiche Rekonstruktion wie beispielsweise eine Blende, die Strahlenschäden am Detektor verhindert, werden untersucht. Die Verwendung einer Referenzöffnung in der Probenebene vereinfacht die Rekonstruktion und gibt erste Hinweise auf eine möglicherweise erfolgreiche Fourier-Transform-Holographie im Bereich weicher Röntgenstrahlung. Ausserdem wird die linsenlose Abbildung einer magnetischen Testprobe durchgeführt, um zu zeigen, dass diese Technik auch auf magnetische Strukturen anwendbar ist.

Schließlich wird die Wiederherstellung der lateralen Domänenstruktur von zuvor unbekannten magnetischen Proben gezeigt. Die Probe wird aufeinanderfolgend äußeren Magnetfeldern ausgesetzt, um jeweils die Umordnung der Domänen zu demonstrieren.

Die hier präsentierte linsenlose Abbildungstechnik könnte genutzt werden, um die Ortsauflösung von bestehenden Transmissionsröntgenmikroskopen zu erhöhen. Prinzipiell kann die lateral Auflösung im Streumuster durch Aufzeichnung hoher Streuwinkel erhöht werden. Eine Kombination eines Mikroskopbildes der entsprechenden Probe mit der Rekonstruktionsprozedur, die ein Streumuster mit großen Streuwinkel als Eingabe benutzt, könnte erfolgreich die Auflösung einer Mikroskopabbildung verbessern. Ausserdem funktioniert die linsenlose Abbildungstechnik auch mit Streubildern, die in einem einzigen Schuss genügender Intensität, wie ihn zukünftige Freie-Elektronen Laserquellen bereitstellen werden, aufgenommen wurden. Dies könnte zeitaufgelöste Experimente erlauben, die herkömmlichen Mikroskopen nicht zugänglich sind.

Introduction

The history of research on magnetism with synchrotron radiation is a story of full success over the last 15 years. Magnetism on one side is still subject to many research programs as many aspects are not fully understood. Synchrotron radiation on the other hand has found an important role for an increasing number of scientist during the last decades. The most striking feature of the (soft) X-ray regime of the synchrotron radiation is the ability to excite core electrons and, consequently, to allow for element specific experiments.

The discovery of soft X-ray resonant absorption dichroism of magnetic materials and the resonant scattering from magnetic structures propelled the investigation of magnetism with synchrotron radiation [1–17]. Spectroscopy and microscopy techniques for investigation of magnetic materials are established and build the basis for many advanced scientific investigations. The X-ray scattering technique is also subject to investigations since many years and the *coherent* scattering is of special interest in view of future free-electron laser sources that will provide coherent X-rays.

Coherent scattering of soft X-rays from magnetic materials is subject of this thesis. The magnetic scattering is caused by magnetic dichroism effects of oppositely magnetized domains. Coherent scattering pattern contain all information about the individual sample structure. Hence, correlation spectroscopy permits to investigate the dynamic properties of materials even if the sample is in thermodynamical equilibrium that prevents from fluctuation of the average properties of the sample. Another topic for coherent scattering is the objective to retrieve the sample structure from the scattering pattern. This lensless imaging technique is subject to a challenging race between different scientific workgroups in the synchrotron comunity.

Two fundamental aspects have to be considered for performing *lensless imaging* experiments on magnetic materials: coherent radiation and X-ray magnetic small angle scattering. The first two chapters are dedicated to these matters. The concept of coherence is introduced in chapter § 1.1. The quantitative definition of coherence and its statistical properties are presented. The difference between incoherent and coherent small angle scattering is explained and the crucial role of coherence for investigations beyond statistical information is stressed. Each topic is illustrated by own experimental results.

The fundamentals of resonant magnetic scattering are explained in chapter § 2. First an introduction to the magnetic scattering and its cross-section is given on an atomic level. It is known that magnetic scattering is very weak compared to non-magnetic charge scattering. In general, interference of charge and magnetic scattering enhances the magnetic signal [10]. This can be achieved in various ways. The favored possibility in this work is the *resonant magnetic* scattering process. The energy is chosen such that the $2p$-electrons of the magnetic element are excited. Dichroic effects permit to achieve a contrast between differently magnetized domains. This is where the step is done from the scattering on an atomic level to the small angle scattering (SAS) from an ensemble of magnetic moments that form domains on a nanometer length scale. The basic concepts of the scattering process concerning polarization and energy dependence are the same as on the atomic level. The influence of polarization on the scattering process and the resulting interference is introduced and an important result from experiments is presented (see § 2.5.1). The effect of energy variation of the incident coherent radiation across the $Co\ L_3$ absorption edge on the resulting interference pattern has also been investigated (see § 2.5.2).

The fundamental reconstruction procedure is introduced in chapter § 3 and a successful application to a test object consisting of an aperture pattern that is drilled into an opaque *Au*-film is demonstrated.

The last chapter § 4 contains the main results of this work: the first recovery of a magnetic structure on nanometer length scale from its coherent speckle pattern. The proof of principle is given using a known magnetic test sample. Finally, the concept is applied to *un*known magnetic objects. The magnetic structure is varied by external magnetic fields and the characteristic behavior of the magnetic domains are shown by analysis of the scattering pattern as well as reconstruction. The results are discussed concerning reliability and the limits of the reconstruction procedure. It is shown that for certain conditions a single inverse Fourier transform of the scattering intensity pattern rather than the application of the reconstruction procedure can be used to obtain the object. This is a hint of probably successful holography of nanoscale magnetic objects.

Chapter 1

Introduction to Coherent X-ray Scattering

1.1 Coherence

Generally, light sources do not provide coherent electromagnetic waves. That means interference experiments with light can only be performed using one light source and producing coherent waves from it. This is a well known process for visible light since some centuries. Fig. 1.1 shows a sketch of a coherence filtering process: a chaotic light source emits polychromatic waves with arbitrary phase relation. The resulting wavefront is disturbed (Fig. 1.1(a)). Collimating the size of the light source creates much sharper wavefronts of all wavelengths such that, transversely to a wavefront, a fixed phase relation can be assumed. This state is quantified by the *transverse coherence*, see Fig. 1.1(b). If a chromatic filter is applied to the light source only a small band of wavelengths remains, ideally only monochromatic light. The light source is made longitudinally coherent, see Fig. 1.1(c). A combination of both filtering processes yields spatially and longitudinally coherent light, see Fig. 1.1(d). From the schematic one can also see that the coherence filtering process occurs always at cost of the remaining photon flux. This is still an issue even for modern highly brilliant synchrotron radiation sources and many efforts are made since years to increase the overall coherent flux of x-rays sources.

Synchrotron radiation created at insertion devices such as undulators is also not perfectly coherent. Its small intrinsic degree of coherence is due comparably monochromatic light that is emitted from electrons in undulator devices [18]. The fundamental requirement for coherent wave sources is: the emitted waves must have the same wavelength and being in fixed phase relation the eachother. An electron emits the radiation tangential to its sinusoidal pathway through the undulator and, as a result, the synchrotron light emitted by the electron is amplified coherently. Usually, one or a few houndred groups of up to 10^{10} electrons, so called *bunches*, are accelerated through the storage ring. The electrons in each bunch do not emit coherently, nor the electrons of different bunches do. As a result, the synchrotron radiation has to be filtered spatially and temporally as shown above if a high degree of coherence is required in the experiment.

To consider the former conditions more quantitatively the longitudinal and transverse coherence lengths are introduced (see Fig. 1.2). Longitudinal or spectral coherence length is determined by the spectral resolution $E/\Delta E \propto \lambda/\Delta\lambda$. The longitudinal coherence length is proportional to the distance along the propagation direction over which two beams of different wavelengths ($\Delta\lambda$) acquire a phase shift of π,

$$\xi_l = \frac{\lambda^2}{2\Delta\lambda}. \tag{1.1}$$

For typical energy resolutions of synchrotron beamlines of about $E/\Delta E \approx 10^3..10^5$ the longitudinal coherence length for soft x-rays is in the range of $10^0..10^2 \mu m$. The longitudinal coherence limits the

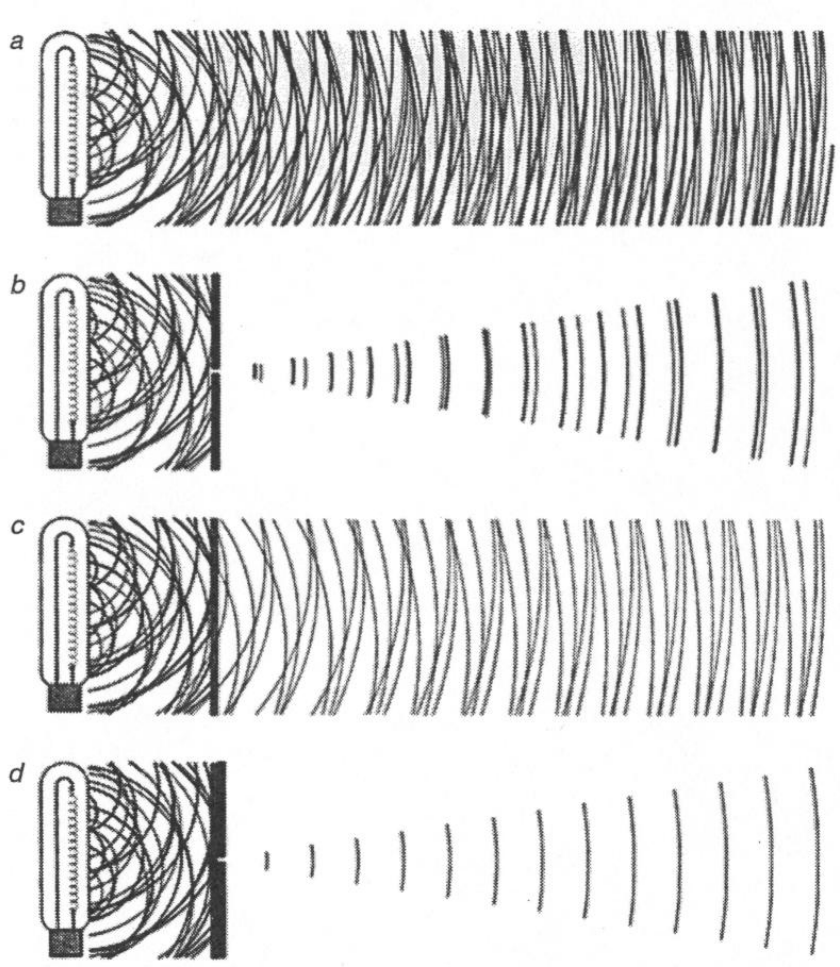

Figure 1.1: *a) Chaotic, polychromatic light source. b) Spatial filtering creates well-defined wavefronts of polychromatic light. c) Spectral filtering creates monochromatic light with distorted wavefronts. d) Both spatial and spectral filtering yields coherent light [18].*

maximum path length difference Δs_{max} that allows for interference of diffracted beams, hence, the maximum angle of diffraction θ' from a sample of size D perpendicular to the beam is also limited,

$$\Delta s = D \sin\theta' < \xi_l \tag{1.2}$$

Transverse coherence varies along the path of the waves and is measured perpendicular to that direction. Perfect transverse coherence would be achieved by a point source emitting perfectly correlated spherical wavefronts. Zero divergence is impossible due to the uncertainty, $\Delta\mathbf{k}\Delta\mathbf{x} \geq 1/2$ where $\Delta\mathbf{k}$ is the uncertainty in wavenumber and $\Delta\mathbf{x}$ is the uncertainty in position [18]. With $k = 2\pi/\lambda$ and assuming $\Delta\mathbf{k} = k\Delta\Theta$ that is true for $\Delta\mathbf{k}$ to be small, we get,

$$\Delta x \cdot k\Delta\Theta \geq \lambda/4\pi,$$

where $\Delta\Theta$ is the uncertainty of the divergence half angle Θ [18]. The diameter of the source is identified as $d = 2\Delta x$ yielding the relationship that determines the smallest source size for which the emitted wavefronts are correlated,

$$d \cdot \Theta = \lambda/2\pi. \tag{1.3}$$

The equation states that a certain source size d can only create perfectly correlation wavefronts of wavelength λ radiating into a half angle of Θ. Or, vice-versa, certain beam divergences of size Θ with a corresponding degree of correlation (or coherence) can only be enhanced by small apertures of size d that satisfies eqn. (1.3).

It is convenient to introduce a transverse coherence length, *i.e.* a lateral length over which the wavefronts are considered to be correlated. It depends on the distance L from the source,

$$\xi_{tr} = L\Theta = \frac{\lambda L}{2\pi d}. \tag{1.4}$$

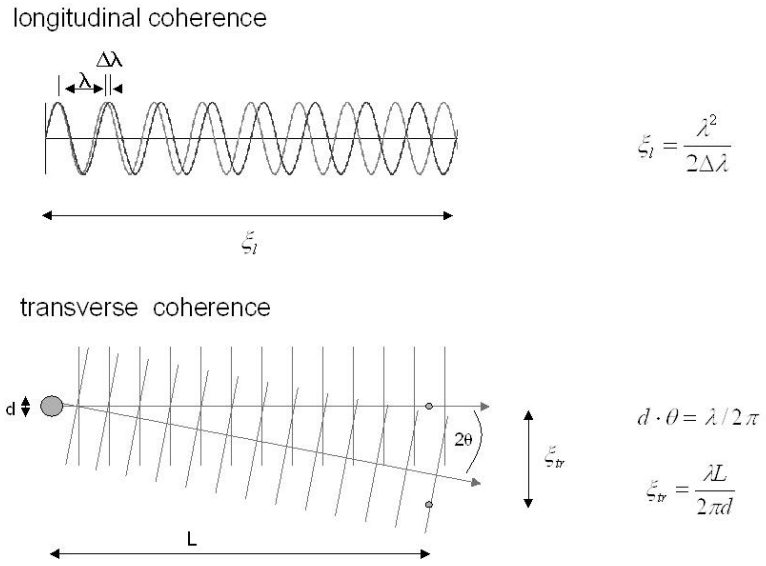

Figure 1.2: *Illustration of longitudinal and transverse coherence length.*

The longitudinal coherence length is a measure of the monochromaticity of the light source. Hence, it is a parameter of the light source alone. The transverse coherence length can only be determined by the complete experimental setup. The source confining pinhole must be chosen appropriately in size and sample distance. Various beamline or experiment devices like mirrors or detectors can destroy the coherence. A further important coherence parameter is the *degeneracy parameter* Δ_c. It is defined as the number of photons in the coherence volume $V_c = A_t \xi_l$, where A_t is the transverse coherence area spanned by two orthogonal directions of the spatial coherence length ξ_{tr}. Δ_c is connected to the brilliance Br as $\Delta_c = Br\lambda^3/\pi c$. Typically, a HeNe laser has about 10^7 photons per coherence volume whereas undulators contain about 10^{-3} coherent photons although the overall photon flux of typical undulators is about $10^{12}/s$ [19]. *I.e.* the flux is reduced dramatically for coherent photons. The relation of the overall flux in the center cone of the undulator to the *coherent* flux obtained by spatial and spectral filtering can be expressed as [18]:

$$P_{coh} \propto \underbrace{\frac{(\lambda/2\pi)^2}{(d_x\Theta_x)(d_y\Theta_y)}}_{\text{spatial filtering}} \cdot \underbrace{N\frac{\Delta\lambda}{\lambda}}_{\text{spectral filtering}} \cdot P_{cen}, \tag{1.5}$$

where the proportionality is given by the beamline efficiency, describing the total intensity loss due to optical elements (typical value: 10%). d_x and d_y are the horizontal and vertical pinhole diameters, respectively, and Θ_x, Θ_y give the corresponding beam divergences.

1.1.1 Experimental geometry

Before the results and experimental examples are presented it might be convenient to explain in general the experimental setup which is mainly the same for all experiments shown throughout the work. All experiments are performed in transmission geometry, *i.e.* the angle of incident of the soft x-rays is perpendicular to the sample surface. Fig. 1.3 shows a sketch of the setup. The synchrotron radiation is incident from the left - in general, it is incoherent but monochromatic within a certain energy resolution. A setup of several apertures follows that either acts as a spatial coherence filter or as guard holes blocking stray light. For coherent illumination of the sample the illuminated area D must be smaller than the coherent area spanned by the transverse coherence lengths. The soft x-rays are scattered by the sample structures under a scattering angle θ' performing small angle scattering (SAS) (see § 2.4). A position sensitive detector (either a micro-channel plate detector or a charge-coupled device) is placed downstream the sample at a distance L (for details about the detectors see § C). The exact setup is explained at the distinct experimental section of the work and the pinholes are referred to as "upstream" or "downstream" pinhole and "guard" hole.

1.1.2 Dual Pinhole - A Coherence Gauge

In most cases, loss in intensity is critical. Every optical element between the light source and the sample reduces the overall flux and last but not least, flux reduction is inevitable, virtually necessary, to increase coherence. During the construction phase of beamline UE56-1 SGM at BESSY II we had the opportunity to measure the coherence of the UE56-1 undulator without any beamline elements. The only optical elements between the undulator and the experimental setup are two pairs of baffles at 13.3 m downstream the undulator and a torroidal mirror at 17 m (see Fig. C.1 in § C.1). At 25 m downstream of the undulator we illuminated a double pinhole with x-rays of 400 eV energy of the 1st undulator harmonic (Fig. 1.4). Each pinhole has a diameter of about $d = 2\ \mu m$ and the pinholes are separated by $D = 10\ \mu m$. The intensity pattern is analytically known and can be used to determine the coherence length of the incident radiation [20], see § A. At 260 mm upstream of the dual pinhole a guard hole of 50 μm diameter is installed (see Fig. 1.3). The natural bandwidth of the undulator's center cone is

$$\frac{\Delta\lambda}{\lambda} = \frac{1}{iN}, \tag{1.6}$$

where N is the number of magnet periods and i is the order of the undulator harmonics [18]. The bandwidth yields $\Delta\lambda/\lambda = 1/30$ for the first harmonic of the $UE56-1$ undulator. Hence, the longitudinal

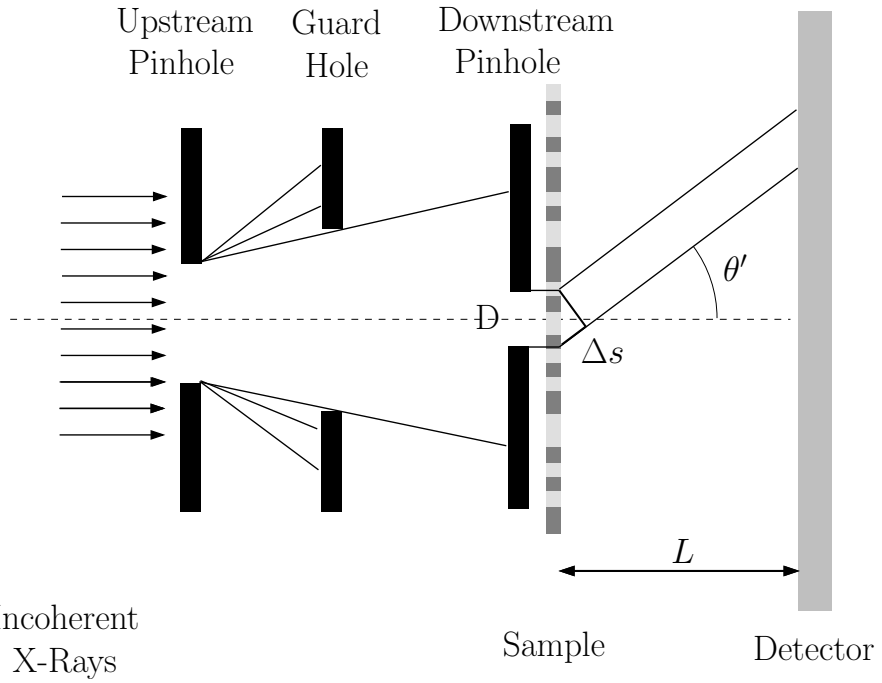

Figure 1.3: *General setup for transmission geometry. Incoherent light is collimated by a set of the upstream pinhole and the downstream pinhole. The sample is illuminated in a region of size D, where D for some experiments is defined by the downstream pinhole. For the reconstruction experiments explained in § 4 the downstream pinhole is attached to the sample and consists of two neighbouring holes. The guard hole is applied for some experiments to surpress higher diffraction orders created by the upstream pinhole. The scattering intensity is recorded by a detector where the scattering angle is* θ_s*. Both parameters D and* θ_s *determine the path length difference* Δs *of the scattered waves.*

coherence length is calculated by setting eqn. (1.6) into eqn. (1.1) and is as small as 46 nm. The central cone of half angle is $\Theta_{cen} \approx 145\ \mu rad$[1].

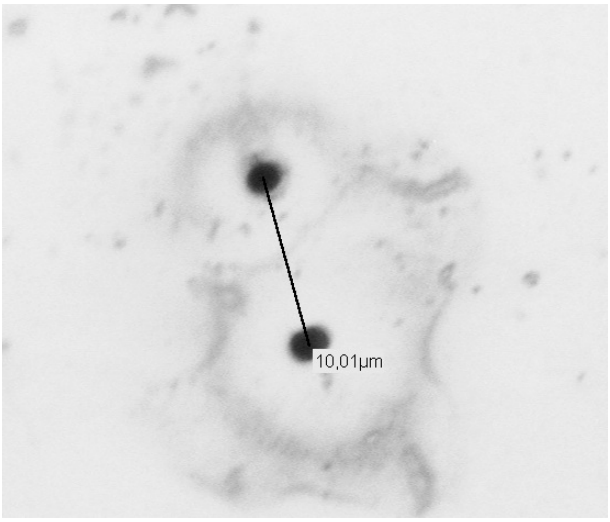

Figure 1.4: *Optical microscope image of the dual pinhole.*

We closed the baffles located 13.3 m downstream the undulator source to 50 $\mu m\ \times 50\ \mu m$, thus, decreasing the acceptance angle for the central cone to $\Theta_b \approx 2\ \mu rad$. The baffles define the size of the source and the half angle $\Theta = \lambda/2\pi/d = 3.1\ nm/2\pi/50\ \mu m = 10\ \mu rad$ of coherent illumination. The upstream 50 μm guard pinhole does not affect the coherence length because it does not shrink the product $d \cdot \Theta$ [18] and it is just installed to reduce stray light. Hence, the transverse coherence length is $\xi_{tr} = L\Theta = 11.7\ m \cdot 10\ \mu rad = 117\ \mu m$.

Fig. 1.5 shows the resulting 2D diffraction pattern (inset) and a line profile of the double pinhole setup illuminated by undulator radiation alone. The detector is placed 660 mm downstream of the dual pinhole. The line profile is taken offset from the center (white line in diffraction pattern shown in the inset) because of a hot spot[2] close to the center of the diffraction pattern. The visibility $V \approx 0.3$ measured as the normalized difference in intensity of the maxima and minima $(I_{max}-I_{min})/(I_{max}+I_{min})$ of the high frequency interference pattern is comparably low in the center and additionally decreasing to $V \approx 0.2$ towards higher momentum transfer. The reason is the low longitudinal coherence ξ_l. For each single wavelength the diffraction pattern is almost perfect due to a relatively large spatial coherence in comparison to the dual pinhole dimensions. The spectral bandwidth of the undulator causes many superposed dual pinhole diffraction patterns each with a slightly different angular separation of the intensity maxima and minima. This smears out the resulting diffraction pattern. The fact that the visibility is decreasing towards high momentum transfer demonstrates the influence of finite longitudinal coherence. It limits the maximum path length difference for which two waves diffracted from one of the two pinholes can interfere. Thus, the higher the diffraction angle the less interference is observed. The separation of the two pinholes $D = 10\ \mu m$ and the definition of the path length difference in eqn. (1.2) yield a maximum momentum transfer of $q^{max} = 2\pi/\lambda sin(\theta_s) \approx 10\ \mu m^{-1}$ which still allows interference.

[1]The central cone half angle is calculated by [18]:

$$\Theta_{cen} = \frac{(1 + K^2/2)^{1/2}}{\gamma\sqrt{iN}}$$

where $K = 3.2$ is magnetic strength for the UE56/1 undulator, $\gamma = 1957E_e(= 1.7\ GeV) = 3330$. The emittance of the electron beam is considered but comparably small with beam divergences of $\sigma_x = 22\mu rad$ horizontally and $\sigma_y = 5\mu rad$ vertically.

[2]A so called *hot spot* is produced by erroneously induced electron transitions in the micro-channel plates. Usually high voltage flashes in broken channels create these electron cascades.

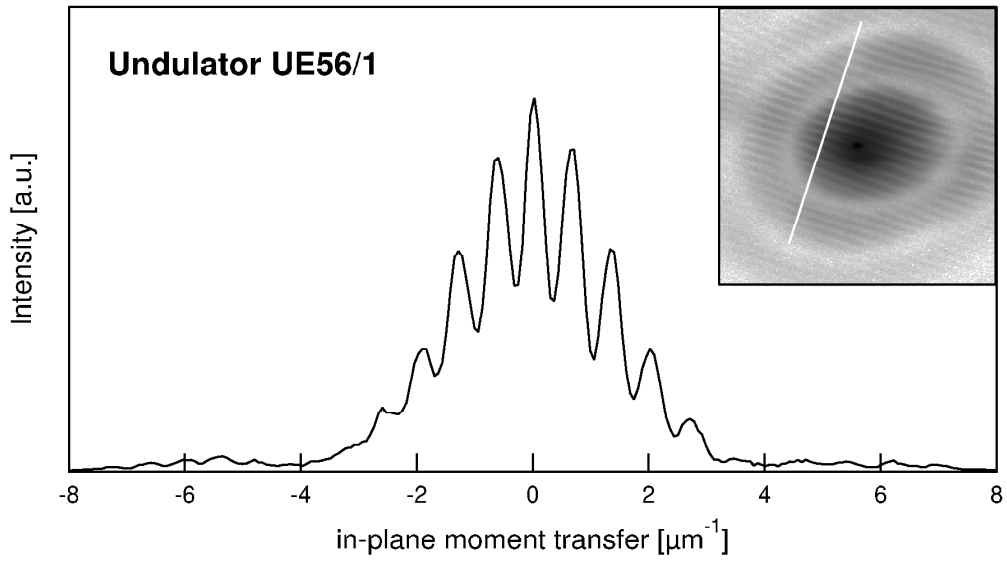

Figure 1.5: *Line profile of the diffraction pattern obtained from the dual pinhole sample that is illuminated with direct undulator radiation. The line profile is cut off-center because some transmission of the direct undulator beam through the pinhole plate occurs and disturbs the diffraction pattern. The inset shows the two-dimensional diffraction pattern from the dual pinhole plotted in logarithmic scale for an in-plane momentum transfer of* -10 μm *to* 10 μm *in both axes.*

We repeated the experiment after the complete UE56/1 SGM beamline was constructed. The optical layout of the beamline is presented in § C.1. The same dual pinhole and the 50 μm guard pinhole are exposed to the monochromatic X-rays but due to a different experimental setup the guard hole is located 723 mm upstream of the dual pinhole. The experimental chamber is located about $L_s = 8$ m downstream the exit slit of the monochromator which itself is located 33.5 m downstream the undulator source. The exit-slit is opened to $d_s = 20$ μm vertically. In horizontal direction the beam is not confined by the exit slit and the width of the beam is determined by the horizontal focussing switching mirror unit (SMU) placed 17 m downstream of the undulator (see § C.1). The focal plane of the switching mirror is 37 m downstream of the undulator, *i.e.* the focus is $L_f = 4.5$ m in front of the experimental station. The horizontal divergence of the beam is $\Theta_{SMU} = 64$ μrad. The corresponding coherence length at the dual pinhole site are: $\xi^h_{tr} = L_f \Theta_{SMU} = 288$ μm and $\xi^v_{tr} = \lambda L_s / 2\pi d_s = 190$ μm.

In the monochromator we use a 800 $lines/mm$ grating with entrance slit opened to 70 μm, *i.e.* accepting the full beam height of 30 μm at the entrance slit, and the exit slit set to 20 μm. The corresponding energy resolution is $E/\Delta E = 5900$ (cp. § C) yielding a longitudinal coherence length of $\xi_l = \lambda/2 \cdot 5900 = 9$ μm. This is large enough to ensure that the interference is not limited by finite spectral coherence. For 10 μm lateral separation of the two pinholes $\xi_l = 9$ μm implies a maximum angle for coherent scattering of $\theta' = 64°$ (see eqn. (1.2)). This exceeds the angular acceptance in the experimental setup.

In Fig. 1.6(a) the diffraction pattern from the dual pinhole is plotted. The center line of the pinholes is oriented vertically. Again, the visibility is calculated from line profiles for the central maximum and the maximum of $1st$ order (see Fig. 1.6(b)). The visibility is $V_v = 0.26$ for the central maximum.

The main difference between the direct undulator beam and the complete beamline setup is that the longitudinal coherence length is increased due to the monochromator. This allows for interference up to high diffraction angles. The transverse coherence length is almost the same for both experiments. The

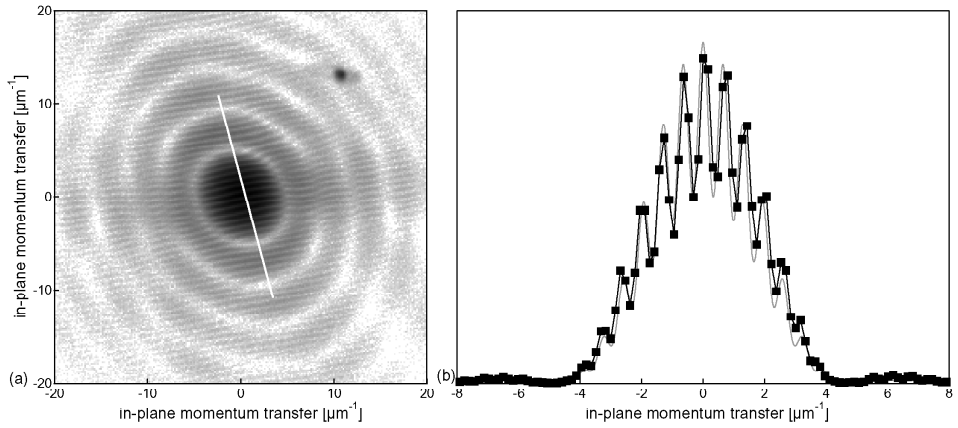

Figure 1.6: *(a) Two dimensional diffraction image of a dual pinhole plotted in logarithmic intensity scale. The center line of the two apertures is vertically oriented. The blob in the image is a hot-spot of the micro-channel plate detector where the channels erroneously induce electron transitions into the resistive anode.(b) A line profile cut through the diffraction pattern (black line and markers). The gray line shows the analytical diffraction pattern for a double pinhole convolved with the detector resolution.*

coherence volume V_c is much bigger for the experiment with the complete beamline setup, merely due to the increased monochromaticity. Nevertheless, the visibility of the diffraction images from the double pinhole is not enhanced in the "beamline" experiment. The reason is the limited spatial resolution of the detector. Its spatial resolution is 100 μm. A simulation of the one-dimensional diffraction pattern according to eqn. (A.4) in § A for perfect coherence. The limited spatial resolution of the detector is simulated by convolving the result with the resolution as shown in Fig. 1.6(b) (gray line). The spatial resolution causes the visibility of the diffraction pattern to be reduced dramatically. As a consequence, it is difficult to distinguish between low resolution or small coherence length causing the visibility to be low.

In a next step, we substitute the *micro-channel plate* detector by a *charge-coupled device* (CCD) camera of 13.5 μm pixel size. It is located 315 mm downstream from the dual pinhole. Again, the vertical coherence length is $\xi_{tr}^{v} = 190\ \mu m$. A profile of the resulting diffraction pattern is plotted in Fig. 1.7. Obviously, the visibility is much higher this time and is determined to be $V = 0.65$.

1.1.3 General remarks

Interference - In general, interference phenomena are observable if there are indistinguishable paths causing the interference pattern. For observation of interference from a double slit (or pinhole) it is crucial that the observer is not able to tell whether the photon passes through one or the other slit or pinhole. As soon as the path through the dual aperture setup is known, *i.e.* one can distinguish the path through one of the two apertures from that through the other one, the interference is destroyed. This well known general quantummechanical concept must be kept in mind while performing and understanding coherence experiments.

Magnetism - Ferromagnetism of the $3d$ transition metals Cr, Mn, Fe, Co, Ni and $4f$ rare earth elements is the basis for many technical and scientific purposes. Any magnetic compound contains at least one of the above elements. The fundamental of ferromagnetism is of pure quantummechanical nature. It is based on the electrostatic Coulomb interaction and the Pauli principle. The Pauli principle prevents the electrons from occupying the same state. Hence, the repelling Coulomb potential is weaker for parallel arranged electron spins because the average distance of the electrons is larger than for

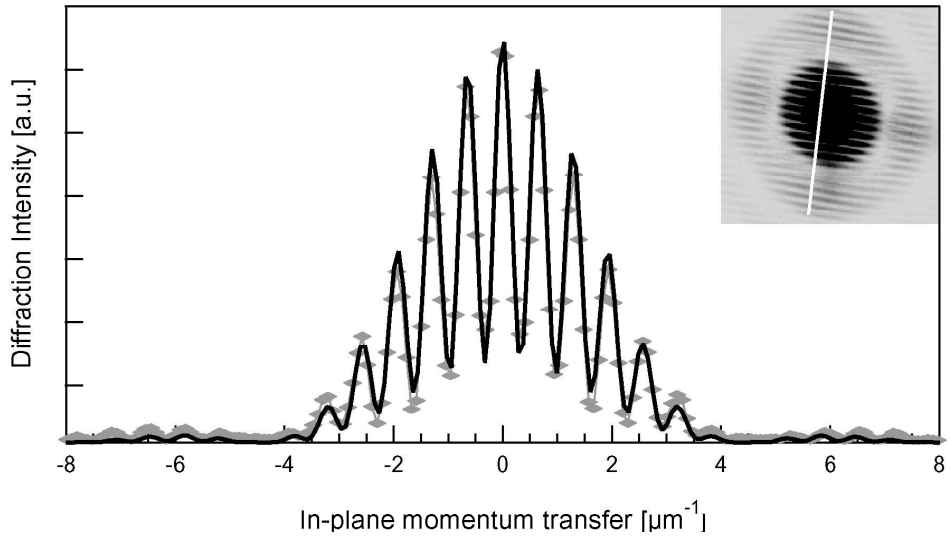

Figure 1.7: *Line profile of the diffraction pattern from the double pinhole recorded with CCD-camera of* 13.5 *μm pixel size (gray dots). The black line is a fit of eqn. A.4 to the data. The inset shows the corresponding CCD-image. Both axes are plotted between* $-8\ \mu m^{-1}$ *and* $+8\ \mu m^{-1}$*. The high-frequency interference lines of the two pinholes are clearly visible. The visibility is* $V = 0.65$*.*

antiparallel spins due to the Pauli principle. As long as the lowering of the Coulomb energy under consideration of the Pauli principle can be achieved by parallel spin orientation, free atoms with partially filled shells show spontaneous magnetization.

This also favors the parallel arrangement of electron spins in condensed matter systems which gives raise to ferromagnetism. If the lowering of the Coulomb energy were the only criterion every metal system would show ferromagnetic properties. Parallel spins force the electrons to occupy higher energy levels. As the delocalized electrons in $3d$ valence bands of transition metals are no longer bound to the ion potential, they gain kinetic energy upon shift to high energy levels. As a consequence, the ferromagnetic order is only favored if the lowering of the Coulomb energy is not compensated by the gain in kinetic energy. Ordered states are preferred for systems with small bands at the Fermi level, *i.e.* the density of states at the Fermi level $n(E_F)$ is large for these bands. This is expressed in the Stoner criterion for ferromagnetic order:

$$n(E_F)I \geq 1.$$

I is the Stoner parameter. Qualitative conditions for ferromagnetic order are:

- The exchange energie must be positive and maximized, *i.e.* $I > 0$.
- High density of states reduce the work upon enhancement of kinetic energy and favor ferromagnetic order.

The ordering of the electron spins in parallel states for ferromagnets is called spin polarization. This yield a difference in number of electrons with the same spin state. Consequently, the density of states of ferromagnetic crystals is different for spin-up and spin-down electrons. Accordingly, the electrons are classified in majority and minority spins.

The most important effect that is exploited in the magnetic scattering experiments is the magnetic dichroism for polarized X-rays. The dichroic property is based on the polarization dependence of absorption of photons over a wide range of the electromagnetic spectrum. Especially, soft X-rays allow for resonant core-electron excitation and can force helicity-dependent transitions from spin-orbit splitted

core levels to spin-dependent d valence bands of *e.g.* ferromagnets. The magnetic samples considered here are compounds containing ferromagnetic Co. This $3d$ metal has a spin-orbit splitted $2p$ core level. The $3d$ valence band has a different density of states for spin-up and spin-down electrons - a consequence of the exchange interaction of the valence electrons. These are the two main properties which explain the magnetic dichroism of circular polarized X-rays (XMCD). The absorption of the photons by $2p$ electrons depends on the photon-helicity. This excitation causes spin-polarized electrons because for a certain helicity it is more probable to excite one kind of electrons, either spin-up or spin-down. For example, for the Co $2p_{3/2}$ level the absorption cross-section of right circular polarized photons is higher for spin-up electrons than for spin-down electrons. As the $3d$ band is exchange-splitted the densities of states have different occupation for spin-up and spin-down electrons. The states (holes) above the Fermi level are also spin-selective and, hence, cause different transition probabilities for spin-up and spin-down electrons. Finally, the magnetic dichroism effect for circular polarized photons can be explained in a two step model: the $2p$ core electrons are excited with spin-dependent probabilities and undergo transitions into unoccupied final states according to the spin-selective probability. Both steps together give raise to a difference in X-ray absorption that depends on the helicity and the direction of the magnetization.

Hence, magnetic domains of opposite magnetization cause different dichroism strength for fix helicity of the absorbed photons. This difference can be exploited to achieve a contrast between differently magnetized domains. It has been used in spectro-microscopy as well as in resonant small angle scattering experiments. The scattering of *coherent* soft X-rays from magnetic materials is subject of this thesis. It is used to obtain the structural information of magnetic samples. The lensless imaging technique is introduced that only requires scattering information from the magnetic objects. The scattering intensity is acquired in two dimensions and algorithmic procedures allow to retrieve the lateral magnetic structure.

Samples - Before going on it is helpful to present the type of samples that are investigated throughout this work. The experiments were mainly done in transmission geometry with a sample of a magnetic anisotropy that is perpendicular to the sample surface. This outstanding magnetic property is obtained by multilayer systems. The static energy of the systems is minimized by forming oppositely magnetized domains and the average domain width depends on the thickness of the layers. The details about these samples are described in § B. A transmission X-ray microscope (TXM) image is shown in Fig. 1.8. The average width a of the domains causes a small angle scattering (SAS) maximum corresponding to a momentum transfer of $q = 2\pi/a$ (cp. § 2.4). As the domains are oriented randomly in 2 dimensions, *i.e.* every direction occurs equivalently, the scattering pattern of the domains is circular (cp. § 1.1.4 and § 2.5).

1.1.4 Incoherent Scattering versus Coherent Scattering

Fig. 1.9 illustrates the difference between incoherent and coherent small angle scattering (SAS) from a sample with characteristic structures of a certain correlation length (Fig. 1.8). In the experiment sketched in Fig. 1.9 (a) the transverse coherence length of the setup is appropriate for the size of the sample structures but it is smaller than the illuminated area. Hence, common incoherent small angle scattering can be observed (line profile and image). Statistical properties of the sample can be obtained from the scattered intensity, *e.g.* the average period of the black and white structures in a certain direction of the sample corresponds to the circular minor maximum in the scattering image. The image (b) below shows the coherent case. The coherence length is increased to at least the illuminated sample area. This time, constructive and destructive interference occurs from the structures of the *completely* illuminated sample and causes bright and dark intensities on the detector, also known as *speckle*. The scattered intensity provides information about the individual sample configuration (see Fig. 1.10). Objects with same statistical properties but a different structure cause a different speckle pattern. Due to the ability of the scattered waves to interfere, the exact location of the scattering centers with respect to its environment is crucial. If the individual arrangement changes the phase relations of the scattered waves change also.

Fig. 1.11 shows a measurement of this important property. The scattering of soft X-rays from a coherently illuminated magnetic domain pattern is shown (for image of the pattern see Fig. 1.8). From left to right the illuminated area changes. Hence, the sample structure that is illuminated changes and,

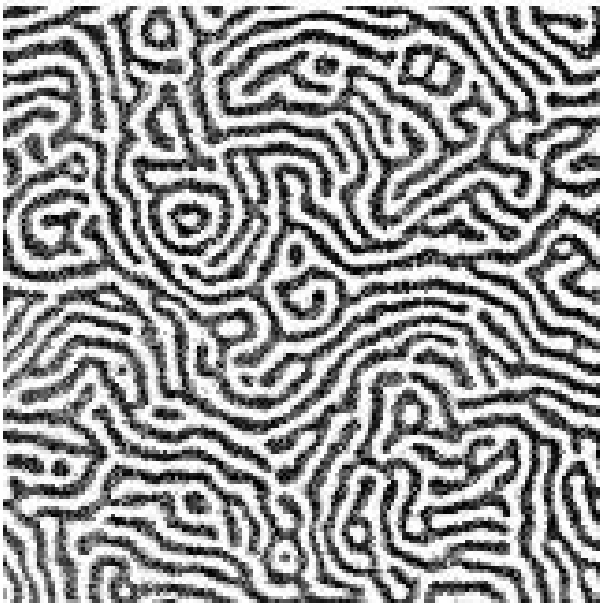

Figure 1.8: *Transmission X-ray Microscope (TXM) image of the CoPt multilayer magnetic domains (size: 5 $\mu m \times 5$ μm). The domains are encoded in white and black color indicating perpendicular magnetization of opposite direction. (Courtesy of G. Denbeaux at ALS, Berkeley, USA [21])*

consequently, a different speckle pattern is observed. The characteristic circular pattern corresponds to the period of domain structures causing small angle scattering (SAS). It would be also visible with incoherent light (see Fig. 1.9). But the interference of coherent waves causes the circular pattern to be modulated by the individual domain structure.

This important property of coherent X-ray scattering can be exploited in the spatial and temporal domain. From the scattered intensity the real space structure can be obtained by phase retrieval using an iterative algorithm or holographic techniques. The speckle pattern itself can also be used as a "fingerprint" of the sample, *i.e.* without retrieving the real space image. The dynamics of the sample can then be monitored by measuring fluctuations in the speckle pattern. Structural resolution can be obtained by confining the scattering angle for which the fluctuations are measured and that corresponds to a certain structure size of interest. This is the basis for a technique known as x-ray photon correlation spectroscopy (XPCS).

1.2 Analysis of Coherent Diffraction

Speckle pattern generated by coherent scattering can be described quantitatively regarding their statistical properties, temporal and spatial correlation and contrast. The relation between these properties is described in this section.

1.2.1 Speckle Statistics

The speckle pattern results from constructive and destructive interference of waves from all scattering centers of a sample. Thus, the distribution of field strengths is supposed to be Gaussian [22–24]. The statistical properties of this particular distribution is described by the probability density function of the intensity I [22]:

$$p_1(I) = 1/\langle I \rangle exp\left(-\frac{I}{\langle I \rangle}\right). \tag{1.7}$$

The probability density function of normalized intensities can be extracted from a speckle pattern by determing the histogram of intensities (see fig. 1.12). The high number of zero-intensity indicates the

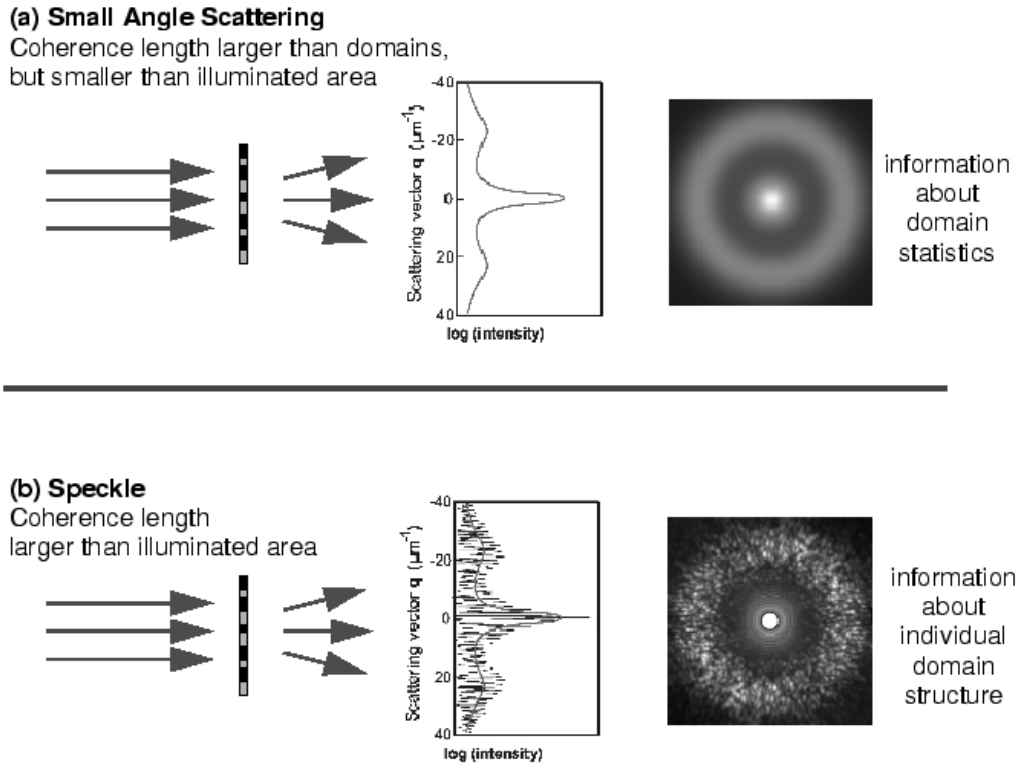

Figure 1.9: *Incoherent versus coherent small angle scattering. (a) The transverse coherence length of the incoming light is smaller than the illuminated area but larger than the correlation length of the characteristic structure within the sample. Conventional small angle scattering occurs. The right image shown is obtained simulation. (c): Increasing coherence length to at least the size of the illuminated area causes the formation of a speckle pattern. The right scattering image shows a simulation.*

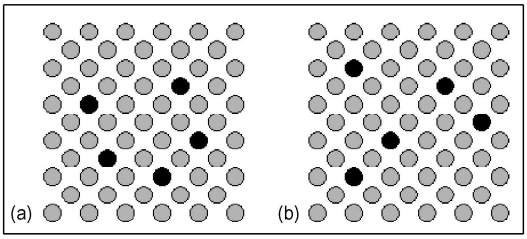

Figure 1.10: *Two sketches of a regular matrix (gray circles) with different disturbances (black circles) but same statistical properties. Coherent scattering experiments can distinguish both configurations.*

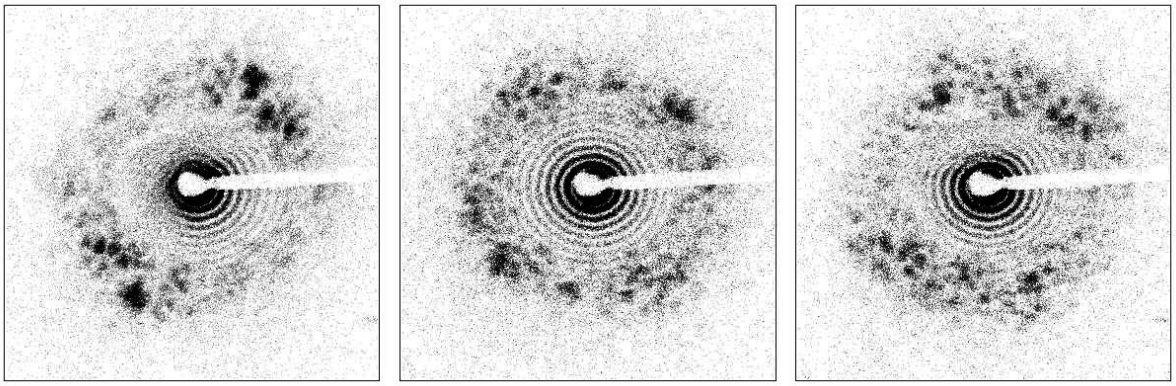

Figure 1.11: *Measured speckle pattern from a wormlike magnetic domain pattern (see § 1.8) of a CoPt multilayer. Every image shows the characteristic circular scattering corresponding to the average domain period of approximately* 200 μm *which also would be measurable with incoherent soft X-rays. The in-plane momentum transfer is* $q = -45\ \mu m$ *to* $q = 45\ \mu m$ *for the horizontal and vertical axis of each image. With coherent illumination the diffraction pattern is modulated and characteristic for the individual domain pattern. For each image a different area of the magnetic domains was illuminated to demonstrate the effect of a "fingerprint".*

perfect destructive interference of coherently illuminated objects. For partial coherent illumination the coherence volume is smaller than the illuminated volume. The ratio M of both numbers gives the number of independent speckle pattern each with perfect coherent illumination. The incoherent sum of the M patterns yields the partial coherent intensity distribution. The probability density functions p_j are multiplied to [22]:

$$p_M(I) = \frac{M^M (I/\langle I\rangle)^{M-1} exp\left(-\frac{MI}{\langle I\rangle}\right)}{\Gamma(M)\langle I\rangle}. \tag{1.8}$$

where $\Gamma(M)$ is a gamma function of M which itself is the only fitting parameter in eqn. (1.8).

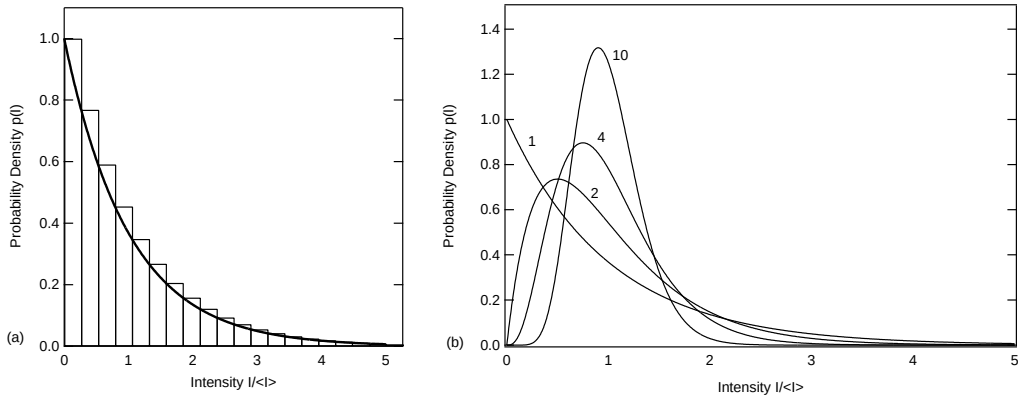

Figure 1.12: *(a) Plot of probability density function in terms of normalized intensities* $\langle I\rangle$ *(solid line). The bars show an idealized histogram of intensities as it would be obtained by perfect coherent illumination. (b) Plot of eqn. (1.8) for different values of* M*.*

Measurements of coherent scattering from rough surfaces in reflection geometry reveal a high sensitivity of the speckle pattern to the surface topology [16, 22, 25–27]. As an example to illustrate the statistical properties of a speckle pattern the scattering from a *CoPt* multilayer was recorded (see Fig. 1.13(a)). The histogram of intensities from the indicated region (black box) is shown in Fig. 1.13(b).

It is very similar to the distribution with $M = 1$, *i.e.* the sample is illuminated with almost perfect coherence. From a fit of eqn. (1.8) the parameter is determined to be $M = 1.15$. The solid line in the figure shows the fit to the histogram. The value of the visibility of the pattern inside the black box is $V = (I_{max} - I_{min})/(I_{max} + I_{min}) = 0.9$.

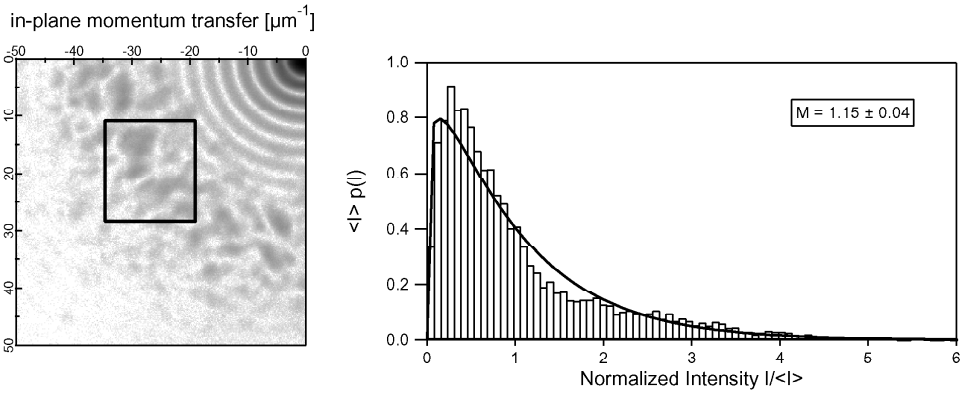

Figure 1.13: *(a) Speckle pattern of CoPt multilayer. The color scale is logarithmic. (b) Histogram of normalized intensities in terms of $\langle I \rangle$ of Soft X-ray scattering pattern from the CoPt multiplayer. The solid line is a fit of eqn. (1.8) to the histogram with parameter $M = 1.15$.*

The standard deviation of the intensities is $\sigma_I^2 = \langle I^2 \rangle - \langle I \rangle^2$ and the contrast of speckle intensities may be defined as [22]

$$C = \frac{\sigma_I}{\langle I \rangle}. \tag{1.9}$$

For perfect coherence the contrast in the speckle pattern is always unity [22]. Of course, the signal-to-noise ratio of the Speckle pattern influences the contrast. High incoherent background smears out the contrast of maximum and minimum intensity and it is found to be [22],

$$C = \frac{\sqrt{1+2r}}{1+r}, \tag{1.10}$$

where $r = I_B/\langle I \rangle$ is the ratio of the background intensity to the mean Speckle intensity (see Fig. 1.14).

Goodman derived an expression for M that results in a contrast definition in terms of the coherence parameter M [22]:

$$C = \left(\frac{1}{M}\right)^{1/2}. \tag{1.11}$$

This allows to determine the contrast of a speckle pattern by statistical analysis of the measured intensities.

An example of contrast measurement: The determination of the contrast of a speckle pattern obtained by coherent scattering from a ferromagnetic $CoPt$ multilayer system (see § B) is demonstrated next. The characteristic magnetic domain pattern of $CoPt$ causes a distinct scattering pattern similar to that shown in Fig. 1.11 or in § 2.5.1. The experimental details are also described in § 2.5.1. From the complete two-dimensional scattering image obtained from the position sensitive detector a sub-image is extracted called q-box. The in-plane momentum transfer covered by the box is $\Delta q = 5.7\ \mu m^{-1}$ in radial direction. Transversely the momentum transfer is almost constant and does not depend strongly on the size of the box. The intensity in the q-box is used to evaluate the contrast by applying eqn. (1.9). In radial direction the q-box is moved to get the q-dependence of the contrast as it is plotted in the upper

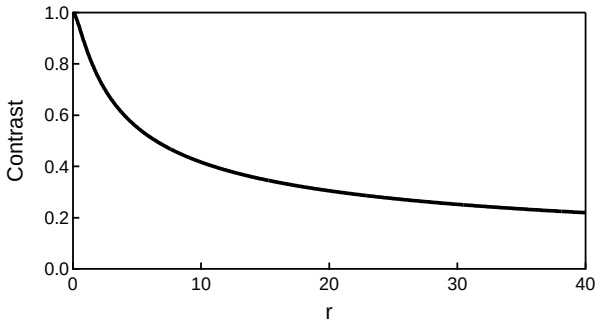

Figure 1.14: *Contrast as function of ratio of the background intensity to mean Speckle intensity concerning eqn. (1.10).*

graph of Fig. 1.15. The error bars indicate the size of the q-box in radial direction. The area of the box is chosen to cover four times the average area of a single speckle. The contrast rises from an initial level of $C = 0.4$ to an average of $C = 0.7$ for $q \in [27\ \mu m^{-1}, 33\ \mu m^{-1}]$. For higher momentum transfer, *i.e.* beyond the large magnetic scattering, the contrast is lowered again to values around $C = 0.4$. This observation is consistent with the variation of the scattering intensity relative to a constant background as described by eqn. (1.10).

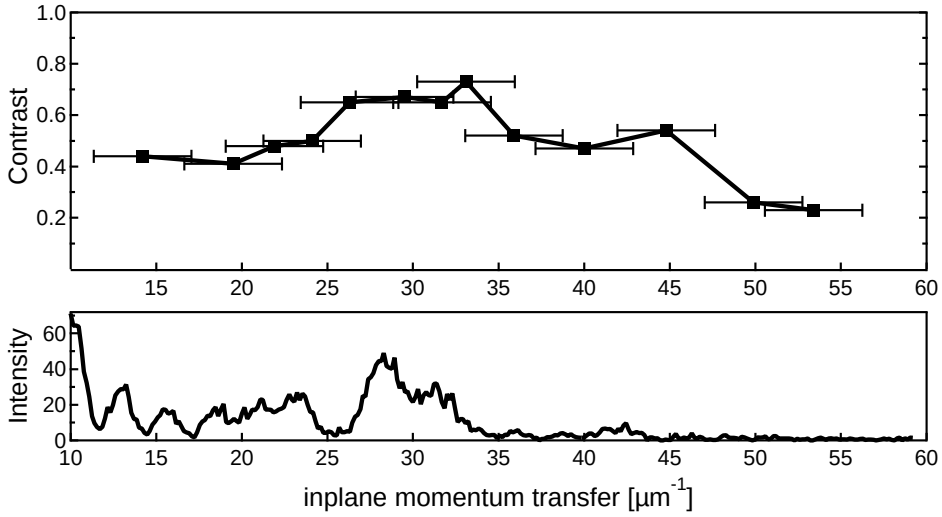

Figure 1.15: *Contrast of a CoPt magnetic multilayer scattering pattern illuminated under coherent conditions. The contrast is evaluated in a q-box of* 5.7 μm^{-1} *radial length across the detector image and plotted against the momentum transfer in the center of the corresponding box. The size of the box is chosen to contain a fourfold area of the average speckle size and indicated by the horizontal error bars in the upper graph. The lower graph is a cross-section through the Speckle pattern along the radial direction of the contrast value being taken. Up to* 15 μm^{-1} *a few pinhole diffraction rings are visible. Between* 20 μm^{-1} *and* 40 μm^{-1} *the scattering pattern from the magnetic domains is present. For high momentum transfer the background intensity becomes dominant.*

1.2.2 Intensity Correlation of Partially Coherent Scattering

The speckle pattern is the result of interference of all waves scattered in the object plane after propagation to the observation plane. Hence, the amplitudes or intensities of two points O and P in the observation plane are correlated to each other and to the waves originating in the object plane. The

correlation of the amplitudes of the two points at the same time t_0 is expressed by the normalized first-order correlation function [18, 19, 22]

$$g^{(1)}(\mathbf{r}_O, \mathbf{r}_P, t_0) = \frac{\langle E^*(\mathbf{r}_O, t_0) E(\mathbf{r}_P, t_0)\rangle}{\{\langle |E(\mathbf{r}_O, t_0)|^2\rangle \langle |E(\mathbf{r}_P, t_0)|^2\rangle\}^{1/2}}. \tag{1.12}$$

Intensities rather than amplitudes are accessible in experiments. The second-order correlation function consideres this

$$g^{(2)}(\Delta r) = \frac{\langle I(\mathbf{r}, t_0) I(\mathbf{r} + \delta\mathbf{r}, t_0)\rangle}{\langle I(\mathbf{r}, t_0)\rangle^2}. \tag{1.13}$$

The SIEGERT relation describes the second-order correlation by the first-order function [19]

$$g^{(2)}(\Delta r) = 1 + |g^{(1)}(\Delta r)|^2. \tag{1.14}$$

Hence, the second-order correlation function does not provide any further information than $g^{(1)}$ but is experimentally easier accessable. For $\Delta r = 0$ the correlation function gives a measure of the contrast [23]

$$C = |g^{(1)}(\Delta r = 0)|^2 = g^{(2)}(\Delta r = 0) - 1 = \frac{\langle I\, I\rangle}{\langle I\rangle^2} - 1. \tag{1.15}$$

The correlation function eqn. (1.13) is a good measure of the speckle size. The size of the speckle corresponds reciprocally to the beam width in the object plane [28, 29]. We put a movable pinhole of $2.5\mu m$ in diameter in front of a $CoPt$ (see § 2.5.1 and § B) multilayer sample that was sputtered on a transparent SiN membrane ($20.9\ \mu m \times 32.8\ \mu m$ in size) to allow transmission geometry. The distance between the pinhole and the sample is adjustable with a micrometer-range UHV manipulator. To first approximation the sample is illuminated only over the region of the central maximimum, called the AIRY disc, produced by the pinhole at the position of the sample (see § A). By varying the pinhole-sample distance, we are able to tune the speckle size. Fig. 1.16 shows the resulting speckle pattern for various distances of the pinhole to the sample, (a) 1.4 mm, (b) 8 mm and (c) 20 mm. The decreasing speckle size with increasing distance is obvious.

The corresponding spatial correlation plots are shown in Fig. 1.17. The correlation is done for a subset of the complete scattering pattern as indicated in Fig. 1.16(a) (white box). The widths of the correlation function match the appropriate speckle sizes. It is determined as the full width of the half-maximum from the cross-sections shown in Fig. 1.17. For a distance of 1.4 mm of the pinhole to the sample the average speckle size is about 760 μm in the observation plane. Increasing the pinhole-sample distance to 8 mm causes smaller speckle of 520 μm in size. If the pinhole is moved away from the sample up to 20 mm the speckle size reduces to 160 μm.

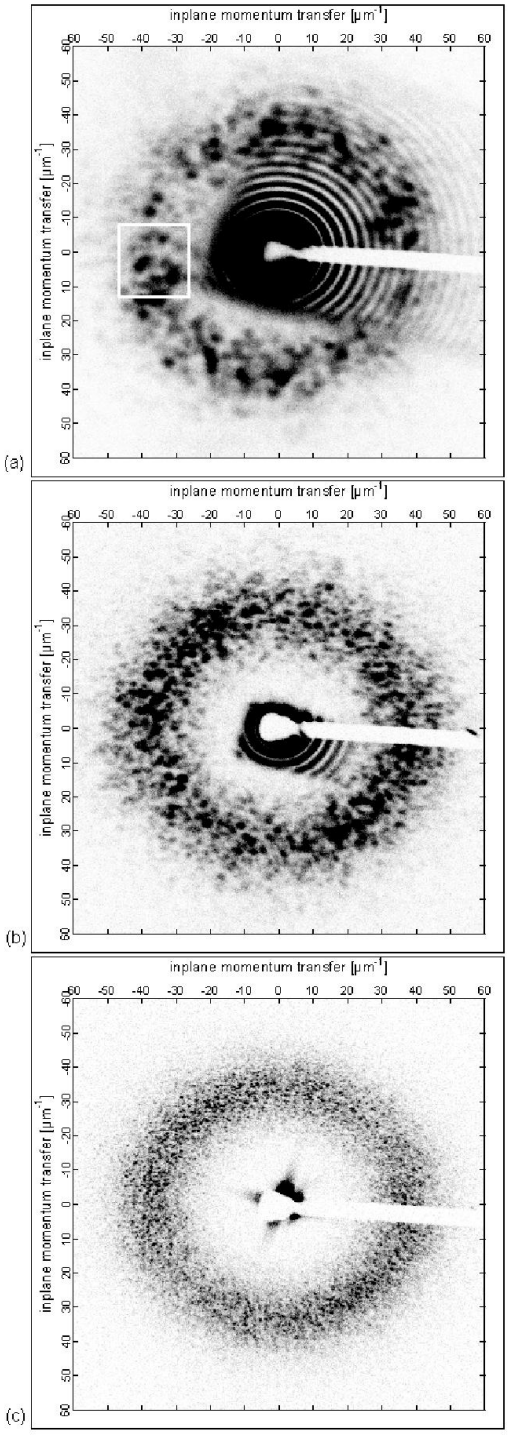

Figure 1.16: *Two-dimensional scattering images of the CoPt ferromagnetic domains obtained for a distance between the collimating pinhole and the sample of (a)* 1.4 *mm, (b)* 8 *mm and (c)* 20 *mm. In (a) and (b) the facet of the membrane on which the CoPt film is sputtered is clearly visible. For large distances the diffraction rings of the pinhole are screened by the facet. From the right side a beamblock is applied to avoid detector saturation in the specular peak.*

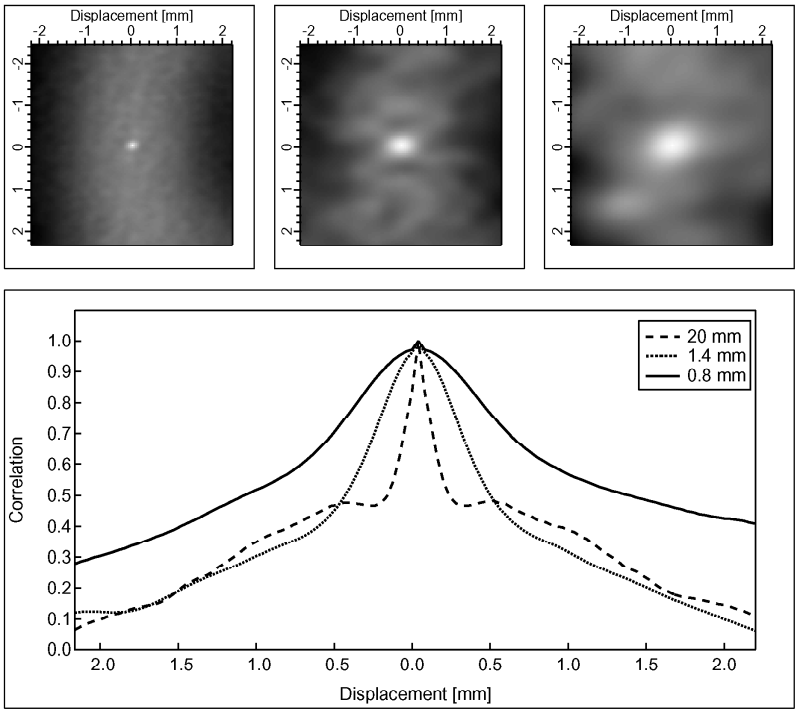

Figure 1.17: *Upper row of images: Correlation maps for a pinhole-to-sample distance of* 1.4 *mm,* 8 *mm and* 20 *mm (left to right). The graph below shows the horizontal cross-section through the maps for distances of* 1.4 *mm (solid line),* 8 *mm (dotted line) and* 20 *mm (dashed line). The Speckle size is determined as the full width at half-maximum. The displacement* Δr *is given in mm.*

Chapter 2

Resonant Coherent Scattering from Magnetic Materials

In this chapter we the various influences on the scattering process of soft X-rays from magnetic materials is investigated. The resonant cross-section for X-rays is considered, namely its dependence on polarization and energy. After the theoretical introduction the experimental results and their discussion are presented. The comprehension of these dependencies is important to analyze the magnetic scattering with respect to image reconstruction and dynamic experiments.

Soft x-rays generated at synchrotron facilities can be tuned to excitation energies of atomic core electrons and consequently allow for element specific investigations. Furthermore, the polarization of soft x-ray photons is selectable and can be used for polarization dependent or spin-selective electron excitation. This work is focussed on the investigation of scattering from *magnetic* structures. The theory of absorption and scattering from magnetic moments is elaborated since several years [1, 2, 4, 30] and many pioneering experiments have established important techniques for (magnetic) material science (*e.g.* [5, 31]). The atomic scattering processes are described by the *resonant magnetic scattering amplitude* that consideres energy and polarization dependence [4]. The first three sections of this chapter describe the basics of the resonant scattering amplitude and its corresponding dependencies. Typically, extreme ultraviolet (EUV) and soft x-ray (SXR) radiation ranges from 50 nm to 0.5 nm wavelength [18] and consequently allows for core electron excitation but cannot be used for probing of atomic distances like *e.g.* conventional Bragg or crystal lattice diffraction of hard x-rays. Hence, it is important to distinguish the atomic scattering amplitude that describes the scattering process from the small angle scattering (SAS) that is caused by comparably macroscopic magnetic domain structures. The small angle scattering is subject of section § 2.4.

2.1 The *atomic* resonant magnetic scattering factor

As all experiments were performed at resonances of the element carrying the magnetic moment, only the so called *resonant magnetic-resonant charge* scattering is considered. Of course, non-resonant charge and non-resonant magnetic scattering exists. Lovesey [10] introduces the different kinds of charge and magnetic scattering in his book in a very comprehensive form. Non-resonant magnetic scattering induces 90° phase shifts into the scattered wave whereas non-resonant charge scattering does not. Consequently, the scattering from both merely superimpose and due to the 10^6 times stronger charge signal [10] the magnetic scattering is nearly negligible. The magnetic signal can only be recovered if the scattering from both charge and magnetic moments is separated in reciprocal space and the magnetic scattering exceeds the noise background.

Rather than superposition of the charge and magnetic scattering interference of both allows to increase the "magnetic" contribution [10]. From eqn. (D.18) it is found that the interference contributes linear

in magnetic moments $\hat{\mathbf{M}}_n$ to the cross-section. Hence, the magnetic scattering is increased by a factor of 10^3 [10]. Charge-magnetic interference can be induced in different ways: 1) the charge and magnetic scattering occurs at different lattice sites of an non-centro-symmetric crystal [10]. 2) Circular polarized light is used which is a composition of two linear polarized orthogonal waves with 90° retardation of one wave. And 3), interference is induced at a resonance of one of the atomic elements which is not neccessarly the magnetic one [10].

In the first case the scattering phases depend the lattice site distribution of the charge and magnetic moments, hence, aloowing for the correct phase shift between charge and magnetic scattering. This is possible for *e.g. anti*ferromagnetic crystals [10]. In the second case, using circular polarized light is helpful because there are always contributions from both charge and magnetic scattering that can interfere. In this thesis the third case, resonant scattering, is considered. Resonances induce anomalous scattering, described by complex refractive indices that permits the charge scattering to interfere with the magnetic scattering. With scattering at a corresponding magnetic resonance-energy interference is also allowed for linearly polarized light assuming the right experimental geometry.

The X-ray scattering process is strongly related to X-ray absorption and the dispersive properties of matter. The energy regime of Soft-X-rays allows both non-resonant and resonant scattering due to excitation of core-electrons. As a consequence, high cross-sections of absorption and anomalous dispersion become important. The scattering amplitude f for magnetic scattering is in general the sum of non-resonant and resonant terms [4]:

$$f_n \approx f^0_{nonres} + f^{magn}_{nonres} + f' + if''. \tag{2.1}$$

The measurable scattering signal is then obtained by summing over all lattice sites $\mathbf{r}_n$ with a phase factor containing the momentum transfer $\mathbf{Q} = \hat{\mathbf{q}}' - \hat{\mathbf{q}}$, where $\hat{\mathbf{q}}$ and $\hat{\mathbf{q}}'$ are the wavevectors of the incident and scattered light, respectively:

$$I \propto \left| \sum_n e^{i\mathbf{Q}\mathbf{r}_n} f_n \right|^2 . \tag{2.2}$$

The scattering factor f is a complex number, in general. The dispersive and absorption contributions are covered by f' and f'', respectively. They are relevant for resonant charge and magnetic scattering as we will see below.

Let us consider strong resonance effects as they occur at a $Co\ L_3$ edge, for example. Thus, the scattering amplitude f_n is dominated by its resonant terms. For simplicity, we just consider dipole transitions [4, 10]:

$$f^{res}_n(\hat{\mathbf{q}}, \hat{\mathbf{q}}'; \hat{\mathbf{e}}, \hat{\mathbf{e}}') = (\hat{\mathbf{e}}' \cdot \hat{\mathbf{e}}) F^{(0)}_n - i(\hat{\mathbf{e}}' \times \hat{\mathbf{e}}) \cdot \hat{\mathbf{m}}_n F^{(1)}_n + (\hat{\mathbf{e}}' \cdot \hat{\mathbf{m}}_n)(\hat{\mathbf{e}} \cdot \hat{\mathbf{m}}_n) F^{(2)}_n. \tag{2.3}$$

Here, $\hat{\mathbf{e}}$ and $\hat{\mathbf{e}}'$ are the unit vectors of the **E**-field for the incident and the scattered light, respectively, also describing the direction of polarization. It is common to establish both vectors in components parallel and perpendicular to the scattering plane (Fig. 2.1). Hence, light with an elliptical component is described as a composition of two orthogonal linear waves. $\hat{\mathbf{m}}_n = (m_1, m_2, m_3)$ is the unit vector in direction of the magnetization at the atomic site $\mathbf{r}_n$. The complex resonance strengths F_n include all electronic properties of the material, e.g. the atomic excitation and decay processes. They have a resonant denominator and are energy dependent [4, 10]. The first term in eqn. (2.3) describes the resonant scattering from the charge distribution and is independent of the magnetic moment. The second term reveals a linear dependency of the magnetic moment and gives rise to X-ray Magnetic Circular Dichroism (XMCD). The third term is quadratic in $\hat{\mathbf{m}}_n$ and therefore it is not sensitive to the direction of the magnetic moment. It becomes important in probing *anti*ferromagnetic materials with linear polarized light (X-ray Magnetic Linear Dichroism, XMLD).

After the atomic scattering amplitude is introduced some special cases are considered concerning polarization dependence of the scattering cross-section and its charge-magnetic interference term. Of course, charge-magnetic interference cannot occur on an atomic level for wavelengths of soft x-rays

because the wavelengths are too large to fulfill the conditions for lattice scattering. Nevertheless, the atomic scattering amplitude is helpful to understand the interaction of the small angle scattering from the magnetic domains with the diffraction of a pinhole that is applied to achieve the coherent beam conditions (see experimental setup in § 1.1.1). Charge scattering is usually neglected. But the polarization dependence of the diffraction from the pinhole is basically the same as for the charge term, $(\hat{\mathbf{e}}' \cdot \hat{\mathbf{e}})$, *i.e.* concerning the polarization effects the pinhole diffraction can be considered the same way as the charge scattering.

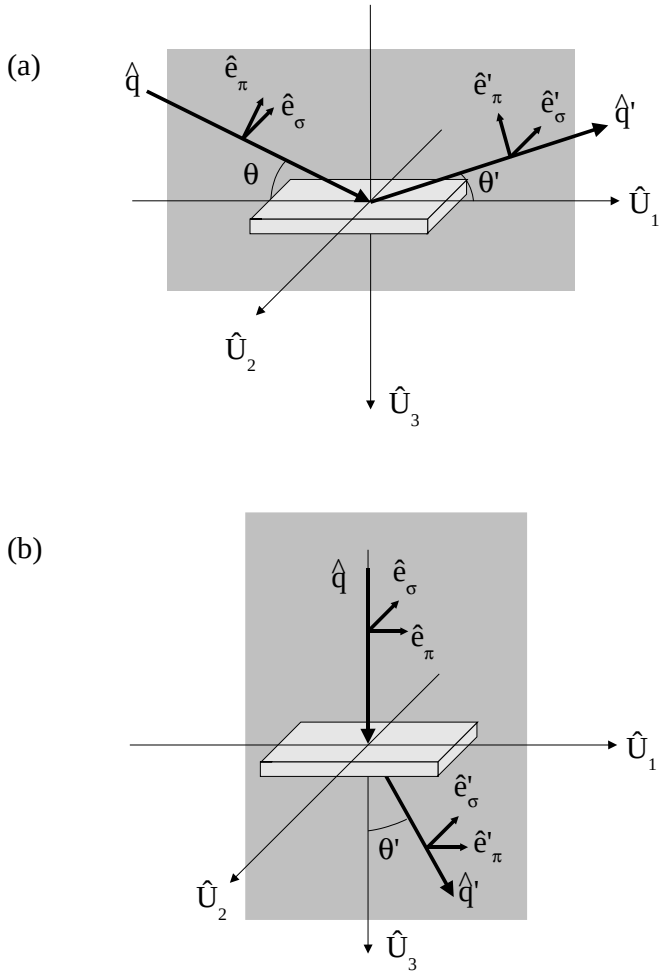

Figure 2.1: *Scattering geometry: (a) reflection and (b) transmission. In reflection the incident wavevector* $\mathbf{q}$ *encloses an angle* θ *with the sample surface and the scattered wavevector* $\mathbf{q}'$ *takes an angle* θ'*. For transmission geometry the incident angle is* $90°$ *and the scattering angle is measured with respect to the surface normal by convention.*

2.2 Polarization and magneto-optical effects

The dipole scattering amplitude f_n^{res} describes all atomic processes including magneto-optical effects and resonant enhancements. The vector-depending terms $(\hat{\mathbf{e}}' \cdot \hat{\mathbf{e}})$, $(\hat{\mathbf{e}}' \times \hat{\mathbf{e}}) \cdot \hat{\mathbf{m}}_n$ and $(\hat{\mathbf{e}}' \cdot \hat{\mathbf{m}}_n)(\hat{\mathbf{e}} \cdot \hat{\mathbf{m}}_n)$ of eqn. (2.3) select the possible contribution of each term to the scattering process for a given polarization

of the light before and after the scattering process. Modern synchrotron insertion devices allow the control of polarization of X-rays. This permits to investigate easily the effect of polarization on the scattering process. This chapter focusses mainly on the "XMCD"-term of the scattering amplitude. For further details about a complete consideration of the "circular" and "linear" term see *e.g.* [4, 10, 32].

The XMCD effect is based on the different probabilities of excitation for right- and left-circular polarized light and the spin-selective final density of states. This is taken into account by complex helicity-dependent resonance strengths F_n [4]. Let us write F^1_{+1} for a helicity parallel and F^1_{-1} for a helicity antiparallel to the net magnetization in the sample. Then the resonant scattering factor can be written as [4, 10, 32]:

$$f_n^{res} = \frac{3}{4q}(\hat{\mathbf{e}}' \cdot \hat{\mathbf{e}})[F^1_{+1} + F^1_{-1}] - i\frac{3}{4q}(\hat{\mathbf{e}}' \times \hat{\mathbf{e}}) \cdot \hat{\mathbf{m}}_n[F^1_{+1} - F^1_{-1}]. \tag{2.4}$$

with $q = \frac{2\pi}{\lambda}$ and omitting the linear dichroism term,

$$f_{lin} = -\frac{3}{4q}(\hat{\mathbf{e}}' \cdot \hat{\mathbf{m}}_n)(\hat{\mathbf{e}} \cdot \hat{\mathbf{m}}_n)[2F^1_0 - F^1_{+1} - F^1_{-1}]. \tag{2.5}$$

The bilinear form of eqn. (2.4) may be expressed in matrix form $\left\langle \tilde{\mathbf{M}} \right\rangle$ with a basis of linear polarization states perpendicular $\hat{\mathbf{e}}_\sigma$ and parallel $\hat{\mathbf{e}}_\pi$ to the scattering plane as DE BERGEVIN and BRUNEL proposed it [2, 33]. Then we obtain:

$$\begin{aligned} f_n^{res} \quad = \quad & \frac{3}{4q}\left\langle \begin{pmatrix} 1 & 0 \\ 0 & \hat{\mathbf{q}} \cdot \hat{\mathbf{q}}' \end{pmatrix} \right\rangle [F^1_{+1} + F^1_{-1}] \\ & -i\frac{3}{4q}\left\langle \begin{pmatrix} 0 & \hat{\mathbf{q}} \\ -\hat{\mathbf{q}}' & \hat{\mathbf{q}}' \times \hat{\mathbf{q}} \end{pmatrix} \right\rangle \cdot \hat{\mathbf{m}}_n[F^1_{+1} - F^1_{-1}]. \end{aligned} \tag{2.6}$$

Details of the matrix formalism to describe the polarization states are described in Appendix D.3. Now, we have a complete description of the scattering amplitude dependence on the incoming and scattered wavevectors, $\hat{\mathbf{q}}'$ and $\hat{\mathbf{q}}'$, the quantization direction of magnetic moments $\hat{\mathbf{m}}$, and finally the state of polarization $\hat{\mathbf{e}}_\sigma$ and $\hat{\mathbf{e}}_\pi$.

2.2.1 Linear polarization

With expression (2.6) we can easily discuss the charge scattering and the magnetic scattering under consideration of the polarization. The matrix form (eqn. (D.11)) allows to select the contribution of every term assuming known polarization of the incident and scattered radiation and the direction of the magnetization (cp. § D.3). For simplicity let us consider only the forward scattering (or near specular scattering) with change of polarization allowed, *i.e.* $\hat{\mathbf{q}} = \hat{\mathbf{q}}'$ (this has to be distinguished from the situation discussed in § 2.3.1 where elastic forward scattering with no change in state of polarization is considered, *i.e.* $\hat{\mathbf{q}} = \hat{\mathbf{q}}'$ and $\hat{\mathbf{e}} = \hat{\mathbf{e}}'$).

The state of linear polarization is defined always with respect to the scattering plane using the following standard notation: σ represents linear polarized light with the **E**-field vector perpendicular to the scattering plane and π light is polarized parallel to that plane. The scattering plane itself is spanned by the incoming **q**-vector and the outgoing vector $\mathbf{q}'$. The resonant charge scattering term does not change the state of polarization, *i.e.* only $\sigma \to \sigma'$ and $\pi \to \pi'$ scattering occurs which is expressed in the diagonal form of the charge term matrix. In contrast, the magnetic term can change the polarization. Some special cases are considered next:

σ-light, any geometry - For magnetic scattering of linear polarized light $\sigma \to \sigma'$ is forbidden whereas every other scattering channel is enabled. Hence, with σ light no interference of the charge

and magnetic term is allowed because the charge scattered wave is perpendicular polarized to the magnetically scattered wave. The suppression of interference of orthogonal states is obvious:

$$I \propto |f^{res}|^2 = |f_c + f_m|^2 ,$$

with f_c and f_m for charge and magnetic amplitude, respectively. Assuming in-phase relation of both amplitudes we get [10],

$$I \propto f_c^2 + f_m^2 + 2 f_c f_m .$$

The interference term $2 f_c f_m$ vanishes for orthogonal **E**-fields.

π-light, reflection geometry - Incident π radiation supports the charge-magnetic interference because both terms contribute to the scattering amplitude with emitted π' light. These polarization dependencies can be exploited to obtain information about the magnetization direction in magnetic materials, as *e.g.* shown in [13]. The $(\pi \rightarrow \pi')$-channel is valuable for interference scattering while the angle of incidence θ is smaller than 90° (reflection geometry, cp. Fig.2.1(a)) and there are in-plane magnetic moments[1], *i.e.* $\hat{\mathbf{m}}_n = m_1 \hat{\mathbf{U}}_1 + m_2 \hat{\mathbf{U}}_2$.

π-light, transmission geometry - For transmission geometry (cp. Fig. 2.1(b)) and pure out-of-plane magnetization the former result is not longer valid. The $(\pi \rightarrow \pi')$-element of the magnetic term in eqn. (2.6) is zero then, hence, the interference term of eqn. (D.18) vanishes.

Forward scattering - The forward scattering causes the polarization plane of incident π or σ light to be rotated upon interaction with out-of-plane magnetic moments. Furthermore, the light gets an elliptical component. This well known magneto-optical FARADAY-effect can be calculated using eqn. (D.9) and (D.18). As introduced in Appendix D.1 it is convenient to describe the state of polarization in terms of STOKES parameters $P_i, i = 1, 2, 3$. For σ or π light the polarization vector is $\mathbf{P} = (0, 0, +1)$ or $\mathbf{P} = (0, 0, -1)$, respectively[2]. The resulting scattering cross-section is obtained with eqn. (D.18),

$$\frac{d\sigma}{d\Omega} \propto |\rho(\mathbf{Q})|^2 \left[F^1_{+1} + F^1_{-1}\right]^2 + 4\pi^2 M(\mathbf{Q})^2 \left[F^1_{+1} - F^1_{-1}\right]^2 ,$$

where $\rho(\mathbf{Q})$ is the structure factor of the charge density and $M(\mathbf{Q})$ is the magnetic structure factor. Only the pure charge and magnetic terms remain and no charge-magnetic interference is observable. The polarization state of the scattered light can be calculated using eqn. (D.9),

$$\begin{aligned}
P'_1 &= \frac{4\pi M(\mathbf{Q})\rho(\mathbf{Q}) \left[\Re\left\{F^{(1)}\right\}\Im\left\{F^{(0)}\right\} - \Re\left\{F^{(0)}\right\}\Im\left\{F^{(1)}\right\}\right]}{\rho^2(\mathbf{Q})\left|F^{(0)}\right|^2 + 4\pi M(\mathbf{Q})^2\left|F^{(1)}\right|^2} \\
P'_2 &= \frac{4\pi M(\mathbf{Q})\rho(\mathbf{Q}) \left[\Re\left\{F^{(0)}\right\}\Re\left\{F^{(1)}\right\} + \Im\left\{F^{(0)}\right\}\Im\left\{F^{(1)}\right\}\right]}{\rho^2(\mathbf{Q})\left|F^{(0)}\right|^2 + 4\pi M(\mathbf{Q})^2\left|F^{(1)}\right|^2} \\
P'_3 &= \frac{|\rho(\mathbf{Q})|^2\left|F^{(0)}\right|^2 - 4\pi M(\mathbf{Q})^2\left|F^{(1)}\right|^2}{|\rho(\mathrm{b}fQ)|^2\left|F^{(0)}\right|^2 + 4\pi M(\mathbf{Q})^2\left|F^{(1)}\right|^2}.
\end{aligned}$$

The resonance strengths are $F^{(0)} = \left[F^1_{+1} + F^1_{-1}\right]$ and $F^{(1)} = \left[F^1_{+1} - F^1_{-1}\right]$. The resulting vector of polarization $\mathbf{P}'$ has non-zero components P'_1 and P'_2. The first parameter describes the degree of linear polarization of 45° with respect to the scattering plane and indicates that the plane of polarization has been rotated (FARADAY-rotation). A non-zero second parameter P'_2 indicates that a circular component of the polarization appeared after the scattering which is consistent with ellipticity measurements upon FARADAY effect [34–36].

[1] Concerning magnetic moments the expressions "in-plane" and "out-of-plane" are meant with respect to the sample surface.

[2] The vector **P** is unity for completely polarized light and zero for complete *un*polarized light

2.2.2 Circular polarization

Circular polarized light is composed by two orthogonal and phase-shifted waves of linear polarization and represented by the second STOKES parameter P_2 of the polarization vector. As for linear polarization some special cases are considered.

Specular scattering, out-of-plane magnetization - For specular scattering ($\theta = \theta'$) of circular polarized photons from magnetic domains of any direction of magnetization the polarization is not changed,

$$P = (0, \pm 1, 0) \rightarrow P' = (0, \pm 1, 0),$$

which is a result of eqn. (D.9) and (D.18). The interaction of circular polarized photons with magnetic moments affects only the phase velocity inside the material which is different parallel or antiparallel orientation of the magnetization to the helicity [37]. The interference term is non-zero for specular scattering in transmission and reflection geometry if the magnetization is parallel to $\hat{\mathbf{U}}_3$ as defined in Fig. 2.1, *e.g.* as in a thin film with perpendicular anisotropy.

Forward scattering in transmission, in-plane magnetization - In transmission experiments the interference term vanishes for in-plane magnetization ($\hat{\mathbf{m}} = m_1\hat{\mathbf{U}}_1 + m_1\hat{\mathbf{U}}_2$), even no magnetic scattering is observed and the cross-section reduces to pure charge scattering:

$$\frac{d\sigma}{d\Omega} \propto |\rho(\mathbf{Q})|^2$$

, what is consistent with angle dependent XMCD measurements [9, 38].

Small angle scattering, out-of-plane magnetization - Of course, forward scattering is just a very special case. Considering a diffuse scattering angle $\theta' \neq \theta$ changes the process immensely. For perpendicular (out-of-plane) magnetization ($m(\mathbf{Q}) \propto \hat{\mathbf{U}}_3$) and transmission geometry the final polarization becomes with $P = (0, 1, 0)$ (initial right circular polarization),

$$P' = \left(0, \frac{2\cos(\theta')}{1+\cos^2(\theta')}, \frac{1-\cos^2(\theta')}{1+\cos^2(\theta')}\right)$$

setting eqn. (D.18) into eqn. (D.9). The scattered waves are elliptically polarized with a linear fraction P_3' that increases with increasing scattering angle θ' (cp. Fig. 2.2).

The final polarization would be completly linear polarized for a scattering angle of $\theta' = 90°$. Of special interest is the small angle scattering cross-section,

$$\begin{aligned}\frac{d\sigma}{d\Omega} \quad \propto \quad & \frac{1}{2}\left(1+\cos^2(\theta')\right)\Big[|\rho(\mathbf{Q})|^2\left|F^{(0)}\right|^2 + 4\pi^2 M^2(\mathbf{Q})\left|F^{(1)}\right|^2 \\ & - 4\pi\rho(\mathbf{Q})M(\mathbf{Q})\left(\Re\left\{F^{(0)}\right\}\Re\left\{F^{(1)}\right\} + \Im\left\{F^{(0)}\right\}\Im\left\{F^{(1)}\right\}\right)\Big],\end{aligned}$$

with $\rho(\mathbf{Q})$ and $M(\mathbf{Q})$ being the structur factors of charge density and magnetic moments, respectively. Again, pure charge and magnetic scattering are observable and additionally an interference term proportional to the product $\rho(\mathbf{Q})M(\mathbf{Q})$ contributes to the intensity. An interesting case is present if the charge term depends only on the real part of the resonance strength $F^{(0)}$ as is true for a real-valued object like an aperture. Then the interference term is only proportional to the real part $\Re\left\{F^{(1)}\right\}$ of the magnetic resonance strength $F^{(1)} = F^1_{+1} - F^1_{-1}$ which itself is proportional to the dispersion (real part) of the magneto-optical constant [10, 34].

2.3 Energy dependence of resonant magnetic scattering

The energy dependence of the resonant magnetic scattering amplitude is represented in the energy dependence of the resonance strengths $F^{(0,1)}$. In this section it is shown how the complex atomic

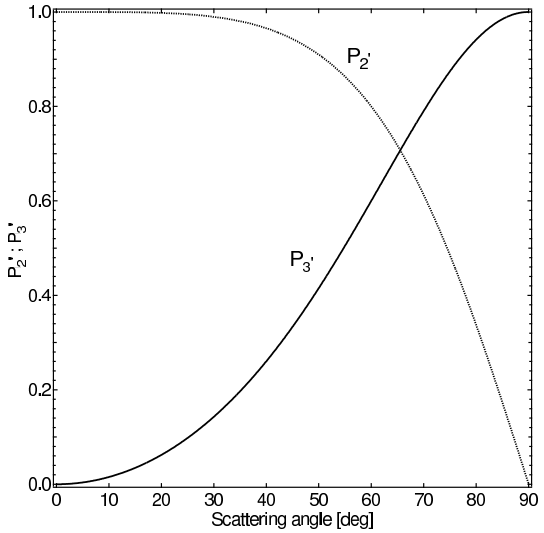

Figure 2.2: *Final polarization parameters P_2' (dotted line) and P_3' (solid line) as function of the scattering angle θ' for perpendicular magnetic anisotropy and transmission geometry.*

resonance strengths are related to the optical constants that are experimentally accessable [34, 35] and reveal the energy dependence of the scattering amplitude. As linear polarized light may be considered as an interference of two circular polarized waves with opposite helicity the following calculations are done assuming circular polarized waves as a basis. The content follows the presentation in LOVESEY: *X-Ray Scattering and Absorption by Magnetic Materials* [10]).

2.3.1 Optical constants, forward scattering and dichroism

On one hand, the interaction of electromagnetic waves and matter is described macroscopically by the dielectric function with a complex index of refraction n,

$$n = 1 - \delta + i\beta, \tag{2.7}$$

where δ is the dispersive index and β represents the absorption index. A magnetic material has different refractive indices for left $(-)$ and right $(+)$ circular polarized light,

$$n_{\pm} = n \pm \Delta n, \tag{2.8}$$

where $\Delta n = -\Delta\delta + i\Delta\beta$. On the other hand, an atomic description of the dispersive and absorptive processes is given by the forward scattering amplitude of circular polarized waves $f_{(0)}\left(\hat{\mathbf{q}} = \hat{\mathbf{q}}'; \hat{\mathbf{e}}_\nu = \hat{\mathbf{e}}'_\nu\right)$, where ν is the relative orientation of the photons helicity and the magnetic axis[3]. Forward scattering is characterized by maintaining the direction of the wavevector $(\hat{\mathbf{q}} = \hat{\mathbf{q}}')$ and the state of the polarization $(\hat{\mathbf{e}}_\nu = \hat{\mathbf{e}}'_\nu)$. The resonant forward scattering amplitude is given by [10],

$$f_{(0)}\left(\hat{\mathbf{q}} = \hat{\mathbf{q}}'; \hat{\mathbf{e}}_\nu = \hat{\mathbf{e}}'_\nu\right) = -\left[r_e Z + \left(\frac{3}{4q}\right)\left\{[F^1_{-1} + F^1_{+1}] - \nu\cos\phi[F^1_{-1} - F^1_{+1}]\right\}\right], \tag{2.9}$$

where r_e is the classical electron radius, Z the atomic number and ϕ the angle between the initial wavevector $\hat{\mathbf{q}}$ and the magnetic axis of the sample. The real and imaginary parts of the refractive index n are related to the real and imaginary parts of the resonant forward scattering amplitude by [10],

$$\Re\{n\} \quad = \quad 1 + \left(\frac{2\pi n_0}{q^2}\right)\Re\left\{f_{(0)}\left(\hat{\mathbf{q}} = \hat{\mathbf{q}}'; \hat{\mathbf{e}} = \hat{\mathbf{e}}'\right)\right\} \tag{2.10}$$

and

[3] $\nu = +/-1$ for *parallel* or *antiparallel* orientation.

$$\Im\{n\} \quad = \quad \left(\frac{2\pi n_0}{q^2}\right) \Im\left\{f_{(0)}\left(\hat{\mathbf{q}} = \hat{\mathbf{q}}'; \hat{\mathbf{e}} = \hat{\mathbf{e}}'\right)\right\}. \tag{2.11}$$

These relations link the *macroscopic* refractive indices and the *atomic* scattering amplitude[4]. Exploiting magneto-optical effects like FARADAY rotation of linear polarized light and measurements of the ellipticity allows for calculating the atomic scattering factors due to the eqn. (2.11) and eqn. (2.11). The rotation and the ellipticity of initially linear polarized light interacting with magnetic material are caused by a difference in absorption and phase velocity for left- and right-circular polarized photons (the two partial waves of linear photons). Therefore, the difference in refractive indices are calculated next. For $n_+ - n_- \propto \Delta n = -\Delta\delta + i\Delta\beta$ one gets [10],

$$\Delta\delta \propto \cos\phi\ \Re\left[F^1_{-1} - F^1_{+1}\right] \quad and \quad \Delta\beta \propto -\cos\phi\ \Im\left[F^1_{-1} - F^1_{+1}\right]. \tag{2.12}$$

$\Delta\delta$ can be measured by polarization analysis experiments because it is proportional to the FARADAY rotation angle. $\Delta\beta$ can be obtained, *e.g.* in the soft x-rays regime, by XMCD measurements [10,34,35]. The atomic scattering amplitude can be expressed in charge and magnetic terms each complex-valued,

$$f = (f'_c + if''_c) \pm (f'_m + if''_m). \tag{2.13}$$

Hence, from the measurements of the FARADAY rotation and/or XMCD signal the scattering factors can be calculated using above relations (eqn. (2.12)) [34,35]. For the $Co\ L_3$ absorption edge the factors are plotted in Fig. 2.3 from results in Ref. [14].

In the experiments presented here the scattering intensity can be measured as function of energy. No polarization analysis is done and XMCD signals cannot be measured because the dichroism signal is cancelled out by oppositely magnetized domains. XMCD could be measured by saturating the magnetic domains and reversing the helicity, but saturation destroys the initial domain arrangement. Consequently, only the small angle scattering (SAS) signal and the transmission intensity are recorded (see § 2.5.2.1). The scattering spectrum can by modulated by knowing the atomic scattering factors (Fig. 2.3) and using the following relation for the scattering cross-section σ_s [39],

$$\sigma_s \propto (f')^2 + (f'')^2. \tag{2.14}$$

The discussion of the energy dependence is important concerning the strong variation of the optical indices and, consequently, the atomic scattering amplitude, by only small variation of the energy in proximity of an absorption edge. The question arises whether the coherent scattering pattern is affected by a small energy variation and if so, how can this be understood. This question is subject to section § 2.5.2.

2.4 Small Angle X-ray Scattering (SAXS)

So far the scattering process was discussed on an atomic level. The experiments performed and presented in this work were done with soft X-rays of 1.6 *nm* to 3.1 *nm* wavelength. Atomic distances or electron densities of Å-range cannot be probed with these wavelengths. Nevertheless, the atomic processes are the same so that the atomic scattering amplitude is valid to describe the scattering process but it is no longer applicable to describe scattering from crystal lattice or charge densities.

Magnetic length scales range from interatomic lengths to domain sizes of many microns. The *nm*-scale of soft X-rays is advantageous to probe magnetic *nm*-domain periods. The scattering occurs from the lateral variation of the direction of the magnetization $\mathbf{m}$. Scattering maxima are obtained for angles where the momentum transfer $\mathbf{Q} = \mathbf{q}' - \mathbf{q}$ fits to a distance of two differently magnetized domains or their walls [13,14,40,41].

[4]The absorptive (imaginary) part of the refractive index is related to the imaginary forward scattering by the *optical theorem* [10].

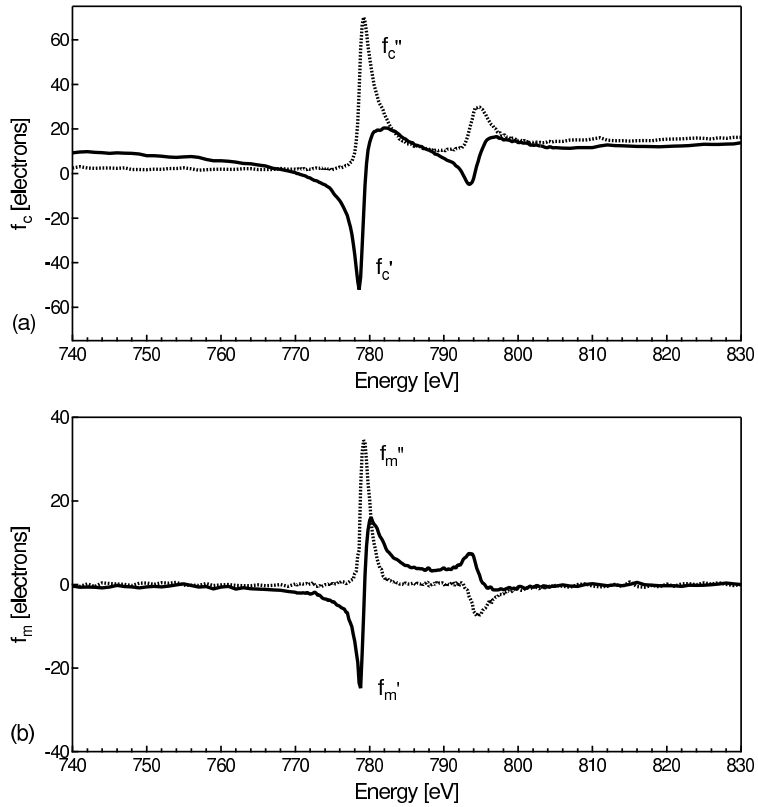

Figure 2.3: *(a) The real (solid line) and imaginary (dotted line) term of the charge scattering factors of Co at the L_3 and L_2 absorption edge. (b) The real (solid line) and imaginary (dotted line) part of the magnetic term of Co measured by [14]. The imaginary magnetic factor corresponds exactly to the difference spectrum of a saturated magnetic sample measured with right and left circular polarized radiation.*

For the *nm*-scale of magnetic domains the magnetic structure factor $\mathbf{M}(\mathbf{q})$ does not describe the lattice site of the magnetic moments but the spatial distribution of the magnetic domains, *i.e.* many atomic moments of the same average direction of magnetic anisotropy. Hence, the small angle scattering shown here has its origin in the lateral distribution of the magnetic domains.

2.5 Results - Polarization and Energy Dependence in coherent magnetic scattering

The theoretical considerations of the former section are next investigated experimentally. First, the dependence of the coherent magnetic scattering on the state of polarization is presented followed by a discussion of the energy dependence of the scattering pattern across the $Co\ L_3$ edge.

2.5.1 Variation of Polarization

As the electron density distribution can not be probed on a crystal lattice scale by soft x-rays the charge scattering discussed in former sections is usually not involved in the scattering experiments presented that are mainly performed in transmission geometry. Nevertheless, the discussion of charge-magnetic interference scattering is still valuable. The diffraction from apertures mostly used to collimate the illumination of the sample to an area that allows for coherent illumination can be described by the same polarization dependence as pure charge scattering: $(\hat{\mathbf{e}}' \cdot \hat{\mathbf{e}})$. Hence, in this section the interference of diffracting objects and magnetic small angle scattering is investigated.

Coherent resonant magnetic scattering from $CoPt$ multilayers (cp. § B) was measured in transmission geometry using soft X-rays of linear and circular polarization (see also [42]). Ferromagnetic $CoPt$ multilayers reveal an anisotropy which is perpendicular to the layers [14, 43]. We measured a multilayer sample in transmission geometry, *i.e.* the angle of incidence is $\theta = 90°$ and the magnetization vector $\hat{\mathbf{m}}$ of the sample is either parallel or *anti*parallel to the incident wavevector. The sample was sputtered on a SiN_x-membrane of 160 nm thickness to enable transmission. The 50 multilayers of 3 nm Co and 0.7 nm Pt were grown on a 20 nm Pt substrate and capped with 2 nm Pt [44]. A lateral domain structure develops in the multilayer with adjacent domains having opposite magnetization. Fig. 2.4(c) shows the worm-like domain structure. Dark and bright domains indicate the opposite direction of magnetization perpendicular to the multilayer film. The average in-plane correlation length of the domain structure is approximately 196 nm as measured by a maximum of the power spectral density[5] (PSD) at $q = 32\mu m^{-1}$ in Fig. 2.5. This domain structure gives rise to small angle x-ray scattering (SAXS) [14, 45].

$380\mu m$ in front of the $CoPt$-film a pinhole of a 2.5 μ-diameter (see Fig. 2.4(b) bottom) was mounted in order to illuminate the sample with a transversely coherent x-ray beam (cp. § 1). The transverse coherence area at the sample position is $\xi_v \approx 612\mu m \times \xi_h \approx 5.6\mu m$ for this setup, where ξ_v and ξ_h are the vertical and horizontal coherence lengths, respectively. The longitudinal coherence length is $\xi_l = 6.4\mu m$ assuring the capability of interference even for large scattering angles[6].

Fig. 2.6 shows the coherent small angle scattering patterns obtained for incident radiation of (a) linear polarization, (b) right circular polarization and (c) left circular polarization. The experiments were performed with a x-ray wavelength of 1.59 nm (778 eV), corresponding to resonant scattering at the CoL_3 edge (see also § 2.5.2). As seen in Fig. 2.6(a), the scattering pattern consists of a Fraunhofer pattern due to diffraction from the pinhole and a SAXS ring of intensity centered at $q = 0$. The radial distribution of the SAXS has its maximum at $q = 32\ \mu m^{-1}$ which corresponds well to the magnetic PSD in Fig. 2.5.

The coherent illumination of the $CoPt$ domains causes a speckle intensity structure which is characterized by destructive (low intensity) and constructive (high intensity) interference of the waves scattered

[5] The PSD is a common measure for the occurancy of a certain frequency in a signal pattern. It is obtained by calculating the square of the Fourier transform of the corresponding pattern (*e.g.* see [14])

[6] All values are calculated from beamline parameters using eqn. (1.1) and eqn. (1.4)

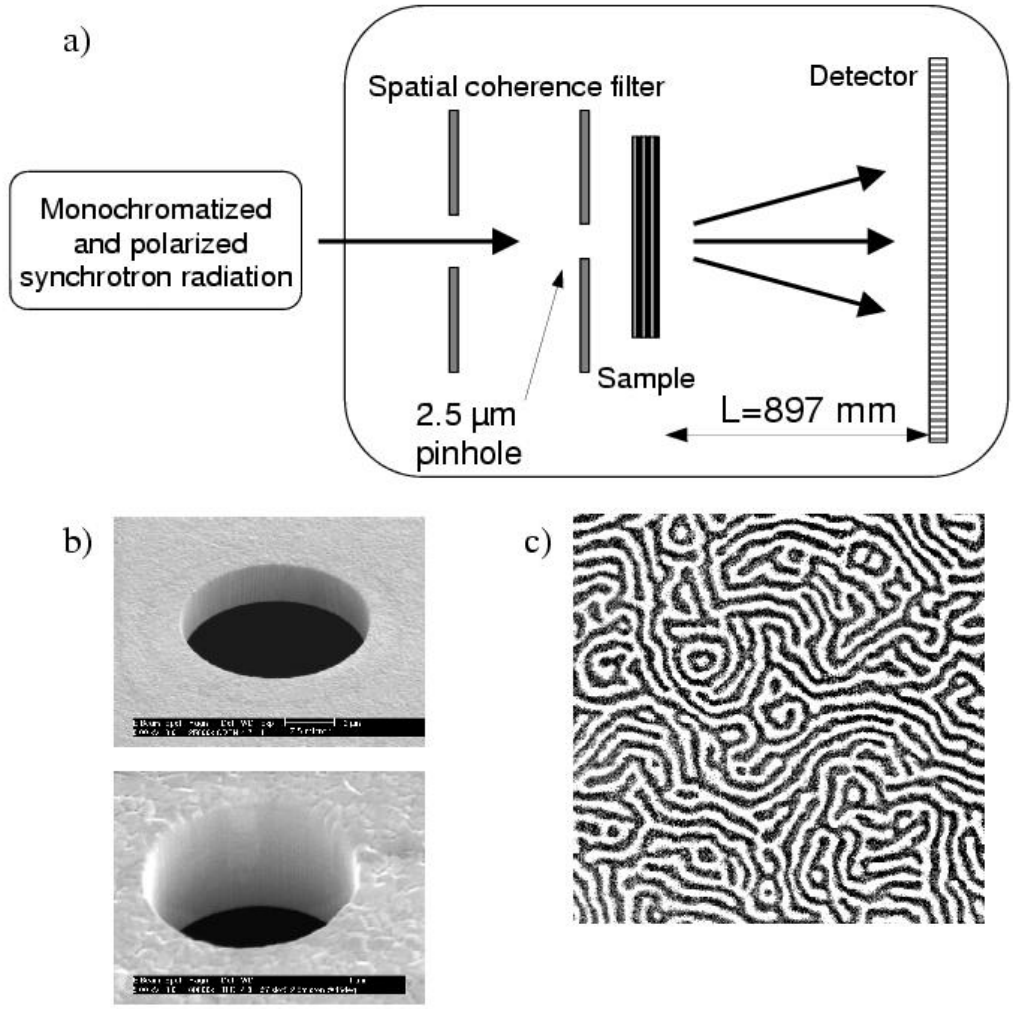

Figure 2.4: *(a) Scheme of the experimental setup for coherent resonant magnetic small angle scattering. The spatial coherence filter is a set of circular pinholes (cp. §1.1). The sample is measured in transmission geometry and the scattered radiation is detected by a two-dimensional position sensitive detector at* $L = 897$ *mm downstream of the object. (b) Electron Microscopy image of a* 7.5 μm *(top) and* 2.5 μm *(bottom) circular aperture. The holes were drilled into a free-standing Au-film of* 2 μm *thickness by focussed ion beam (FIB) of* 30 $keV Ga^+$ *ions [46]. (c) Soft X-ray transmission microscope (TXM) image of* $CoPt$ *multilayers taken at the ALS XM-1 microscope [21]. The image covers a* 5 $\mu m \times 5$ μm *region of the magnetic sample. The average period of two domains is about* 196 *nm causing a scattering intensity maximum at* $q = 32$ μm^{-1}.

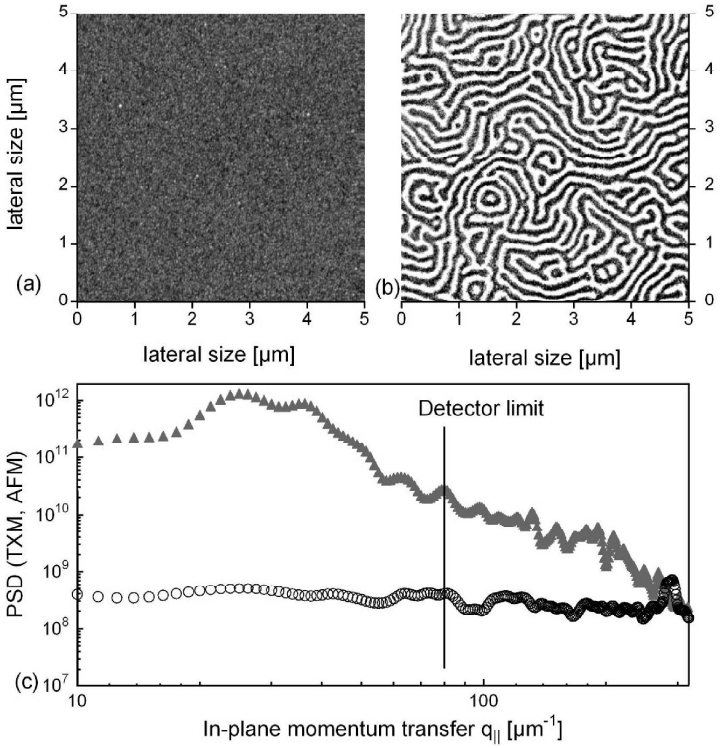

Figure 2.5: *(a) Atomic Force Microscope (AFM) image of the surface of the CoPt sample. The gray-scale range is from* 0 *nm to* 8.3 *nm (Courtesy of O. Hellwig). (b) Transmission X-ray microscope (TXM) of the CoPt multilayer (Courtesy of G. Denbeaux [21]). (c) Power spectral density (PSD) plots of the magnetic domains (gray triangles) obtained from TXM image and of the surface topography calculated from the AFM-image (black circles). The maximum of the PSD corresponds to the average period of the magnetic domain width. It is relatively broad ($q \approx 20\ \mu m^{-1}$ to $45\ \mu m^{-1}$) indicating that the periodicity is not sharp in one transverse direction (like it would be for stripe domains). At* 290 μm^{-1} *the PSD of the surface has a distinct peak corresponding to* 22 *nm correlation length of the granular surface.*

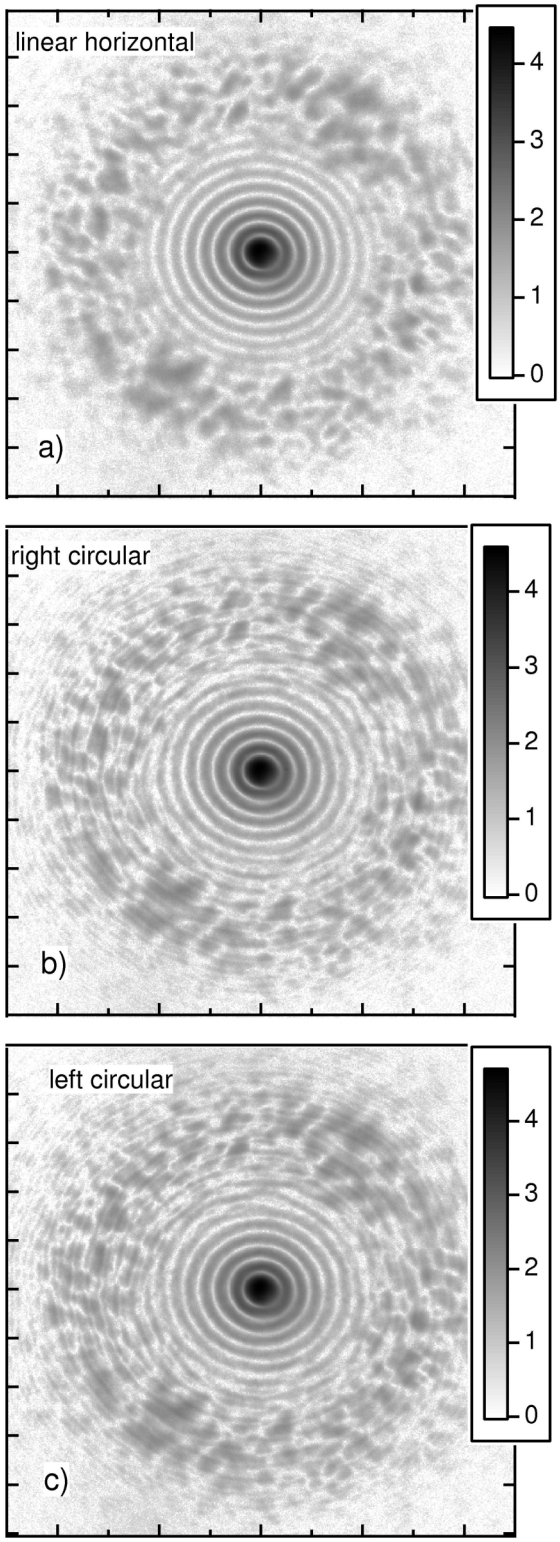

Figure 2.6: *Coherent small angle scattering patterns recorded with soft X-rays of* 1.59 *nm wavelength corresponding to the Co* L_3 *resonance. The intensity is plotted in logarithmic gray-scale. The Fraunhofer rings are caused by diffraction from the* 2.5μm *diameter pinhole. The coherent illumination of the CoPt domains cause the speckled intensity distribution. (a) shows the pattern for incident radiation of linear polarization. (b) and (c) demonstrate the influence of right and left circular polarized light on the scattering pattern, respectively.*

from the magnetic domain borders. The visibility of the speckle pattern is already determined in § 1.2.1 as an example and here just its value is reminded to be $V = 0.9$ indicating a high degree of coherence.

The domains contribute differently to the magnetic scattering amplitude f_m (second term of eqn. (2.6)) depending on their direction of the magnetization relative to the wavevectors $\mathbf{q}$ and $\mathbf{q}'$. This causes a different cross-section and hence a scattering contrast between the two types of domains. The scattering contrast is energy-dependent (see § 2.5.2). A contribution of the charge scattering f_c cannot be detected with the above setup as described above. The surface rms-roughness of the sample is less than 5 nm with a in-plane correlation lengths smaller than 22 nm as observed by atomic force microscopy (AFM), see Fig. 2.5(a). This typical surface structure size gives rise to a peak at 290 μm^{-1} and is beyond the angular detection capabilities of the setup. A frequency analysis (PSD) of the surface roughness obtained by atomic force microscopy (AFM, see Fig. 2.5(a)) is shown in Fig. 2.5(c) (black circles). This result corresponds well to the result presented in [14]. The PSD of the surface is calculated from the AFM data and does not show any distinct intensity peaks. Therefore, the surface scattering may be neglected in further consideration.

A clearly detectable contribution arises from the diffraction pattern of the collimating pinhole. The state of polarization is not changed upon diffraction from the aperture. In contrast, linearly polarized radiation is changed by magnetic scattering from $\sigma \rightarrow \pi'$ and $\pi \rightarrow \sigma'$. $(\pi \rightarrow \pi')$-scattering is forbidden for this geometry because of $\hat{\mathbf{q}}' \times \hat{\mathbf{q}} \perp \hat{\mathbf{m}}$. Consequently when linearly polarized radiation is incident on the pinhole and the sample, no interference between the pinhole diffraction and the magnetic scattering exists due to their orthogonal polarization states. The *superposition* (in contrast to *interference*) of the pinhole term and the magnetic term can be observed in Fig. 2.6(a).

The exact same sample region is also illuminated with coherent radiation of the same energy but with *circular* polarization ($P_2 = 0.85$ of the helical undulator UE56/1 at BESSY). Now the state of polarization remains the same upon diffraction from the pinhole as well as upon scattering from the magnetic domains (Spin-flip, *i.e.* left $\rightarrow$ right or vice versa, is forbidden). Both the diffracted and the magnetically scattered partial waves can interfere this time. Fig. 2.6(b) and (c) show the interference pattern for right circular and left circular polarization, respectively. The diffraction of the pinhole and the magnetic scattering both cover a broad q-space range around $q = 20\mu m$ where the interference becomes very well observable. In contrast to the "linear" case the Fraunhofer rings are disturbed. Furthermore, the magnetic speckle ring shows circular ripples caused by destructive and constructive interference.

For left and right circular radiation the detected intensity pattern is different. The difference is plotted in Fig. 2.7(b). The existance of a difference is not obvious at first glance when considering Babinet's theorem. Upon changing the helicity of the incident radiation the magnetic term of eqn. (2.6) flips its sign, *i.e.* the absorption cross-section of the magnetic domains causes the bright domains in Fig. 2.4(c) to become dark and vice versa. According to Babinet this does not change the intensity of the magnetic scattering contribution (although the phase would do so). However, the assumptions of Babinet's theorem, namely that the contrast of the diffracting object is inverted everywhere, are not fulfilled: the pinhole aperture does not change its contrast upon helicity reversal. The diffraction of the pinhole interferes with the magnetic scattering and, hence, is responsible for the observed effect upon helicity reversal.

If the intensity for scattering of left and right circular polarized radiation are added the summed speckle pattern becomes identical to the intensity pattern recorded with linear polarization (Fig. 2.7(a)).

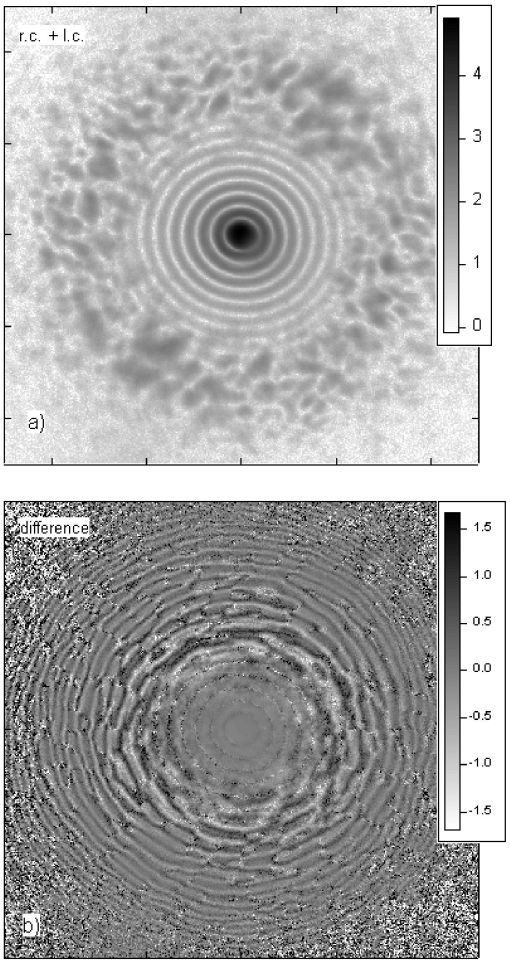

Figure 2.7: *(a) Sum of intensities from scattering of right (Fig. 2.6(b)) and left (Fig. 2.6 (c)) circular polarized light. (b) Difference of both circular polarization. The pure pinhole-magnetic scattering interference remains.*

Now, all pinhole-magnetic domain interference vanishes:

$$\begin{aligned} I_r + I_l &= \left|\mathcal{F}_q\left\{f_c + f_m\right\}\right|^2 + \left|\mathcal{F}_q\left\{f_c - f_m\right\}\right|^2 \\ &\propto \left|\mathcal{F}_q\left\{f_c\right\}\right|^2 + \left|\mathcal{F}_q\left\{f_m\right\}\right|^2 + \mathcal{F}_q\left\{f_c f_m\right\} - \mathcal{F}_q\left\{f_c f_m\right\} \\ &= \left|\mathcal{F}_q\left\{f_c\right\}\right|^2 + \left|\mathcal{F}_q\left\{f_m\right\}\right|^2 \\ &= I_{lin}, \end{aligned}$$

where $\mathcal{F}_q$ denotes the Fourier transform of the bracket expression into reciprocal space. This is an illustration of the fact that linear polarization can be thought of as the superposition of right and left circular polarization and that orthogonal polarization channels cannot interfere.

The difference image $I_r - I_l$ in Fig. 2.7(b) shows the pinhole diffraction - magnetic scattering interference term, only

$$\begin{aligned} I_r - I_l &= \left|\mathcal{F}_q\left\{f_c\right\}\right|^2 + \left|\mathcal{F}_q\left\{f_m\right\}\right|^2 - \left|\mathcal{F}_q\left\{f_c\right\}\right|^2 - \left|\mathcal{F}_q\left\{f_m\right\}\right|^2 + 2\mathcal{F}_q\left\{f_c f_m\right\} + 2\mathcal{F}_q\left\{f_c f_m\right\} \\ &\propto \mathcal{F}_q\left\{f_c f_m\right\}. \end{aligned}$$

The possibility to switch on and off the interference of the diffraction pattern from the circular aperture with the magnetic small angle scattering is important to be taken into account. The aim of the experiments is to show the possibility to reconstruct the magnetic real-space structure from the coherent scattering pattern (cp. § 4). It turns out that it is necessary for the reconstruction to be successful to have interference of the pinhole diffraction pattern and the magnetic scattering. *I.e.* it is required that the experiments for reconstruction of magnetic domains are performed with circular polarized radiation.

2.5.2 Variation of Energy

After studying the polarization effects on the coherent scattering from magnetic material the energy dependence of the scattering cross-section is investigated next. The energy of the incident radiation is considered in the resonance strengths F which are determined by atomic transition matrix elements [4, 10, 32]. In section § 2.3 the forward scattering cross-section is shown to be related to the complex resonance strengths, hence, revealing their energy-dependence. The remainder of the section is organized as follows:

- Small angle scattering (SAS) from magnetic domains measured in transmission is presented concerning
  - the transmission and scattering spectra of a $CoPt$ multilayer that reveal strong variation of the small angle scattering intensity across the $Co\ L_3$ edge.
  - the evidence of magnetic scattering at the $Co\ L_3$ resonance.
- In § 2.5.2.2 the energy-dependence of the speckle intensity of a $CoPt$ multilayer is presented for
  - *linear* polarized soft x-ray photons.
  - *circular* polarized soft x-ray photons.
  - a magnetic $CoFe$ sample measured in reflection geometry.
- Experimental correlation values as function of energy are presented for
  - the coincidence of both pinhole diffraction and magnetic scattering measured with linear and circular polarization.
  - both diffraction and magnetic SAS compared to pure magnetic SAS.
  - charge (height) scattering and magnetic SAS in reflection geometry.
- And, finally, intensity correlations are simulated and discussed.

2.5.2.1 Small angle scattering from magnetic domains

Transmission and SAS spectra - While the forward scattering amplitude describes the absorption spectrum and magnetic dichroism signal of the sample, the small angle scattering intensity is proportional to the scattering cross-section σ_s (see § 2.3.1 and eqn. (2.14)). Again, we performed measurements on the $CoPt$ multilayer sample with perpendicular magnetic anisotropy (§ B and [14, 43]) at the UE56/1 SGM beamline BESSY II. Forward scattering in transmission is acquired by accepting only the specular intensity on the micro-channel plate detector. Alternatively, we can accept only the diffuse scattering from the magnetic structure allowing us to measure the scattering cross-section σ_s. The monochromator is used with 800 $lines/mm$ grating defining the energy resolution together with the entrance and exit slit dispersion (see Fig. C.2). The transmission spectra of the forward scattering (square symbols) and the diffuse magnetic scattering (circle symbols) of linear polarized photons are plotted in Fig 2.8. The transmission spectrum is recorded with $\Delta E = 0.18\ eV$ (entrance slit: 15 μm, exit slit: 15 μm) and the scattering spectrum is measured with $\Delta E = 0.4\ eV$ (slits: 30 μm/50 μm. Due to the thickness of 185 nm of the $CoPt$ multiplayer plus the SiN-membrane and the Pt buffer and cap layer the absorption is strong and transmission is small. The diffuse scattering cross-section σ_s increases with energy approaching the absorption edge. It should be maximum at the CoL_3 resonance. But the low transmission through the sample diminishes the scattering signal, *i.e.* actually the product of the scattering cross-section and the transmission $\sigma_s \cdot T$ is measured. The effect can be observed by comparing Fig. 2.8(a) and (b), where (b) shows the spectrum for a thin sample of just 50 layers of 4 nm Co and 7 nm Pt. For this sample absorption is less strong and the maximum of the diffuse magnetic scattering intensity is centered at the resonance.

The experiments presented in the following have been performed on the thick sample (a) in order to to increase magnetic scattering due to the high concentration of Co.

Evidence of magnetic SAS - The coherent scattering from the ferromagnetic $CoPt$ multilayer is already subject to § 2.5.1 where the influence of the polarization of the incident soft X-rays is investigated. The $CoPt$ sample is very advantageous because the magnetic and the charge scattering are well separated in space. Further, the magnetic scattering is very concentrated in a circular area with an average in-plane momentum transfer of $q = 32\ \mu m^{-1}$ (see Figs. 2.5 and 2.6). This facilitates the investigation of the magnetic scattering alone. To prove the speckle structure to be purely magnetic in origin, Fig. 2.9 shows the scattering from the same $CoPt$-multilayer and collimating pinhole setup recorded with 758.0 eV and 778.0 eV of incident radiation, respectively. Image (a) contains only the diffraction FRAUNHOFER rings from the 2.5 μm diameter pinhole. The magnetic scattering is not existing as the oppositely magnetized domains do not reveal a magnetic contrast. Hence, there is no magnetic structure and small angle scattering cannot occur from the domains. If we increase the soft X-ray photon energy to 778.0 eV the difference in magnetic scattering factors for the two types of domains becomes dominant and photon scattering from the magnetic domains can be observed (Fig. 2.9(b)). This agrees well with the measured scattering intensity in Fig. 2.8(a) and proves that the circular scattering pattern originates from magnetic structures.

As seen in this section the scattering amplitude is attenuated strongly by the limited transmission through the sample. Nevertheless, low intensity passes through the sample even at the resonance for the thick sample but to decrease acquisition time and to improve signal-to-noise ratio it is advantageous to decrease the energy of the incident photons a few electron volts towards the maximum intensity of the transmitted scattering signal. Doing so might raise the question whether the "detuning" somehow affects the coherent scattering pattern.

Near the XMCD resonance of $Co\ L_3$ the contrast between oppositely magnetized domains is maximum. With decreasing energy (off the resonance) the contrast reduces and a domain image taken would appear increasingly faint. Evidently, the individual domain arrangement is not affected and small angle scattering still occurs from the same scattering centers as at the resonance, just the intensity is reduced. This scenery is well observed in the former paragraph by measuring the overall scattering intensity at

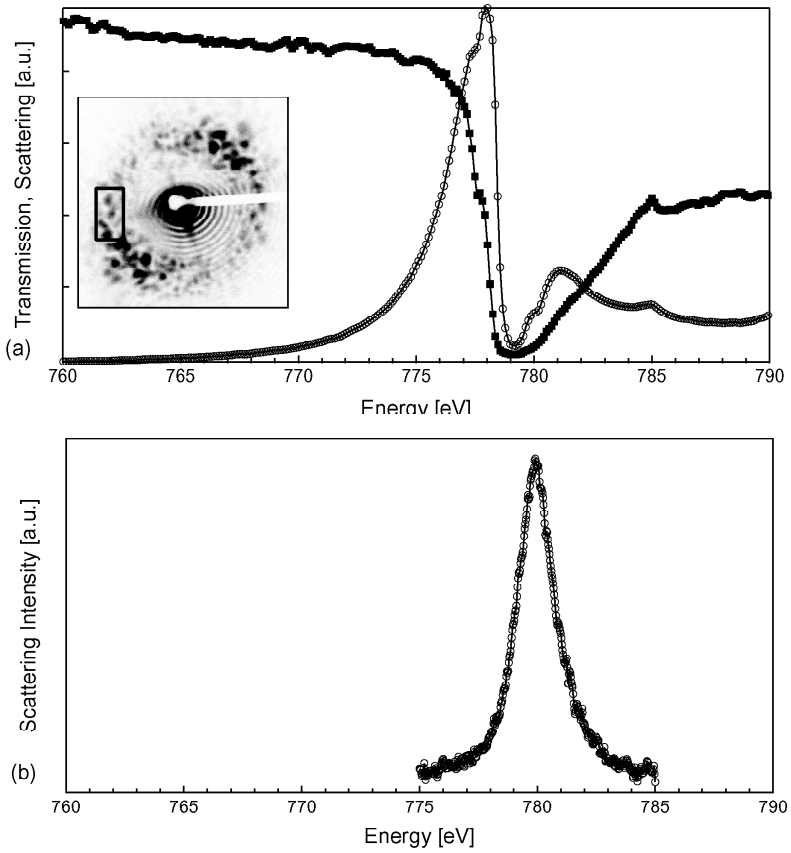

Figure 2.8: *(a) Transmission (squares) and diffuse scattering (circles) across the CoL_3 resonance of the thick $CoPt$ sample. The inset shows the region of interest (black rectangle) where the intensity of the scattering was measured during the energy-scan. The detectable scattering intensity is diminished by the absorption of the radiation at the resonance. (b) Diffuse spectra of a thin multilayer sample. For the thin sample the transmission is higher than for (a), hence, the scattered intensity peaks at resonance. In both cases the polarization is linear.*

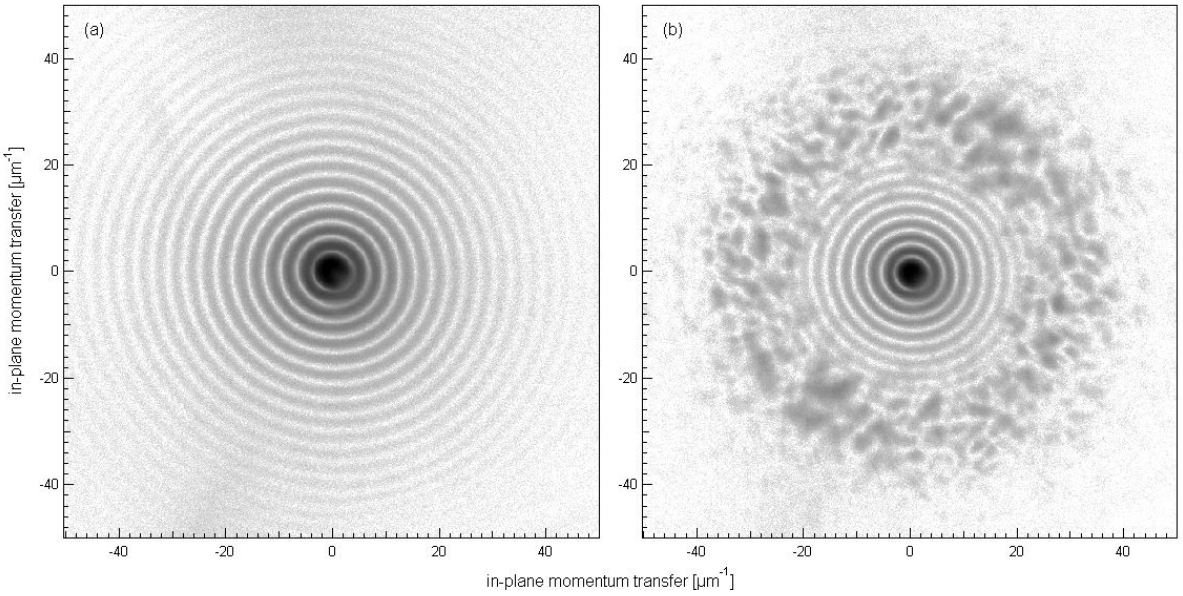

Figure 2.9: *(a) Scattering of* 758.0 *eV photons from the CoPt magnetic domain sample. No magnetic scattering is observable. (b) The same magnetic structure reveals magnetic SAS if the energy is tuned close to the L_3 absorption edge of Co (*778.0 *eV). For both plots the polarization of the incident synchrotron radiation is linear and the intensities are plotted in logarithmic scale.*

momentum transfer that corresponds to the average domain period (cp. Fig. 2.8). Consequently, one should not expect a change in the scattering pattern from absorption contrast alone.

In addition to the amplitude (absorption) contrast the phase of the scattered wave is influenced by the domains. It is less obvious to state whether the phase variation by energy variation affects the speckle pattern than to make a prediction about the influence of the absorption contrast. Therefore, the energy dependence of the scattering pattern is measured and the results are presented next.

2.5.2.2 Diffuse Scattering across the CoL_3 absorption edge

A compelling question is whether the pattern of the speckle distribution changes across the absorption edge due to the strong variation of the scattering factors. To get an answer the speckle pattern of the $CoPt$ worm-domains is measured by varying the photon energy across the L_3 resonance of the Co species.

Linear polarization - A section of each scattering pattern is presented in Fig. 2.10 with an indication of the corresponding photon energy of linear polarized soft X-rays. Far below the Co resonance only the diffraction pattern of the collimating pinhole is visible consistent with the result in Fig. 2.9. For increasing energy the magnetic scattering pattern becomes predominate revealing the magnetic speckle structure. The overall pattern of the individual speckle does not change across the absorption edge. Furthermore, although the transmission is low at and slightly above the resonance (images (7) and (8)) the magnetic speckle pattern is still visible because the magnetic scattering factor do not vanish for these energies. Note that the overall intensity is very similar for point (2) and point (7) but the scattering pattern is different because the magnetic scattering distribution is different for the corresponding energies.

Circular polarization - The same set of images is taken with right circular polarized soft X-rays of the same energies as in case of linear polarization (except the image taken above the XMCD maximum for linear photons lacks for the circular polarization because the intensity was too low). The result is

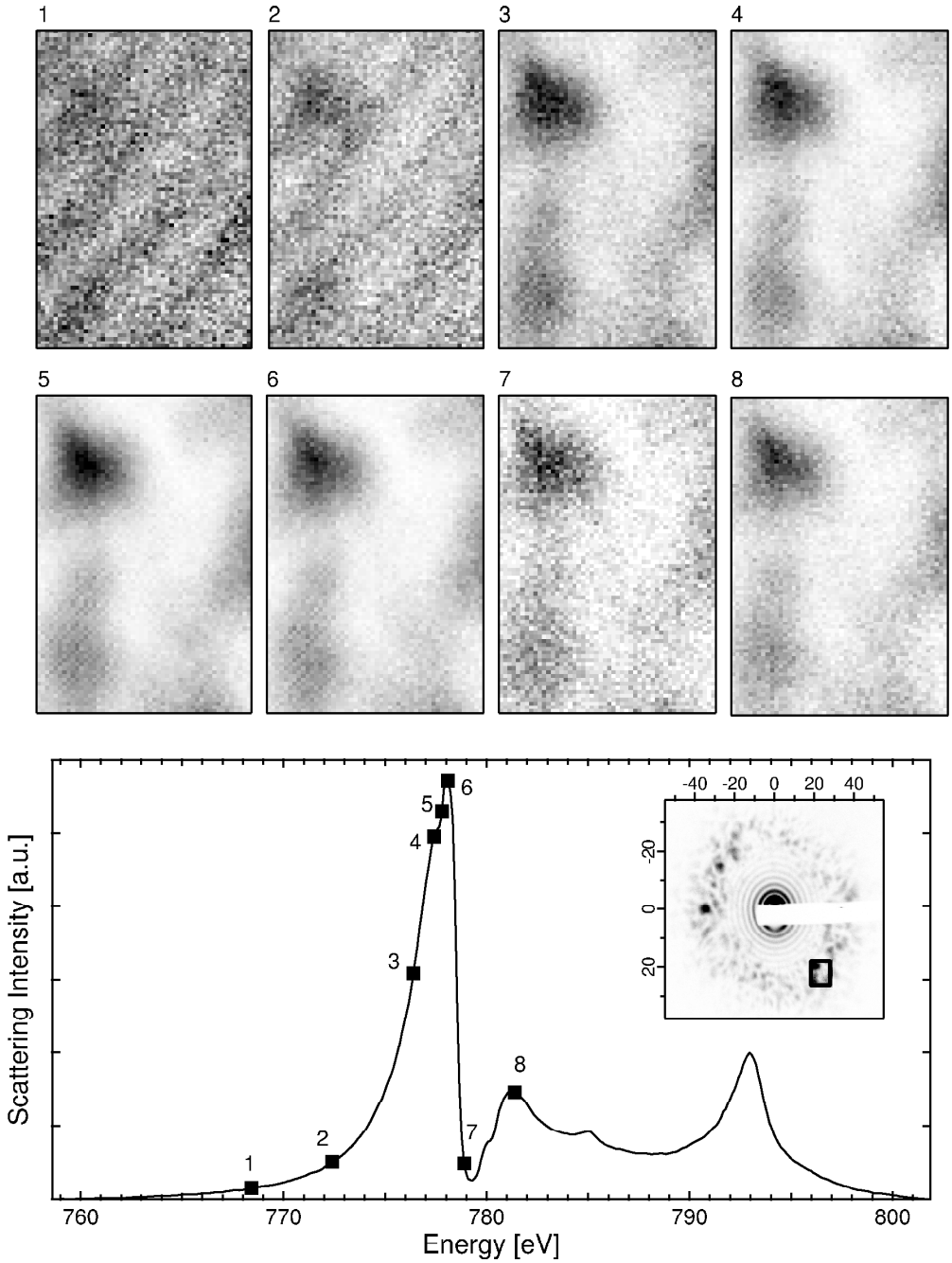

Figure 2.10: *Subsets of the two-dimensional speckle pattern acquired across the CoL_3 absorption edge for linear polarization. The q-range is horizontally from $q = 17.9\ \mu m^{-1}$ to $29.2\ \mu m^{-1}$ and vertically from $q = 17.6\ \mu m - 1$ to $26.8\ \mu m^{-1}$. The location of the subset in the complete Speckle pattern is depicted in the inset of the graph below. The curve shows the total scattering cross-section as function of energy to indicate the corresponding photon energy for the above speckle plots (black squares). The total scattering intensity is attenuated upon layer transmission near resonance.*

shown in Fig. 2.11. The location of the subsets is the same as in Fig. 2.10. Again the pinhole diffraction pattern dominates for low energies and, again, the magnetic scattering pattern does not change across the L_3 edge.

Magnetic $CoFe$ in reflection geometry - Additionally, we measured the energy-dependent scattering from a $CoFe$ layer in reflection. The $CoFe$ layer is sputtered on a $IrMn$ layer and pinned to the *anti*ferromagnetic $IrMn$ layer of unidirectional anisotropy. The ferromagnetic $CoFe$ forms domains if not exposed to an external magnetic field that exceeds the coercitivity. Although this system is of great interest concerning the investigation of exchange-bias effects and its applications [47], here this sample is just used to demonstrate the energy dependence of speckle patterns obtained from reflection experiments. Reflection scattering in grazing incidence is very sensitive to the surface topography [25–27, 29, 45]. Hence, the reflection experiments allow for enhancing the scattering from surface roughness relative to the magnetic scattering. As the non-magnetic surface roughness scattering interferes with the magnetic scattering the energy variation causes the speckle pattern to change across the Co resonance. Again subsets of the speckle pattern are plotted for various energies of the incident radiation, Fig. 2.12. The intensity pattern varies noticeably across the resonance. An explanation may be: the surface scattering does not vary much with energy variation. In contrast, the intensity contribution of the magnetic scattering to the total interference pattern varies across the absorption edge. *I.e.* for different energies the distinct contributions of surface and magnetic SAS vary and this might cause the change in the resulting speckle pattern. The quantitative investigation of this phenomenon is subject to section § 2.5.2.4.

The observations made so far are:

- In the transmission experiments shown the pattern of magnetic small angle scattering do not change with energy variation across the Co L_3 absorption resonance. When the magnetic contrast decreases for energies below the absorption edge the pinhole diffraction pattern becomes dominant. As long as the magnetic scattering dominates the speckle pattern no change of the pattern is observable by energy variation.

- In the reflection experiment presented the surface roughness scattering together with the magnetic scattering contributes to the total speckle pattern. The pattern changes with energy variation.

These observation gives reason to the following statement. If the coherent scattering is composed of two or more contributions the resulting speckle pattern changes if at least one of them is varied. This is also true if the lateral distribution that causes the small angle scattering remains unchanged.

2.5.2.3 Correlation of Magnetic Scattering Patterns

To evaluate the former observations quantitatively a degree of correlation is defined. The similarity of two two-dimensional patterns measured with an energy E and E_0 of the incident radiation can be calculated with [16, 48],

$$\gamma_{exp}(E, E_0) = \frac{\sum_{h,k}(M_{hk} - \bar{M}_{hk})(N_{hk} - \bar{N}_{hk})}{\left[\sum_{h,k}(M_{hk} - \bar{M}_{hk})^2 \cdot \sum_{h,k}(N_{hk} - \bar{N}_{hk})^2\right]^{1/2}}, \tag{2.15}$$

where M_{hk} and N_{hk} are the scattering data matrices to be compared with the corresponding mean values $\bar{M}_{hk}$ and $\bar{N}_{hk}$. For two identical images the correlation is unity, $\gamma_e xp = 1$. Uncorrelated patterns have a zero correlation value ($\gamma_{exp} = 0$), and anticorrelation is given if $\gamma_{exp} = -1$. The correlation values are calculated relative to a pattern at fixed energy E_0 (reference pattern). The reference pattern is acquired at the transmission minimum which is identical to the XMCD-maximum ($E_0 = 779.2\ eV$) where the domain contrast should be maximized (cp. Fig. 2.8(a)).

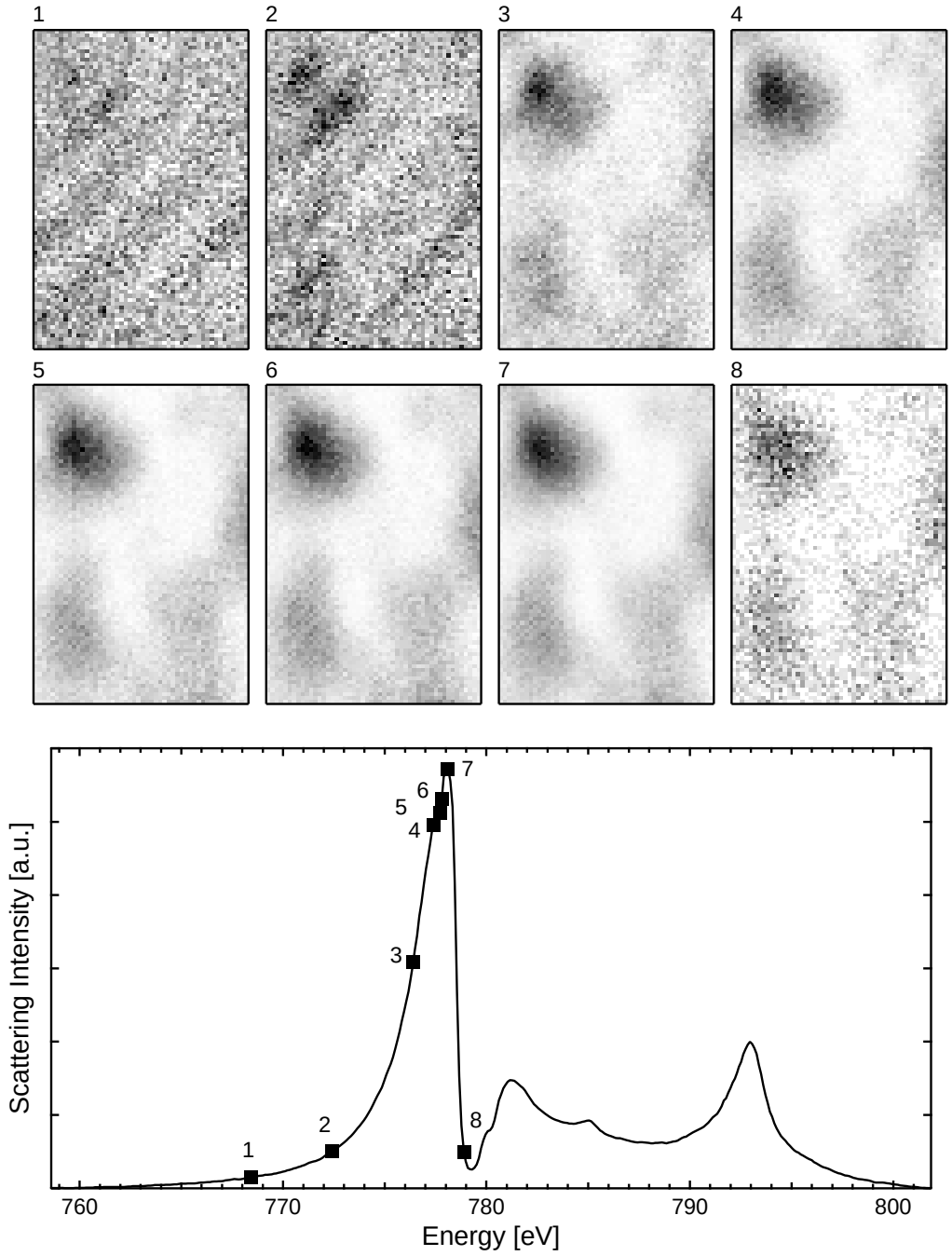

Figure 2.11: *Subsets of the two-dimensional speckle pattern acquired across the CoL_3 absorption edge for circular polarized soft X-rays. The q-range is the same as in Fig. 2.10. The graph below is a plot of the scattering intensity and the corresponding energies for the subsets are indicates with black squares.*

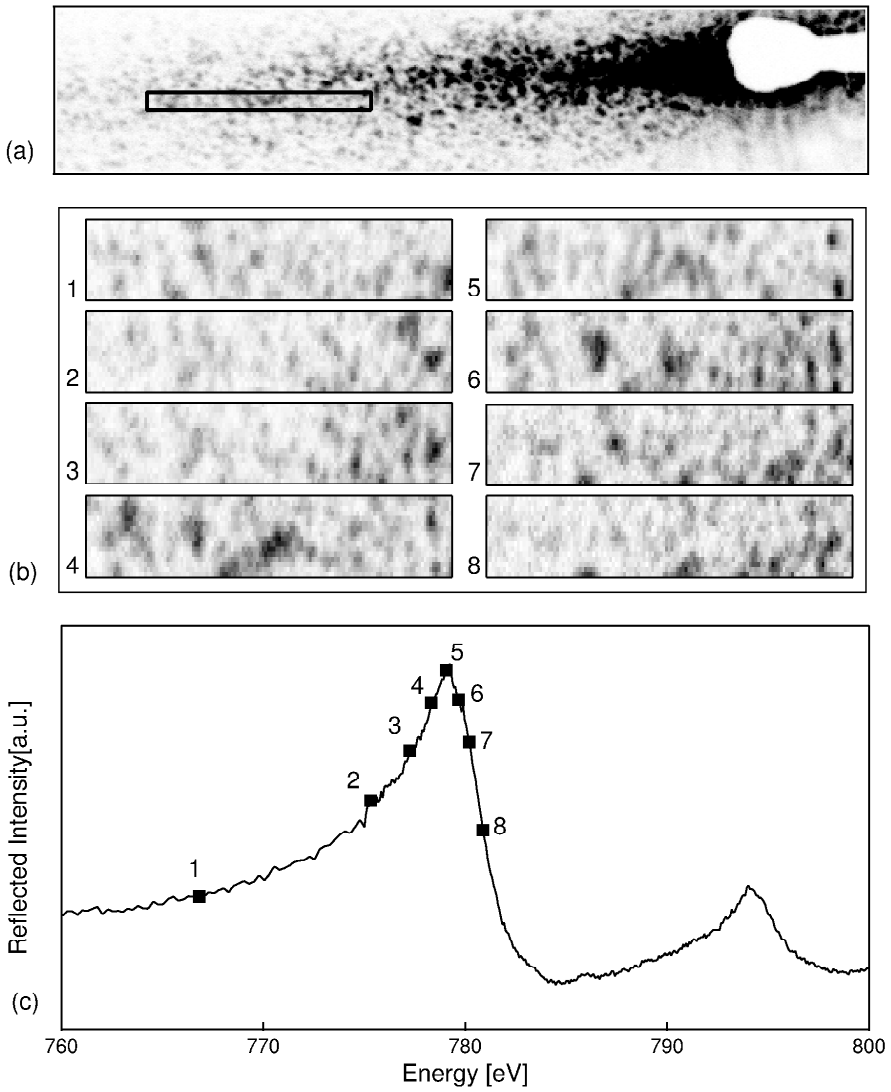

Figure 2.12: *(a) Two-dimensional scattering pattern from the CoFe surface measured in reflection geometry with $\theta_0 = 6°$ grazing incidence. The black square indicates the region of interest for which the pattern analysis has been performed. (b) Subsets of pattern cut from the scattering image (black square) for different energies of incident photons of circular polarization. The energy variies across the Co L_3 edge. (c) Co L_3 and L_2 edge measured in reflection with grazing incidence of $\theta_0 = 6°$. The corresponding energies of the subsets shown in (b) are indicated by black squares in the reflectivity scan.*

Pinhole diffraction and magnetic SAS, linear and circular polarization - In Fig. 2.13 the correlation values are plotted for two different regions of interest of the speckle pattern (marked areas). Region **A** is chosen around a momentum transfer of $q = 25\ \mu m^{-1}$ where the pinhole diffraction rings and the magnetic scattering have comparable intensities. In the center of region **B** the momentum transfer is $q = 36\ \mu m^{-1}$. In this region the magnetic scattering dominates because the FRAUNHOFER diffraction of the aperture is approximately 2 orders of magnitude lower in intensity (cp. Fig. 2.14).

The experiments were carried out with linear and circular polarized radiation. Following observations can be made:

The correlation is always higher for linear polarized photons than for circular polarized photons, *i.e.* the similarity of the speckle pattern is higher for a superposition of the pinhole diffraction and the magnetic scattering than for interference of both (cp. § 2.2).

Pattern taken with photon energies within $\pm 2\ eV$ show good similarity as it is confirmed by high correlation values of $\gamma_{epx} = 0.8$ for linear polarization and $\gamma_{exp} = 0.6$ for circular polarization.

In region B the pattern are more similar near resonance energy than in region A, *i.e.* the correlation values vary less for region B than for region A. This can be understood if we considered that in region A the impact of the pinhole diffraction on the magnetic scattering is higher than in region B.

The decay of the correlation values with decreasing energies is stronger for region B than for region A, *i.e.* the pattern vary stronger in region B than in region A if the magnetic scattering becomes less intense. This is easy to understand if we keep in mind that the magnetic scattering intensity decreases for low energies towards zero and only the pinhole diffraction remains. In region **A** the pinhole diffraction contributes strongly, due to comparable intensities of diffraction and magnetic scattering at resonance (see Fig. 2.14).

Both diffraction and magnetic SAS *versus* pure magnetic SAS - Now, the question arises whether for *pure* magnetic scattering the pattern is constant with energy variation. We used a sample-pinhole arrangement which allows to block the pinhole diffraction and to accept only the pure magnetic scattering. For that purpose the sample-pinhole setup is rotated around its vertical axis until the edge of the Si-wafer facet blocks the pinhole diffraction due to the distance of 380 μm from the pinhole to the facet (cp. Fig. 2.15(b)). A plot of the resulting speckle pattern is shown in Fig. 2.15(a). Plot (c) of the same figure shows the corresponding correlation values. Obviously, the pattern does not change for pure magnetic scattering even 5.7 eV below the XMCD-maximum, hence, the correlation values are constant and measure around $\gamma_{exp}(\Delta E) = 0.9$.

Reflection geometry, charge (height) scattering and magnetic SAS - In contradiction to the observation of weak pattern variation for the transmission experiment with low impact of the pinhole diffraction and the surface roughness, experiments in reflection geometry show strong pattern variation as already shown in § 2.5.2.2. The variation is also confirmed in low correlations to the reference pattern recorded at the $Co\ L_3$ resonance, Fig. 2.16. The roughness scattering from the surface of the $CoFe$ film influences the magnetic scattering. The coincidence of the two contributions causes the scattering pattern to vary strongly with energy variation.

2.5.2.4 Modelling of the Cross-Correlation

A lot of observations have been presented in the previous section that need further explanation. Therefore, it is desirable to know the impact of each contribution to the correlation function γ: the pinhole diffraction, the surface roughness scattering and the magnetic scattering. The basic idea of the following derivation is to get an analytical correlation factor that contains explicitly these contributions, in order to be able to discuss the influence of the different contributions. Most of the derivation is according to

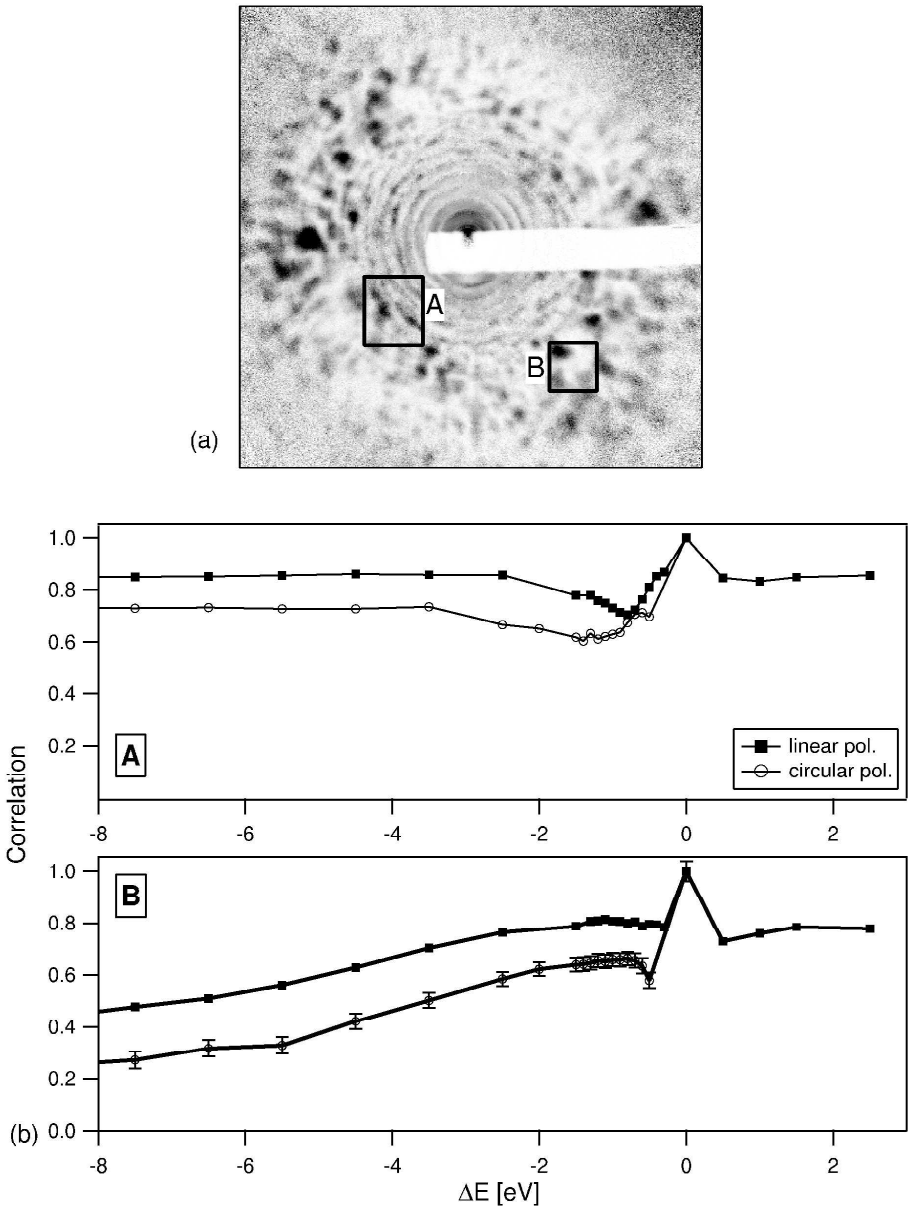

Figure 2.13: *(a) Image plot of the two-dimensional speckle pattern with marked region of interest.* **A** *is a region around* $q = 25\ \mu m^{-1}$ *of comparable intensities of the pinhole diffraction and the magnetic scattering. In region* **B** *around* $q = 36\ \mu m^{-1}$ *the magnetic scattering dominates the overall intensity by an order of magnitude (cp. Fig. 2.14). (b) Correlation values indicating the degree of pattern similarity for linear polarized (squares) and circular polarized (circles) radiation in region* **A** *and* **B**, *respectively. The pattern of reference is recorded at the energy of the Co* L_3 *XMCD-maximum.*

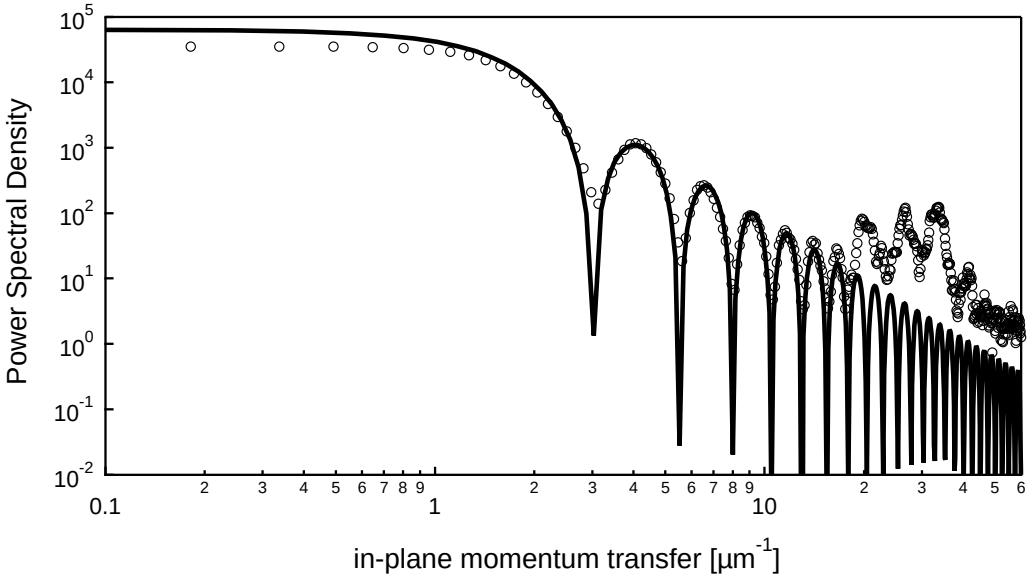

Figure 2.14: *PSD of the pinhole and magnetic domains obtained from experiment (symbols) at the scattering maximum,* 778.0 *eV. Calculated PSD of a* 2.5 *μm diameter pinhole (black line). The absolute intensities of the simulated pinhole diffraction are fitted by adjusting the relative intensity of the second minor maximum of the* FRAUNHOFER *ring to the measured intensity of that ring (cp. § A). Hence, the intensity of the pinhole diffraction can be compared to the measured scattering.*

the presentation of an analytical correlation factor in Ref. [16]. The derivation is based on an intensity correlation function. The scattering intensity can be expressed in form of Fourier transformed scattering factors for roughness and magnetic scattering. The Fourier expressions can be separated into the different terms for each contribution such that the mutual influence on the correlation can be discussed.

We start with the second-order intensity correlation function introduced in § 1.2.2,

$$\gamma_{(\Delta E=E-E_0)}(\mathbf{q}) = \frac{\langle I_{E_0}(\mathbf{q}) I_E(\mathbf{q})\rangle}{\left[\langle I_{E_0}(\mathbf{q})^2\rangle \langle I_E(\mathbf{q})^2\rangle\right]^{1/2}} \tag{2.16}$$

and substitute [16]

$$\langle I_{E_0}(\mathbf{q}) I_E(\mathbf{q}\rangle = \left|\Gamma_{(E_0,E)}(\mathbf{q})\right|^2 \tag{2.17}$$

and

$$\langle I_E(\mathbf{q})^2\rangle = \left|\Gamma_{(E,E)}(\mathbf{q})\right|^2 \tag{2.18}$$

where

$$\Gamma_{(E_0,E)}(\mathbf{q}) = \langle A_{E_0}(\mathbf{q}) A_E^*(\mathbf{q})\rangle \tag{2.19}$$

and

$$\Gamma_{(E,E)}(\mathbf{q}) = \langle A_E(\mathbf{q}) A_E(\mathbf{q})\rangle = \left|\langle A_E(\mathbf{q})\rangle\right|^2 . \tag{2.20}$$

The amplitude correlation function $\Gamma_{(E_0,E)}$ is expressed by the total scattering amplitude

$$A_E(\mathbf{q}) = \int d\mathbf{r} p(\mathbf{r}) e^{iq_z h(\mathbf{r})} f(\mathbf{r}) e^{i\mathbf{qr}}, \tag{2.21}$$

where $p(\mathbf{r})$ is the aperture function, $h(\mathbf{r})$ is the surface height function with perpendicular momentum transfer q_z, and

$$f(\mathbf{r}) = f_c + f_m = c(\mathbf{r}) e^{i\phi(\mathbf{r})}[1 + m(\mathbf{r})] \tag{2.22}$$

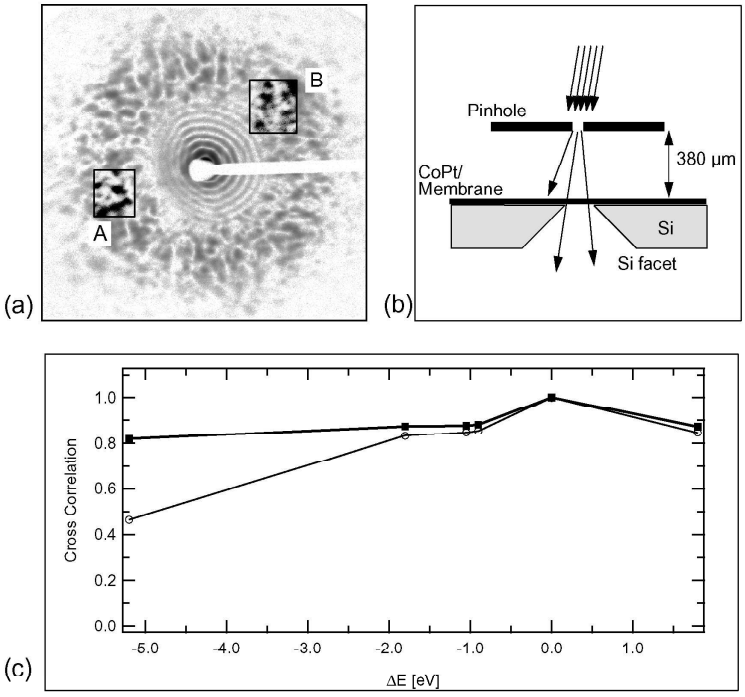

Figure 2.15: *(a) Image plot of the two-dimensional speckle pattern with screened* FRAUNHOFER *diffraction rings on the left. The squares indicate the regions of interest for the calculation of the correlation values. (b) Scheme of the sample setup. The collimating pinhole of* 2.5 μm *in diameter is set* 380 μm *in front of the sample membrane. By rotating the hole setup the diffraction rings of the pinhole are blocked by the facet. (c) Graph of the correlation values for the pure magnetic scattering region (squares) and the region of superposition of the diffraction pattern (circles). The radiation is linear polarized.*

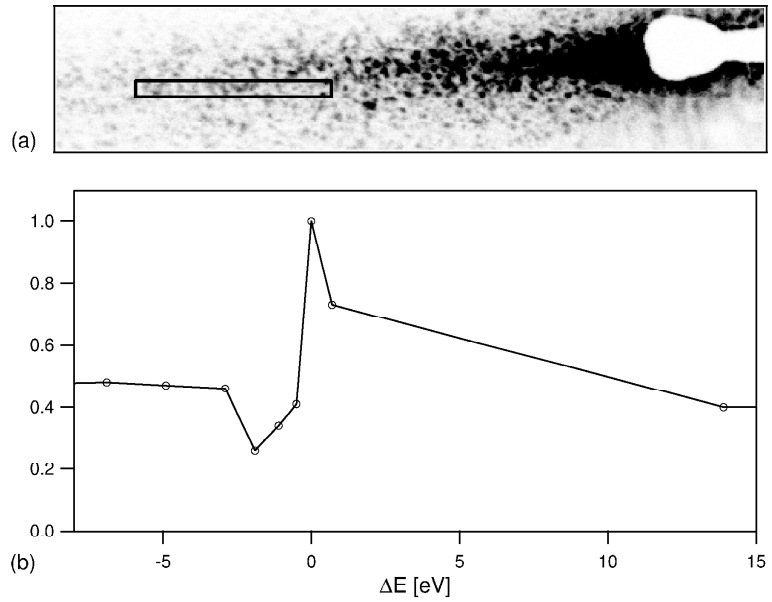

Figure 2.16: *(a) Two-dimensional speckle pattern of the $CoFe$ surface measured in reflection geometry. The photon energy is tuned the Co L_3 resonance at 779.2 eV and polarization is set to circular state. The correlation values are calculated from subregion marked in the image (black box). (b) Corresponding correlation values as function of ΔE referring to the pattern recorded at the Co L_3 resonance. The correlation is low confirming the above observation of non-similar patterns across the Co resonance.*

is the resonant magnetic scattering amplitude. Here $c(\mathbf{r})$ and $e^{i\phi(\mathbf{r})}$ are the average magnitude and the phase of the magnetic scattering amplitude f^{res}, respectively, with $\langle\phi(\mathbf{r})\rangle = 0$. The variation of of the scattering amplitude due to the magnetic domains is described by $m(\mathbf{r})$, also with zero mean, $\langle m(\mathbf{r})\rangle = 0$ [16]. The average magnitude $c(\mathbf{r})$ may be included into the aperture function

$$p(\mathbf{r}) \rightarrow p_c(\mathbf{r}) \begin{cases} c(\mathbf{r}) & \mathbf{r} \in \textit{aperture} \\ 0 & \mathbf{r} \notin \textit{aperture}. \end{cases} \tag{2.23}$$

Using eqn. (2.21) the amplitude correlation eqn. (2.19) can be written,

$$\Gamma_{(E_0,E)}(\mathbf{q}) = \left\langle \iint d\mathbf{r}_1 d\mathbf{r}_2 p_c(\mathbf{r}_1) p_c(\mathbf{r}_2) e^{iq_z[h(\mathbf{r}_1)-h(\mathbf{r}_2)]} e^{i\left(\phi_{E_0}-\phi_E\right)} \right.$$
$$\left. [1+m_{E_0}(\mathbf{r}_1)][1+m_E(\mathbf{r}_2)] e^{i\mathbf{q}(\mathbf{r}_1-\mathbf{r}_2)} \right\rangle. \tag{2.24}$$

The surface roughness and the magnetic structure are considered to be spatially independent. Hence, the ensemble average $\langle\rangle$ is taken separately for both terms. We assume that the surface roughness can be described by Gaussian distributed height fluctuations [16, 45],

$$\left\langle e^{iq_z[h(\mathbf{r}_1)-h(\mathbf{r}_2)]} \right\rangle = e^{-q_z^2\sigma_h^2[1-\rho_h(\mathbf{R})]}, \tag{2.25}$$

where the distance of two points in the surface is defined by $\mathbf{R} = \mathbf{r}_1 - \mathbf{r}_2$. σ_h is the rms-roughness of the surface and $\rho_h(\mathbf{R})$ is the autocorrelation function of the surface height. If the surface is assumed to be a self-affine fractal surface then the autocorrelation function can be described by [16, 45],

$$\rho_h(\mathbf{R}) = e^{-(|\mathbf{R}|/\xi_h)^{2h_r}}, \tag{2.26}$$

where ξ_h is the fractal cutoff length for the roughness and h_r is a roughness-parameter that is defined by the fractal dimension $D = 3 - h_r$. A finite cutoff length ξ_h is introduced *e.g.* to describe a finite size of

the surface [45]. $0 < h_r < 1$ describes the texture of the surface roughness, *i.e.* if h_r is small the surface is very rough and for h_r approaching unity the surface becomes smooth [45]. The Fourier transform of the surface autocorrelation function $\mathcal{F}_q\{\rho_h(\mathbf{R})\}$ is equal to the power spectral density (PSD) of the surface which can be obtained experimentally from atomic force microscopy (AFM) (see Fig. 2.5).

Since the intensity correlations are evaluated here, only $\left|\Gamma_{(E_0,E)}(\mathbf{q})\right|^2$ is relevant and the phases $e^{i(\phi_{E_0}-\phi_E)}$ are neglected for the following derivation. The correlation of the magnetic scattering intensity may be expressed as,

$$\langle[1+m_{E_0}(\mathbf{r}_1)][1+m_E(\mathbf{r}_2)]\rangle = 1+\langle m_{E_0}(\mathbf{r}_1)m_E(\mathbf{r}_2)\rangle\,. \tag{2.27}$$

If the magnetic domain distribution has a zero mean, $\langle m(\mathbf{r})\rangle = 0$, *i.e.* the same total area of up and down domains. The magnetic-magnetic correlation function can be set to,

$$\langle m_{E_0}(\mathbf{r}_1)m_E(\mathbf{r}_2)\rangle = \sigma_{m,E_0}\sigma_{m,E}\rho_m(\mathbf{R}), \tag{2.28}$$

calling $\rho_m(\mathbf{R})$ the magnetic amplitude autocorrelation function that can be derived from the PSD of the magnetic domain distribution by Fourier transform, $\rho_m \propto \mathcal{F}_q\{PSD\}$. $\sigma_m = \sqrt{\langle m(\mathbf{r})^2\rangle}$, is the rms variation of the magnetic scattering amplitude. It can be expressed by the magnetic scattering factors $\sigma_m = |f'_m|^2 + |f''_m|^2$. The autocorrelation function $\rho_m(\mathbf{R})$ is a general expression, that can be describe any correlated magnetic domain structure. For example, a random magnetic domain distribution may be described by a Gaussian surface with a cutoff parameter ξ_m [16],

$$\rho_m(\mathbf{R}) = e^{-(\mathbf{R}/\xi_m)^2}.$$

Substituting eqn. (2.25) and eqn. (2.27) into eqn. (2.24) yields,

$$\Gamma_{(E_0,E)}(\mathbf{q}) = e^{-q_z^2\sigma_h^2}\int d\mathbf{R}\varrho_p(\mathbf{R})(1+\sigma_{m,E_0}\sigma_{m,E}\rho_m(\mathbf{R}))e^{q_z^2\sigma_h^2\rho_h(\mathbf{R})}, \tag{2.29}$$

where $\varrho_p(\mathbf{R}) = \int d\mathbf{r}p(\mathbf{r})p(\mathbf{r}+\mathbf{R})$ is the aperture correlation function. Proceeding with eqn. (2.29) and abbreviating the Fourier integral to $\mathcal{F}_q$ gives,

$$\begin{aligned}
\Gamma_{(E_0,E)}(\mathbf{q}) &= e^{-q_z^2\sigma_h^2}\mathcal{F}_q\left\{\varrho_p(\mathbf{R})\left(e^{q_z^2\sigma_h^2\rho_h(\mathbf{R})}+1-1+\sigma_{m,E_0}\sigma_{m,E}\rho_m(\mathbf{R})e^{q_z^2\sigma_h^2\rho_h(\mathbf{R})}\right)\right\}\\
&= e^{-q_z^2\sigma_h^2}\mathcal{F}_q\left\{\varrho_p(\mathbf{R})+\varrho_p(\mathbf{R})\left(e^{q_z^2\sigma_h^2\rho_h(\mathbf{R})}-1\right)+\varrho_p(\mathbf{R})\sigma_{m,E_0}\sigma_{m,E}\rho_m(\mathbf{R})e^{q_z^2\sigma_h^2\rho_h(\mathbf{R})}\right\}\\
&= e^{-q_z^2\sigma_h^2}\mathcal{F}_q\left\{\varrho_p(\mathbf{R})\right\}+\mathcal{F}_q\left\{e^{q_z^2\sigma_h^2\rho_h(\mathbf{R})}-1\right\}+\sigma_{m,E_0}\sigma_{m,E}\mathcal{F}_q\left\{\rho_m(\mathbf{R})e^{q_z^2\sigma_h^2\rho_h(\mathbf{R})}\right\}.
\end{aligned} \tag{2.30}$$

The aperture function $\varrho_p(\mathbf{R})$ is used as windowing function to set the integration limits of the second and third term of eqn. (2.30). Finally, the amplitude correlation function can be written in short form [16],

$$\Gamma_{(E_0,E)}(\mathbf{q}) = e^{-q_z^2\sigma_h^2}\left(P(\mathbf{q})+R(\mathbf{q})+M_{(E,E_0)}(\mathbf{q})\right), \tag{2.31}$$

with

$$P(\mathbf{q}) = \mathcal{F}_q\{\varrho_p(\mathbf{R})\} \tag{2.32}$$

$$R(\mathbf{q}) = \mathcal{F}_q\left\{e^{q_z^2\sigma_h^2\rho_h(\mathbf{R})}-1\right\} \tag{2.33}$$

$$M_{(E_0,E)}(\mathbf{q}) = \sigma_{m,E_0}\sigma_{m,E}\mathcal{F}_q\left\{\rho_m(\mathbf{R})e^{q_z^2\sigma_h^2\rho_h(\mathbf{R})}\right\}. \tag{2.34}$$

The corresponding denominator eqn. (2.20) can be evaluated by expressing the magnetic correlation as

$$\langle[1+m_E(\mathbf{r}_1)][1+m_E(\mathbf{r}_2)]\rangle = 1+\sigma_{m,E}^2\rho_m(\mathbf{R}), \tag{2.35}$$

again with the magnetic domain distribution to be assumed of zero mean, $\langle m(\mathbf{r})\rangle = 0$. Following the same derivation as above yields,

$$\Gamma_{(E,E)}(\mathbf{q}) = e^{-q_z^2\sigma_h^2}\left(P(\mathbf{q}) + R(\mathbf{q}) + M_{(E,E)}(\mathbf{q})\right), \tag{2.36}$$

with

$$M_{(E,E)}(\mathbf{q}) = \sigma_{m,E}^2 \mathcal{F}_q\left\{\rho_m(\mathbf{R}) e^{q_z^2\sigma_h^2}\rho_h(\mathbf{R})\right\}. \tag{2.37}$$

Hence, we get the expression for the intensity-intensity correlation function,

$$\gamma_{(\Delta E)}(\mathbf{q}) = \frac{\left(P(\mathbf{q}) + R(\mathbf{q}) + M_{(E_0,E)}(\mathbf{q})\right)^2}{\left[(P(\mathbf{q}) + R(\mathbf{q}) + M_{(E_0,E_0)}(\mathbf{q}))^2 (P(\mathbf{q}) + R(\mathbf{q}) + M_{(E,E)}(\mathbf{q}))^2\right]^{1/2}}. \tag{2.38}$$

The Fourier transform of the aperture correlation function $\mathcal{F}_q\{\varrho_p(\mathbf{R})\}$ for a circular pinhole with radius a is [20, 22, 49],

$$P(|\mathbf{q}|) = P_0\left|2\frac{J_1(|\mathbf{q}|a)}{|\mathbf{q}|a}\right|^2, \tag{2.39}$$

where P_0 is the peak intensity and J_1 is the Bessel function of first kind.

2.5.2.5 Discussion of the Analytical Correlation and Comparison to Experimental Results

A first observation may be the following: eqn. (2.38) is unity if the pinhole is infinitely large ($a = \infty$) and the surface is absolutely smooth ($\sigma_h = 0$), *i.e.* $P(\mathbf{q}) = R(\mathbf{q}) = 0$,

$$\begin{aligned}\gamma_{(\Delta E)}(\mathbf{q}) &= \frac{\left(M_{(E_0,E)}(\mathbf{q})\right)^2}{\left[(M_{(E_0,E_0)}(\mathbf{q}))^2 (M_{(E,E)}(\mathbf{q}))^2\right]^{1/2}} \\ &= \frac{(\sigma_{m,E_0}\sigma_{m,E})^2}{\left[(\sigma_{m,E_0}\sigma_{m,E_0})^2(\sigma_{m,E}\sigma_{m,E})^2\right]^{1/2}} = 1\end{aligned}$$

This agrees well with the experimental result shown in Fig. 2.15 for pure magnetic scattering. Aside from experimental uncertainties the correlation values are constant with ΔE and approximately unity.

For a q-box of comparable scattering intensities from the pinhole and the magnetic domains (see Fig. 2.14) the correlation of a reference pattern acquired at resonance energy $E_0 = 779.2\ eV$ to a pattern recorded several eV below the resonance decreases towards zero as seen experimentally in Fig. 2.13. This is confirmed by eqn. (2.38), too. For simplicity, let the surface be perfectly flat, *i.e.* $\sigma_h = 0$. Hence, we can neglect the second term $R(\mathbf{q})$. This is a good assumption for our sample and transmission scattering geometry, see § 2.5.1, stating that the surface in-plane roughness scattering due to a granularity of 20 nm occurs for much higher scattering angles than the magnetic scattering. Thus, eqn. 2.38 simplifies to,

$$\gamma_{\Delta E}(\mathbf{q}) = \frac{\left(P(\mathbf{q}) + \sigma_{m,E_0}\sigma_{m,E}\mathcal{F}_q\{\rho_m(\mathbf{R})\}\right)^2}{\left[(P(\mathbf{q}) + \sigma_{m,E_0}\sigma_{m,E_0}\mathcal{F}_q\{\rho_m(\mathbf{R})\})^2 (P(\mathbf{q}) + \sigma_{m,E}\sigma_{m,E}\mathcal{F}_q\{\rho_m(\mathbf{R})\})^2\right]^{1/2}}. \tag{2.40}$$

To be able to simulate the energy-dependent correlations it is necessary to know the relative intensities of the pinhole diffraction and the magnetic scattering. From Fig. 2.14 we know the relative intensities at the scattering maximum, $E = 778\ eV$. The calculated pinhole diffraction from eqn. (2.39) is fitted to the measured intensity of the second-order minor maximum of the Fraunhofer rings (see also § A.1). The magnetic PSD from Fig. 2.5(c) is calibrated to the measured scattering intensity at $q = 26\ \mu m^{-1}$. Hence, we can calculate the magnetic scattering intensity for each energy if the magnetic PSD is weighted by $\sigma_m = |f_m'|^2 + |f_m''|^2$ for the corresponding energy.

At the resonance energy $E_0 = 779.2\ eV$ the relative intensity of the pinhole diffraction for $q \approx 30\ \mu m^{-1}$ is 2 orders of magnitude lower than the magnetic scattering (cp. Fig. 2.17). That is why the pinhole diffraction may be neglected at the resonance energy. On the other hand, the magnetic term can be neglected 10 eV below the resonance energy. For the correlation between the on-resonance and the off-resonance case we thus obtain:

$$\gamma_{\Delta E}(\mathbf{q}) = \frac{(P(\mathbf{q}) + \sigma_{m,E_0}\sigma_{m,E}\mathcal{F}_q\{\rho_m(\mathbf{R})\})^2}{(P(\mathbf{q})\sigma_{m,E_0}\sigma_{m,E_0}\mathcal{F}_q\{\rho_m(\mathbf{R})\})}. \tag{2.41}$$

Simplifying and expanding the above expression yields,

$$\gamma_{(\Delta E)}(\mathbf{q}) = \frac{P(\mathbf{q})}{\sigma^2_{E_0}\mathcal{F}_q\{\rho_m(\mathbf{R})\}} + 2\frac{\sigma_E}{\sigma_{E_0}} + \frac{\sigma^2_E\mathcal{F}_q\{\rho_m(\mathbf{R})\}}{P(\mathbf{q})}. \tag{2.42}$$

The interference term σ_E/σ_{E_0} is negligible because $\sigma_E \ll \sigma_{E_0}$ (cp. Fig. 2.3). As $P(\mathbf{q}) \ll \sigma^2_{E_0}$ and $\sigma^2_E \ll P(\mathbf{q})$ the first and third term of eqn. (2.42) also approaches zero. As a result, the intensity-intensity correlation vanishes, *i.e.* we get uncorrelated patterns.

The state of polarization can also be taken into account in eqn. (2.40). In § 2.5.1 we learned that for linear polarized light no interference occurs of the diffracted beam from the pinhole and the scattered radiation from the magnetic domains. Hence, the squared bracket expressions of the correlation for incident linear polarized soft X-rays reduce to,

$$\gamma_{(\Delta E)}(\mathbf{q}) = \frac{P(\mathbf{q}^2 + (\sigma_{m,E_0}\sigma_{m,E}\mathcal{F}_q\{\rho_m(\mathbf{R})\})^2}{[(P(\mathbf{q})^2 + (\sigma_{m,E_0}\sigma_{m,E_0}\mathcal{F}_q\{\rho_m(\mathbf{R})\})^2)(P(\mathbf{q})^2 + (\sigma_{m,E}\sigma_{m,E}\mathcal{F}_q\{\rho_m(\mathbf{R})\})^2)]^{1/2}}. \tag{2.43}$$

Simulations of correlation values are shown in Fig. 2.18. The state of polarization is included. The correlation for linear polarized radiation is plotted with square symbols and for circular polarization with circle symbols. The main experimental results are confirmed. Linear polarization causes higher pattern correlation than circular polarization. Strong magnetic scattering in the corresponding q-range causes a constant correlation upon energy variation near-resonance, Fig. 2.18(a). For high q the correlation decreases rapidly with energy variation. Variation of the transmission due to absorption in the sample is not considered in the calculation.

Finally, we can conclude from the experimental and analytical results in this chapter some important statements about coherent resonant magnetic scattering:

Polarization - The polarization state of the incident radiation strongly influences the speckle pattern. In conjunction with the scattering geometry and the magnetization directions in the sample the polarization determines the possibility for interference of charge and magnetic contributions.

Energy variation - The answer to the initial question whether the speckle pattern changes with energy variation is: yes and no. *Yes* if interference or superposition in q-space of at least two of the contributing scattering terms is possible. *No* is the correct answer if there is pure scattering observable from one of the contributing scattering terms. To be more detailed,

- The speckle pattern of pure magnetic scattering does not depend on near-resonance variation of the energy.
- Both superposition intensities and interference of amplitude of pinhole diffraction and magnetic scattering cause a change of the individual speckle pattern. A prior condition is that the intensities of both terms are comparable in the q-space region of interest. *E.g.* the magnetic scattering intensity varies with energy and is its contribution to the total scattering is enhanced near $Co\ L_3$ resonance.
- For linear polarized soft X-rays and for the magnetization being parallel to the propagation direction of the incident light ($\hat{\mathbf{m}}\hat{\mathbf{n}}\hat{\mathbf{q}}$) the correlation of the on-resonance pattern to near-resonance pattern is higher than for circular polarization states due to the possibility of interference.

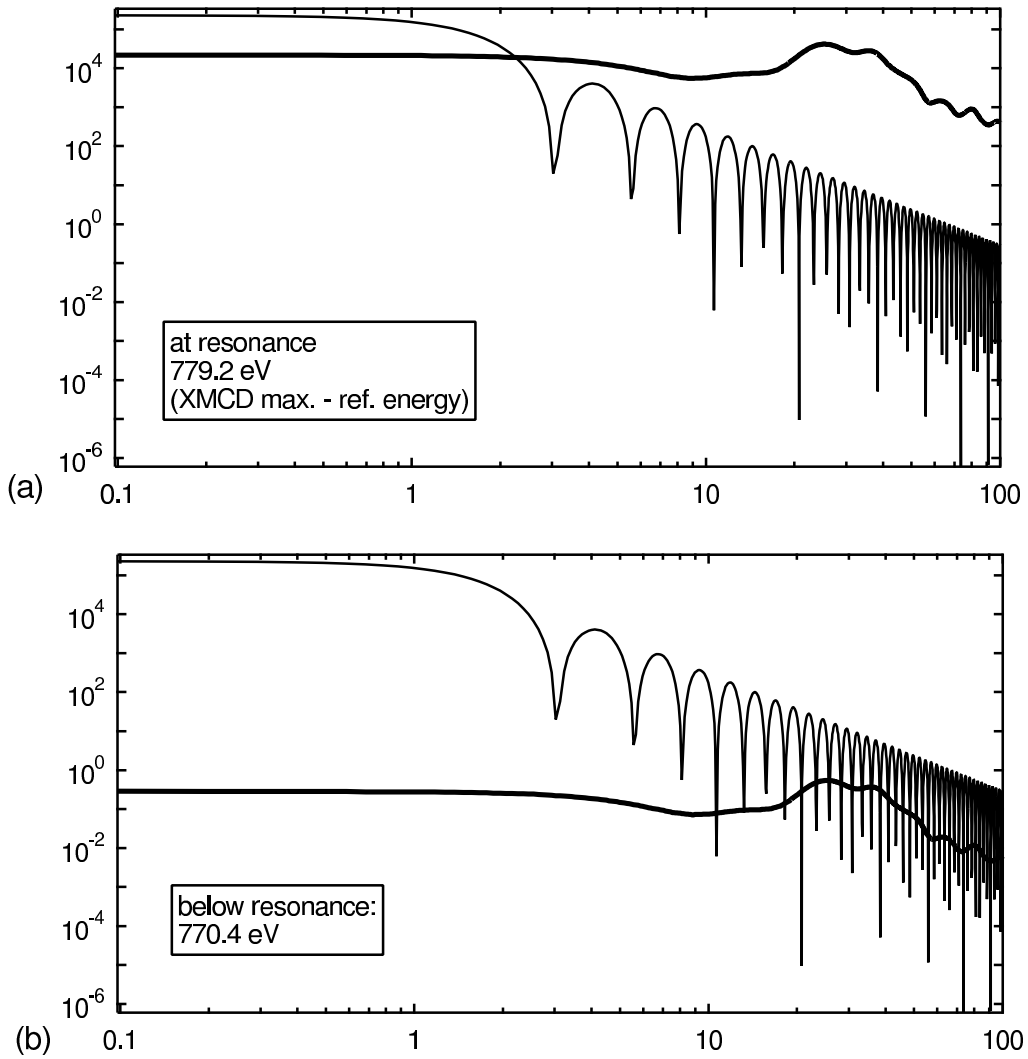

Figure 2.17: *PSD for the pinhole diffraction (thin line) and the magnetic scattering (thick line) obtained from the TXM-image in Fig. 2.5. The pinhole diffraction was calibrated to the measured intensity by adjusting the intensities of the second minor diffraction maximum the analytical diffraction pattern to the measured one (cp. Fig. 2.14). The PSD from the TXM-image was calibrated to the measured magnetic scattering as described in the text. (a) shows the relative intensities at resonance energy and (b) depicts the PSD for* 770.4 *eV, i.e. the magnetic PSD is weighted by the scattering amplitude.*

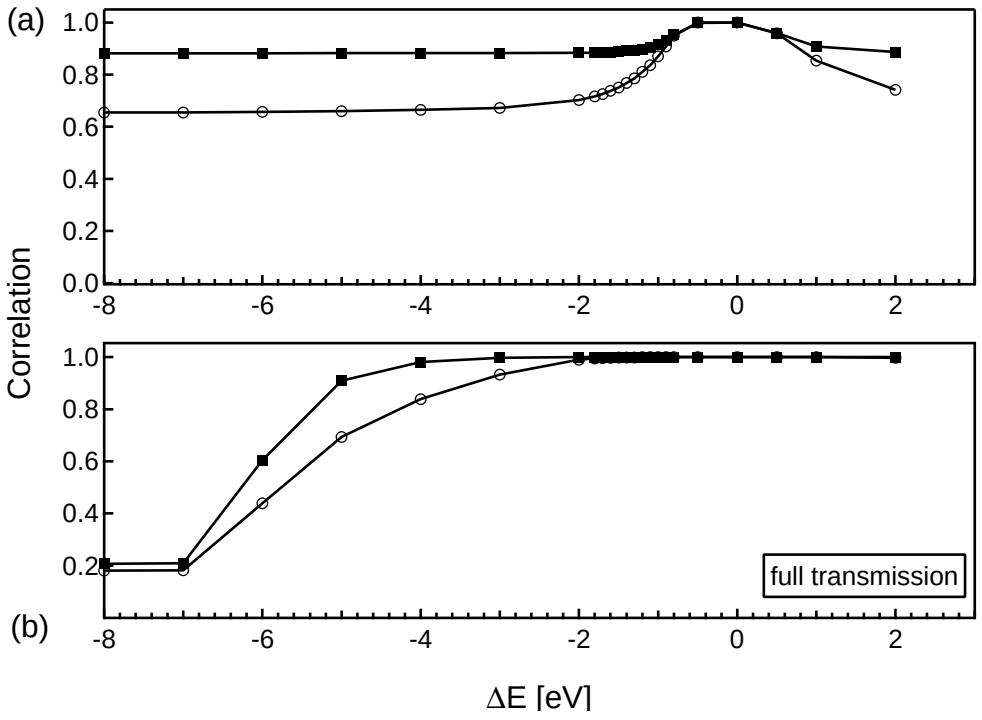

Figure 2.18: *Calculated correlation values using eqn. (2.40) for circular (circles) and linear (squares) polarization. The reference pattern is calculated for photons of the resonance-energy ($E = 779.2\ eV$). (a) The correlation is calculated for $q = 2\ \mu m^{-1}$ (low magnetic scattering contribution). (b) Correlation for $q = 43\ \mu m^{-1}$ (high magnetic contribution). The reduced transmission due to absorption of the radiation in the sample is not considered.*

Chapter 3

Phase retrieval and lensless imaging

Coherent scattering is sensitive to the sample individuality in the sense that the speckle fine structure observed in the diffraction pattern is sensitive to the sample fine structure beyond statistical averages (see § 1.1.4). Hence, one could say the real space structure is "encoded" in frequency space. The transition into the frequency space is mathematically described by the Fourier transform assuming perfect coherent conditions [20, 49]. Inverse transform is able to retrieve the original real space structure.

Hence, performing scattering experiments with coherent light allows for reconstruction of the real space object. Before realizing the imaging of objects by coherent scattering and inverse Fourier transform one has to overcome an immense obstacle: usually the wave magnitude and its phase cannot be measured separately, but only the intensity, *i.e.* only the squared modulus of the Fourier wave can be recorded. The phase information is lost in the intensity measurement. This well known phase problem makes it difficult to retrieve the real space object from its scattering pattern.

Nevertheless, a solution was found and it has been shown that the real space structure can be reconstructed from the measured intensity under certain conditions [50–59]. This chapter will present the fundamental tools for the phase retrieval, namely a reconstruction algorithm and its boundary conditions (constraints). A proposal of an advantageous sample-setup is made to overcome a hitherto performed patching technique that is often subject to discussions. Successful reconstructions of opaque objects are shown and discussed also under consideration of the limits for phase retrieval. The object reconstruction is finally extended to magnetic objects (see chapter 4).

3.1 Iterative reconstruction algorithm

3.1.1 The modified Gerchberg-Saxton algorithm

The fundamental idea of the algorithm is to make use of the Fourier transform relation between the object and the diffraction plane and to apply the algorithm iteratively. The latter helps to decrease the deviation between the calculated object and the actual object [50]. Initially, Gerchberg and Saxton used the measured intensities of *both* the image plane and the diffraction plane as input for their algorithm to retrieve the lost phase information. Fienup proposed a modified version of that algorithm that needs only the measured intensity of the diffraction or scattering pattern and renamed the retrieval procedure to *error reduction* algorithm [51]. Additionally, Fienup introduced boundary conditions to the algorithm that merely define constraints for the object (see also § 3.1.2). A schematic drawing of the algorithm is shown in Fig. 3.1(a). The Fourier space (index "f") is referred to as the plane of the diffraction or scattering pattern and the object space (index "r") is referred to as the plane of the real object. The algorithm starts in Fourier space with an amplitude proportional to the square root of the measured intensity

$$A_f(\mathbf{q}) = \sqrt{I_f(\mathbf{q})}$$

and a phase guess $\phi_f(\mathbf{q})$ of random numbers between $-\pi$ and π. An inverse Fourier transform is applied to the complex wave $A_f(\mathbf{q})e^{i\phi_f(\mathbf{q})}$ obtaining the first estimate of the real space object:

$$a_r(\mathbf{r})e^{i\phi_r(\mathbf{r})} = \int \sqrt{I_f(\mathbf{q})}e^{i\phi_f(\mathbf{q})}e^{-i\mathbf{qr}}d\mathbf{q}. \tag{3.1}$$

In a next step real space constraints (boundary conditions) are applied. These constraints are introduced in detail in section § 3.1.2. Next, the constrained object's amplitude and phase are Fourier transformed into reciprocal space. Now, the calculated amplitudes are substituted by the square roots of the measured intensity whereas the phases are maintained: the first cycle of the algorithm is completed. To get an estimate of the deviation between the calculated object and the actual object the mean squared error in the Fourier domain is calculated

$$E_f^2 = \frac{\int \left[|A_f(\mathbf{q})| - |F_f(\mathbf{q})|\right]^2 d\mathbf{q}}{\int \left[|F_f(\mathbf{q})|\right]^2 d\mathbf{q}}, \tag{3.2}$$

where $|F_f(\mathbf{q}| = \sqrt{I_f(\mathbf{q})}$.

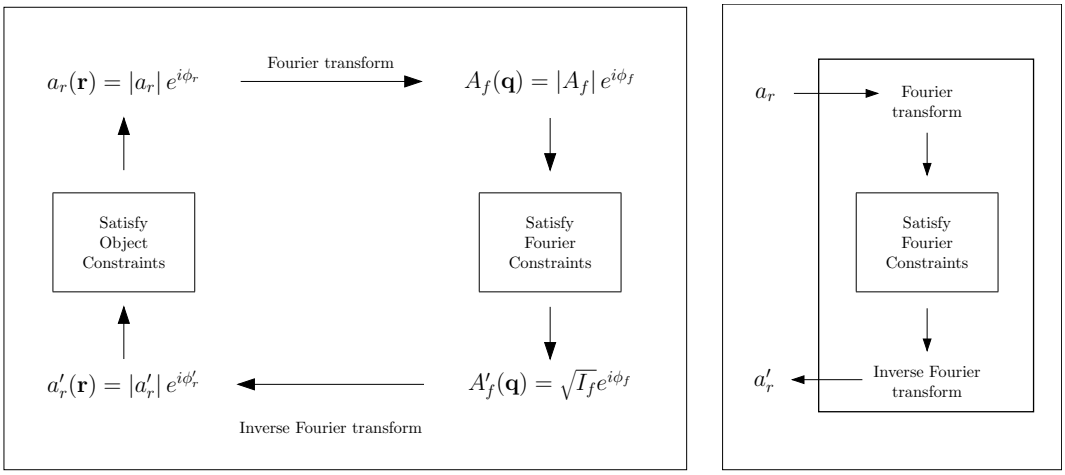

(a) (b)

Figure 3.1: *(a) Scheme of the error-reduction (ER) algorithm and (b) the hybrid-input-output (HIO) algorithm [51].*

3.1.2 Finite support and oversampling technique

In this section the idea of "constraints" or boundary conditions is introduced. Basically, the more knowledge about the object can be put into the reconstruction procedure the more probable is it that the algorithm procedure converges towards the correct solution. The knowledge about the object is applied to the algorithm in terms of boundary conditions or *constraints*, generally, either in the object or the Fourier space. The simpliest knowledge about the sample is its measured scattering pattern. This condition is put into the algorithm in Fourier space by substituting the calculated magnitude by the square root of the measured intensity.

The improvement of Fienup was to introduce a real space constraint that defines important properties of the object, as *e.g.* non-negativity or low spatial-frequency information [51]. The low spatial-frequency information may *e.g.* reduce the area of accepted amplitudes and phases to the shape of the object. The calculated real space object has to satisfy the following constraints:

$$a_r(\mathbf{r}) = \begin{cases} a'_r(\mathbf{r}) & \mathbf{r} \in S_r(\mathbf{r}) \\ 0 & \mathbf{r} \notin S_r(\mathbf{r}), \end{cases} \tag{3.3}$$

where $S_r(\mathbf{r})$ includes all points at which the constraint has to be fulfilled. S_r is often referred to as "support". First, the support defines the region over which the sample is extended. For example, if the sample has a circular shape and internal structure , then the support is given by the circular shape of the sample. Additionally, inside the support region the sample can be forced to fulfill additional conditions, like *e.g.* being non-complex or being an *anti*-phase object [54]. The support itself can either be initially known or being derived from the measured autocorrelation function of the sample. The latter approach is discussed below in detail (§ 3.2).

Mathematically, the Fourier inversion procedure must be able to solve a system of N non-linear equations for the amplitude and additional N non-linear equations for the phase, assuming that both the object and its Fourier magnitude are being sampled by a one-dimensional matrix of N elements. Of course, the phase is lost upon intensity measurements. To overcome this problem the *oversampling* technique is applied [51,60]. It has been shown that the phase can be retrieved if the Fourier magnitude is sampled twice as fine as the object [60–62]. If the 2-fold oversampled intensity pattern is Fourier transformed into the object space, the object of length N is embedded into an oversampled object of length $2N$. *I.e.* twice as much is known about the object as before the oversampling. As an illustration, consider the Fourier magnitudes of a simple hole measured with different sampling rates. Fig. 3.2(a) shows a 1-dimensional profile of a 2-dimensional FRAUNHOFER diffraction pattern of a circular aperture. The pattern is once sampled with 9 elements (circles) and once with 5 elements (squares) per FRAUNHOFER ring. The inversion of the corresponding two-dimensional matrices are shown in Fig. 3.2(b) and (c). The higher Fourier space sampling rate generates a larger real space area by Fourier transform. More elements of the real space object are known than with a smaller sampling rate. No additional oversampling is given with a Fourier sampling rate of one element for the FRAUNHOFER maximum and one element for the minimum (not shown). The oversampling factor Ω for scattering from a 2D object recorded on a 2D detector can be defined as the ratio of the real space area probed by the detector divided by the actual sample area. In the small angle scattering limit one obtains

$$\Omega_{2D} = \frac{(\lambda L)^2}{(SP)}, \tag{3.4}$$

where S is the sample area and P is the detector pixel area.

This oversampling technique is the main idea of the phase retrieval procedure presented in this work. The additional knowledge about the object due to oversampling is usually used as follows: The area around the object (white area around the black circle in the above example) is considered as being opaque. That means no transmission through this object region is possible. Hence, the constraint in the object space is is defined as putting all magnitudes and phases to zero values outside the actual object. In the experiments the zero-padded area is realized by a opaque mask (see § 3.2 and § 4.1.1). Mathematically, an oversampling of 2 is sufficient for each dimension but experimentally oversampling rates of 6 to 10 are necessary [60].

The possible oversampling is experimentally limited *e.g.* by the size of the detector pixel. The spatially resolvable elements of the micro-channel plate detector are only 400 pixel elements of 100 μm size. The oversampling rate can be increased by using a detector with more pixel per axis. For the experiments presented in chapter 4 a CCD camera is used with 2048×2048 pixel elements of $13.5\mu m \times 13.5\mu m$ pixel size. For technical details of the camera see § C. This enhances the oversampling by a factor of 5. Furthermore, the spatial resolution can be enhanced with this camera if at the cost of oversampling the sample-camera distance is reduced. Then the camera accepts a higher maximum momentum transfer q_{max} as before and hence, the smaller structures of the sample can be resolved.

3.1.3 The *hybrid-input-output* algorithm

FIENUP also extended the *error-reduction* algorithm by an *hybrid input-output* procedure similar to the negative feedback principle [51]. The only difference to the ER-algorithm is the modified input in the

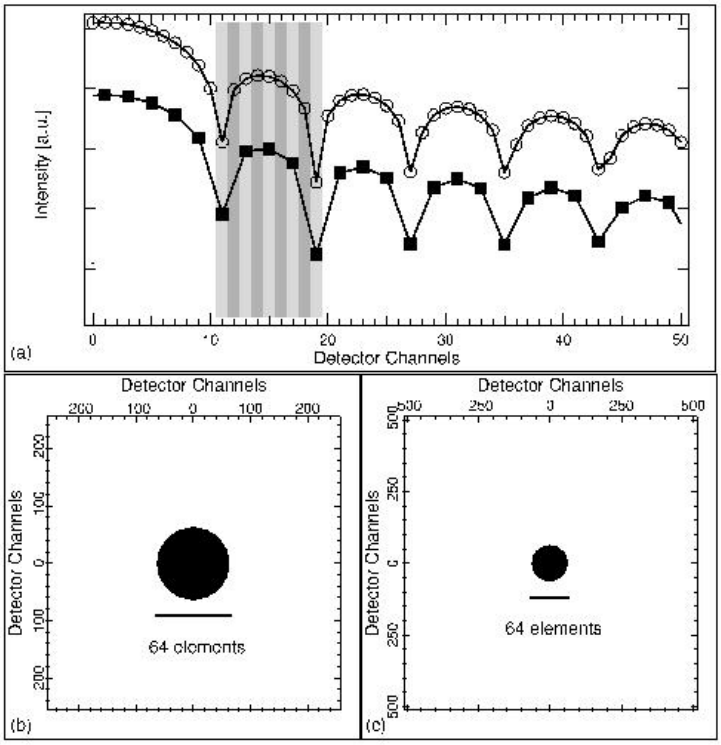

Figure 3.2: *(a) Different sampling rates for a diffraction pattern. (b) Real space object obtained by Fourier transform of the diffraction pattern recorded with small oversampling and (c) with large oversampling.*

object domain. The input for the $k+1$ algorithm cycle is set to the weighted difference of the output a'_k and the constrained input a'_k from the k-th step exactly there where the constraint is violated:

$$a_{k+1}(\mathbf{r}) = \begin{cases} a'_k(\mathbf{r}) & \mathbf{r} \in S_r(\mathbf{r}) \\ a_k(\mathbf{r}) - \beta a'_k & \mathbf{r} \notin S_r(\mathbf{r}). \end{cases} \tag{3.5}$$

The weighting factor β has typical values between 0.5 and 1.0. The lower condition of eqn. (3.5) can be understood as follows: the output a'_k violates the constraints outside the support S, hence, the input for the $k+1$ step is compensated for the violation by the difference of a_k and a'_k. In a lot of cases the so called HIO-algorithm successfully breaks stagnation of the ER-algorithm and, hence, speeds up convergence [51, 58, 60, 63].

In general, the constraints used for the reconstruction must be fitted to the individual problem. The next section demonstrates the phase retrieval by the ER-algorithm where only measurable information from the sample is used to determine the tight object domain support and, finally, to recover the real object from the scattered intensity.

3.2 Result - Lensless imaging at 3.1 nm wavelength

The following section demonstrates the feasibility of phase-retrieval from the scattering pattern generated by a transparent object on an opaque background using coherent soft x-rays [64]. The object consists of transparent structures drilled into a Au-film and forming a letter pattern. The freestanding Au-film has a thickness of 2 μm. For soft X-rays of 400 eV with 0.035 μm Au-attenuation length the film is opaque and, evidently, the apertures have full transmission. The holes are drilled with a focused ion beam (FIB)[1] and the resulting pattern is shown in Fig. 3.3. The object is real and non-periodic.

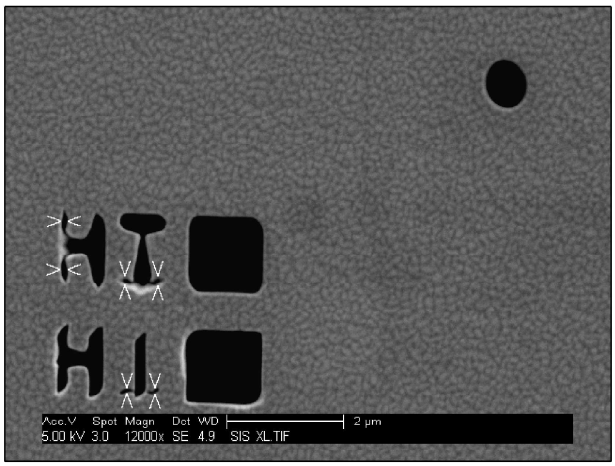

Figure 3.3: *Scanning Electron Microscope (SEM) image of the test sample [prepared by S. Andrews, SSRL, 2003]*

The pattern of interest is the double "HI■", contained in a region of about $3.3\mu m \times 3.5\mu m$ in size. The letters contain finer structure due to imperfect FIB sputtering as indicated on the image by white arrows. A reference pinhole of approximately 0.8 μm in diameter is placed in the right upper edge in a distance of 5.7 μm from the upper square of the letter pattern. The role of the reference pinhole is crucial for the reconstruction procedure because it allows to determine the support from the x-ray scattering image. This technique is discussed in detail in § 3.2.1.

[1] Courtesy of S. Andrews, Stanford Synchrotron Radiation Laboratory, 2003

The coherent x-ray scattering experiment was performed in transmission geometry at UE56−1/SGM beamline of the BESSY II synchrotron facility (see Fig. 3.4). Soft X-rays with a wavelength of $\lambda = 3.1\ nm$ (400 eV photon energy) were used. To satisfy both longitudinal and transverse coherence requirements the undulator radiation is monochromatized to $E/\Delta E \approx 5000$ and is then spatially filtered. The resulting longitudinal coherence length is given by $\xi_l = \frac{\lambda^2}{2\Delta\lambda} \approx 8\ \mu m$, which is larger than all possible optical path length differences in our setup. The spatial filter consists of a 50 μm pinhole 723 mm upstream of the sample and the fact that the sample is transparent only within an area of $6 \times 9\ \mu m^2$, respectively. The transverse coherence length at the sample position defined by the 50 μm pinhole is $\xi_{tr} = \frac{\lambda D}{\pi d} \approx 13\ \mu m$, *i.e.* the sample (consisting of the double HI■ pattern and the reference hole) is illuminated coherently. A 2D position sensitive detector is placed 990 mm downstream of the sample. The detector is based on a stack of five micro channel plates with a top CsI layer for photon-to-electron conversion and a 2D resistive anode readout. While the spatial resolution is only 100 $\mu m \times 100\ \mu m$ over the 40 $mm \times 40\ mm$ active area, the dynamic range (10^4) and the background noise level (10 $counts/s$ over the entire active area) are significantly superior to CCD devices, allowing to operate without a beam block for the zero order beam.

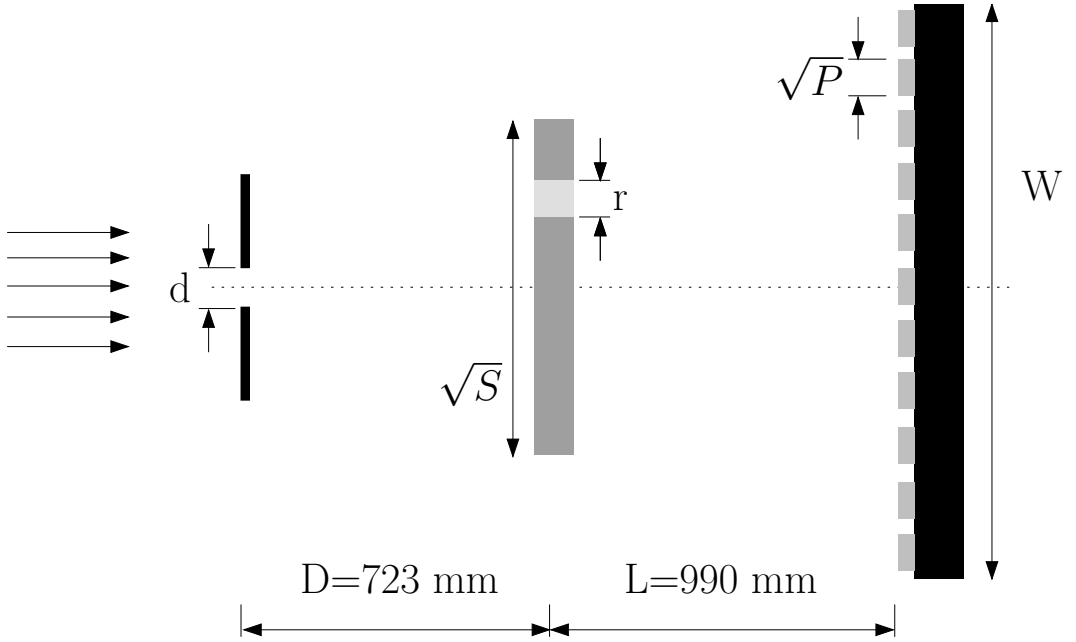

Figure 3.4: *Scheme of the experimental setup. Incident soft x-rays of wavelength* $\lambda = 3.1\ nm$ *pass through a pinhole of diameter* $d = 50\ \mu m$ *and are scattered by the sample, located* 723 mm *downstream.* S *denotes the sample area (*$6 \times 9\ \mu m^2$*) and* r *is the linear dimension of a resolvable element, determined by the maximum momentum transfer in the scattering experiment. A 2D detector is positioned at a distance* $L = 990\ mm$ *behind the sample. The linear detector size is* $W = 40\ mm$*, the area* P *of a spatially resolvable element is* $100 \times 100\ \mu m^2$*.*

The coherent diffraction pattern of 3.1 nm X-rays from this sample is presented in Fig. 3.5. The image is a sum of 10 subsequent measurements each with an exposure time of approximately 30 min. The average countrate on the detector is 2700 $counts/s$ which translates into an incident coherent flux of $2 \cdot 10^5$ $photons/s$ at the sample position, when the sample geometry and absorption is taking into account. The experimental chamber had to be set up 7 m downstream of the beamline focal position. Hence, an estimated fraction of only 5% of the total coherent flux available at this beamline under optimized conditions could be used.

Several features in the coherent diffraction pattern can be easily related to the pattern in the Au-film. The cross-like intensity originates from the "■"-apertures of the "HI■". A high frequency line

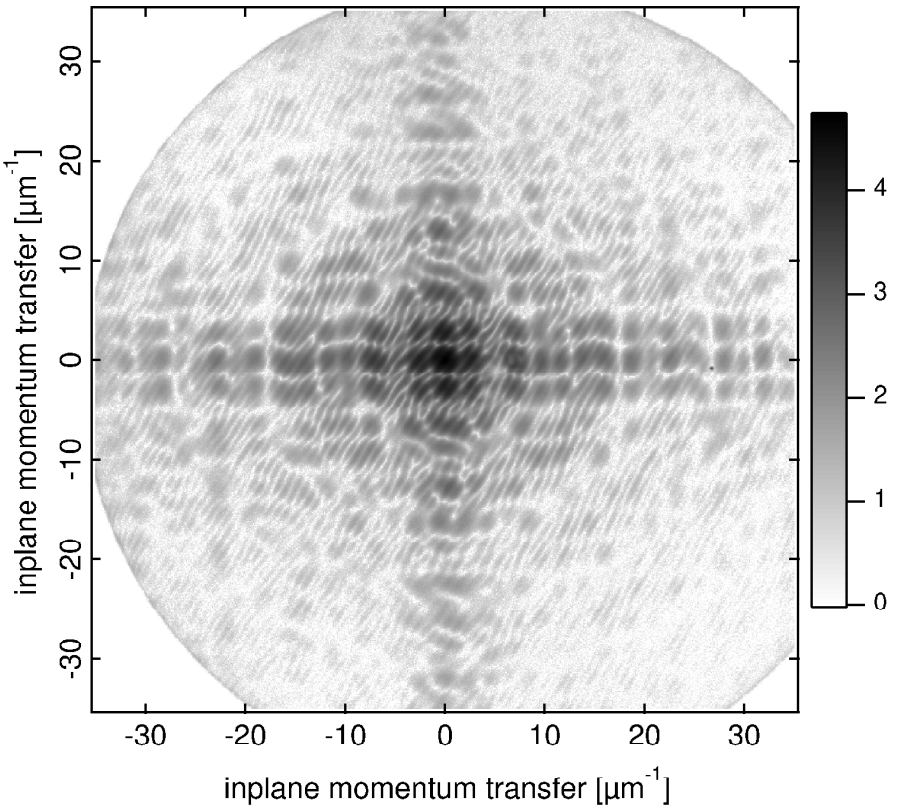

Figure 3.5: *Scattered intensity distribution on the two-dimensional position sensitive detector located* 990 *mm downstream of the sample. Intensity is shown in a logarithmic gray scale. The maximum momentum transfer of approximately* 35 μm^{-1} *results in an overall spatial resolution of* 180 *nm.*

pattern can be observed at about 45 degrees with respect to the central cross. This component is due to interference of X-rays photons passing through the reference pinhole and through the "HI■" pattern. The inverse line spacing in the high frequency pattern of approximately $q = 0.83\mu m^{-1}$ corresponds well to the real space distance of $d = 2\pi/q \approx 7.6\ \mu m$ of the reference hole to the transmission weighted center of the "HI■" pattern. The number of detector channels sampling the diffraction pattern of the largest spatial dimension determines the one-dimensional oversampling rate. The 400 resolvable detector elements cover a total range of $q_{det} \approx 80\ \mu m^{-1}$. Hence, $0.83\ \mu m^{-1}$ are covered by 4 channels, *i.e.* the $1D$ oversampling is $\Omega_{1D} = 4$. Also, a fairly weak Fraunhofer pattern of concentric rings can be observed, originating from the reference pinhole. At 3.1 nm x-ray wavelength the detector covers a maximum momentum transfer of approximately $q_{max} = 35\ \mu m^{-1}$ in the experimental geometry, corresponding to a maximum spatial resolution of 180 nm. It is important to note that the zero order beam has been recorded together with the rest of the diffraction pattern, giving access to information on a large spatial scale.

3.2.1 Determination of the support

We turn now to the crucial step of determing the support for the object domain constraint. The spatial autocorrelation of an object is connected to its shape and can thus be used to determine the rough support [58, 59]. The autocorrelation can easily be calculated by inverse Fourier transform of the measured scattering intensity[2]. The autocorrelation of an object obtained by Fourier transform of the diffraction pattern is known in crystallography as the "PATTERSON map". The more distinct and separated the regions of an object are the better and easier interpretable is the resulting correlation image. The aperture object in our experiment consists of a few very well separated patterns (the letters) and the reference pinhole probes the object itself very well. The size of the reference hole determines the spatial resolution of the probed objects in the PATTERSON map. The autocorrelation of the aperture object shows very distinct structures, see Fig. 3.6.

At the center of Fig. 3.6 the lateral offset is zero and the auto-correlation value maximal. At a positive and negative displacement that corresponds to the distance of the reference hole to the letter pattern the correlation is high again. This intensity corresponds to the convolution of each of the "HI■" letters with the reference hole. As a result, we obtain an estimate of the lateral size and shape of the real space object and on this basis we are able to define a real space support $S(\mathbf{r})$, as indicated in Fig. 3.6 (outlines). The support area consists of three separate regions, enclosing the reference hole and each of the "HI■" rows. Only one of the two mirrored images at positive and negative displacement is chosen. Of course, the result of the algorithm may always be the mirror image of the real object [51, 65].

For the object of interest it is known that the *Au*-film is opaque. With the help of the support the object domain constraint can now be defined. Outside the indicated shape the X-rays are attenuated, thus, the magnitude of the calculated object are set to zero-values. Inside the support area the calculated magnitude and phase of the object are floating in the algorithm as described in eqn. (3.3) of § 3.1.2.

3.2.2 Pattern Reconstruction

Now, all requisites for the first object reconstruction are known. We estimate a matrix of Fourier phases ϕ_f of random numbers of interval $-\pi \ldots \pi$ and create a complex Fourier wave together with the square roots of the measured intensity. After 150 iteration cycles of the ER-algorithm the real space object is reconstructed. The result is presented in Fig. 3.7. By comparing Fig. 3.3 and Fig. 3.7 one observes that the elliptical shape of the reference hole is recovered within the support around the hole. Furthermore, the overall structure and most of the fine structure in the "HI■" pattern is reproduced such as *e.g.* the change in width in the vertical line of the "I" in the top row. Several features marked by arrows in the SEM picture are not reproduced. These features have a characteristic width of 100 nm and are

[2] Autocorrelation theorem:

$$\mathcal{F}_q\{g(x) \circ g(x)\} = \mathcal{F}_q\{g(x)\} \cdot \mathcal{F}_q\{g(x)\} = |\mathcal{F}_q\{g(x)\}|^2 = I(q)$$

.

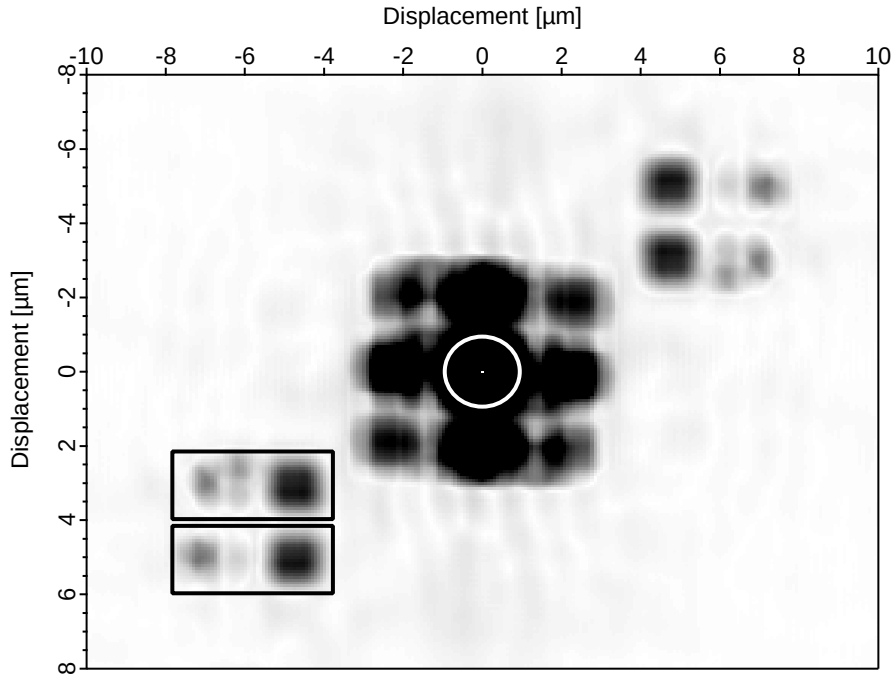

Figure 3.6: *Autocorrelation of the real space object determined from the recorded diffraction pattern in Fig.3.5. The outlines indicate the support chosen on the basis of the information from the autocorrelation.*

thus below the smallest structure size resolvable due to the maximum momentum transfer in the setup used here, which corresponds to 180 nm in real space. The same reconstruction pattern is obtained for different random start phases. This indicated that the obtained result is reliable.

In the small angle scattering limit, the spatially resolvable structure r is $r = 2\lambda L/W$, where W is the detector length in the scattering plane and L is the sample–detector distance (see Fig. 3.4). For this geometry, one obtains $r = 150\ nm$. The experimental value is slightly higher ($r_{exp} = 180\ nm$) as the zero order beam is not perfectly aligned to the center of the detector (Fig. 3.5). As a consequence, the effective detector width is reduced for some scattering directions. The 2D oversampling factor is according to eqn. (3.4) $\Omega_{2D} = 17$ for $S = 6\ \mu m \times 9\ \mu m$ and the detector pixel size of $P = 100\ \mu m \times 100\ \mu m$. Hence, the oversampling is large enough for the 2D problem and is about equal to the value determined experimentally from the high frequency oscillations: $(\Omega_{1D})^2 = 16$.

One pixel in Fig. 3.7 corresponds to a lateral size of 90 nm. The graph in the inset above the "HI■" pattern shows a profile cut through the reconstructed letter pattern. Each dot of the line represents one pixel in the image. The onset of a letter happens over two image pixels, hence, confirming the resolution of 180 nm that was calculated from the maximum momentum transfer q_{max}.

3.3 Discussion and modelling results

In the last section of this chapter we want to discuss some details of the algorithm and show possible improvements. First, we apply the HIO-algorithm in combination with additional internal constraints on the sample. Second, the advantage of a sample setup with a reference hole is discussed. Third, we discuss the influence of a beamblock covering the central peak in the scattering pattern.

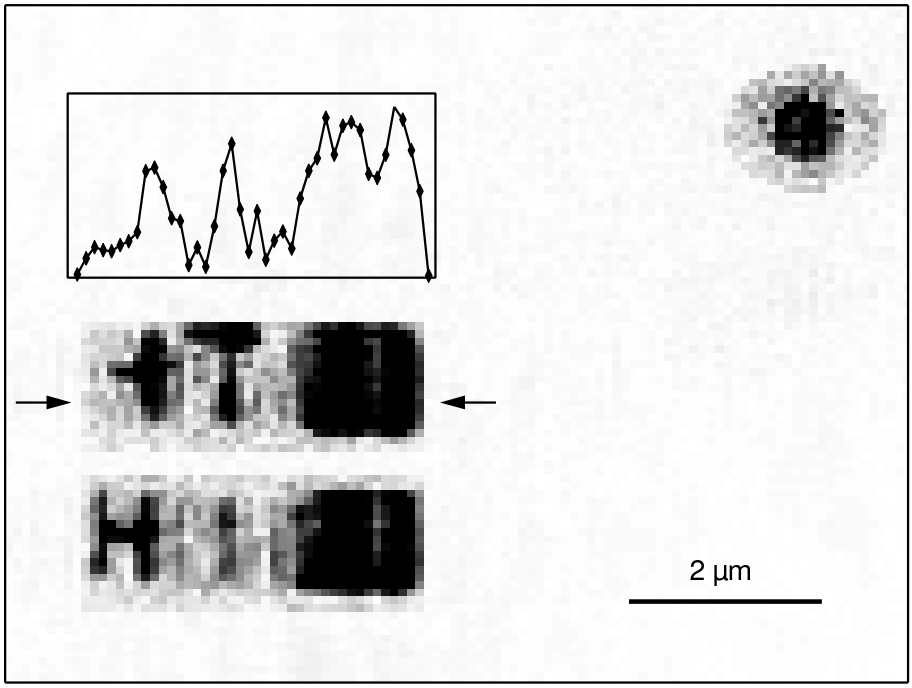

Figure 3.7: *(a) Reconstructed real space pattern of the Au-film. The detailed structures of the object are recovered. The resolution of the image retrieval is about* $180nm$*. The inset shows a profile cut through the letter pattern between the arrow indicators. The same reconstructed image is obtained for different random start phases giving reliability to the reconstructed object.*

3.3.1 Application of the HIO-algorithm

The algorithm procedure described above is very simple, but allows to reconstruct the object successfully. Nevertheless, further constraints and the application of the HIO-algorithm can slightly improve the retrieved image quality. Additional constraints are the so called internal constraints in contrast to the external constraints that are defined by the support. Further information of the object can be used to enhance the algorithm procedure. The apertures in *Au*-film are real objects, *i.e.* the their imaginary part equals zero. This knowledge is set into the algorithm by extending the object domain constraints to:

$$a_r(\mathbf{r}) = \begin{cases} \Re\{a'_r(\mathbf{r})\} + 0 \cdot \Im\{a'_r(\mathbf{r})\} & \mathbf{r} \in S_r(\mathbf{r}) \\ a_k(\mathbf{r}) - \beta a'_k & \mathbf{r} \notin S_r(\mathbf{r}). \end{cases} \tag{3.6}$$

The algorithm is started with the same support (Fig. 3.6). First, 100 steps of the ER-algorithm with constraints of eqn. (3.3) and the internal real-object constraint are performed, followed by 30 steps of the HIO-algorithm with eqn. (3.6)-constraints. Finally, 20 steps of the ER-algorithm are carried out. The Fourier space error eqn. (3.2) and the resulting object are shown in Fig. 3.8. The shapes of the apertures slightly sharper than in the previous ER-reconstruction. This is most notable at the reference hole and the second letter "I" in the lower row. The error increases strongly during the application of HIO-algorithm. This is typically observed [16, 66] and caused by the modified output outside the support.

3.3.2 The advantage of a known reference hole

Miao often uses low-resolution microscopy images to patch in the center part of the scattering image that can not be measured due to detector saturation caused by its limited dynamic range [53, 57, 67]. The use of a microscopy image, of course, is not always feasible if the reconstruction procedure shall be applied to *un*known objects. The micro-channel plate detector we used for the above experiment has a large dynamic range that allows the acquisition of the near-specular intensity. The center intensity

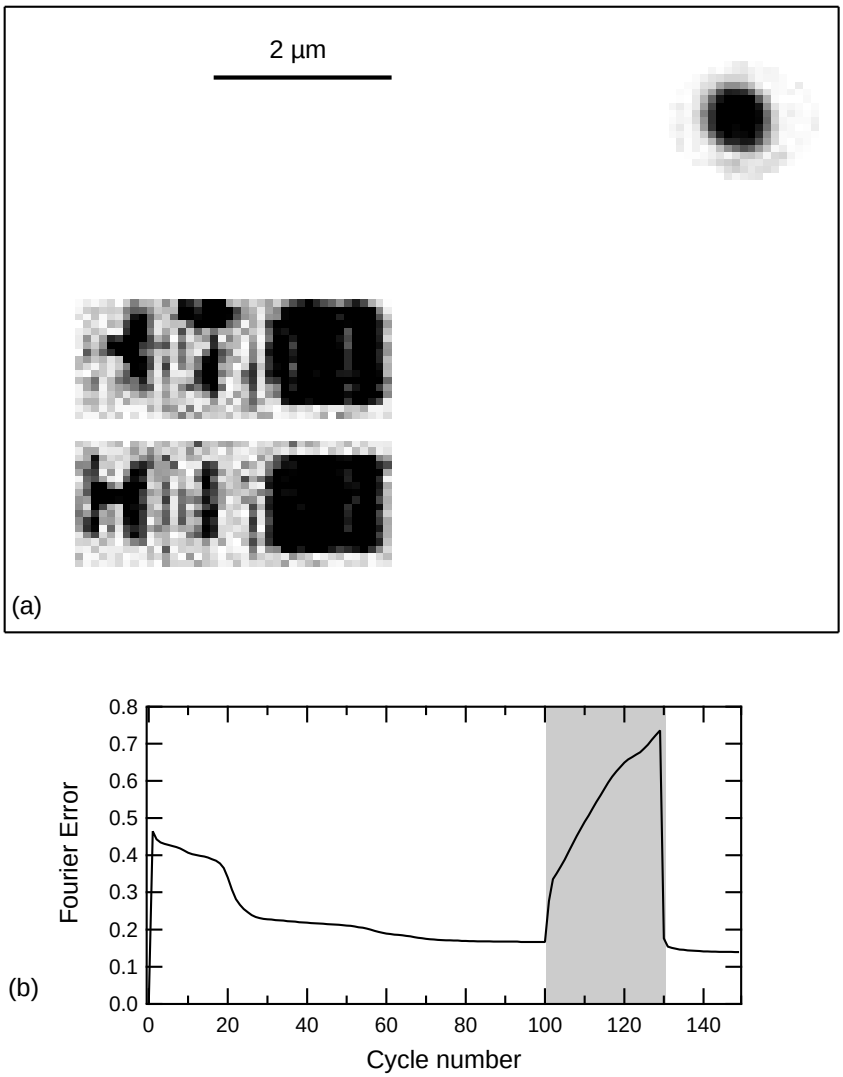

Figure 3.8: *(a) Reconstructed Au-pattern by application of the HIO-algorithm and by assumption of the object to be real. (b) The error in Fourier-space is plotted for each iteration cycle. The gray background indicates the application of the HIO-algorithm. Outside the gray region the ER algorithm was used.*

provides the information about the object on large length scales. But in general measuring the specular peak is (a) difficult due to saturation and (b) unreliable due to coexistence of transmission and forward scattering. The reference pinhole approach provides the near specular information. The reference hole probes the sample and allows for determing the long range dimension of the sample by calculating the autocorrelation from the measured intensity. This procedure was describes above.

It is desirable to increase high-q intensity to obtain information about smaller structure sizes. This can be achieved by increasing the total incident power of the synchrotron radiation. Hence, the parallel recording of the center and the diffuse scattering may become difficult. In this case it is advantageous to use a central beamblock in front of the detector. Now, the specular information is not available in order to extract the support for the object domain constraint. Still the autocorrelation can be helpful for the determination of the support, if the object has a suitable shape, *i.e.* distinct objects [58, 59]. This approach has been realized by arranging an object consisting of Au balls with an scanning tunneling microscope (STM) tip. One Au-ball is separated with the tip from other balls and acts as a separated reference scatterer [59].

In order to make the reference hole concept available for a wide variety of samples, the use of custom made sample holders is proposed here that includes the reference hole. Micro-technology and lithography allow the production of a sample holder system consisting of a reference hole laterally separated from a sample holder region (cp. Fig. 3.9). Both are structured *e.g.* into a Au-film which is sputtered on a SiN-membrane to allow transmission. There are several parameters which can be optimized to the objects under study. The size of the reference pinhole determines the smallest structure of the object which can be observed in the PATTERSON map, *i.e.* without reconstruction. Consequently, the pinhole should be made small enough such that the autocorrelation is sufficient to determine the shape of the object. Of course, the pinhole size cannot be reduced to any extent as (a) the transmission through the pinhole becomes low with small pinhole sizes and (b) nm holes with sufficient aspect ratio to block X-rays are difficult to produce.

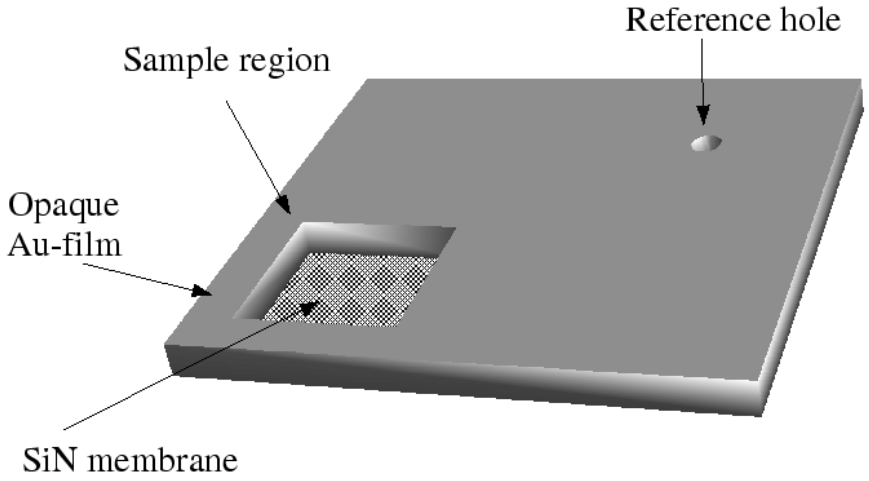

Figure 3.9: *Proposition of a microfabricated sample holder system. The SiN membrane is coated onto a Si wafer with an etched facet that allows transmission. A Au-film that is thick enough to be opaque for soft x-rays is sputtered onto the membrane. The rectangular region contains the sample that is reconstructed. The reference hole must be separated from the sample region by a distance that is larger than the sum of the diameter of the reference hole and the diameter of the sample region.*

A further parameter is the distance of the reference hole to the sample area. The autocorrelation contains a distinct sample region if the separation of the pinhole from the object is bigger than any distance within the sample area (cp. Fig. 3.6). Otherwise, the correlation area around displacement 0 cuts the area of the probed object like in Fig. 3.10(b). This makes the determination of a support difficult. Fig. 3.10(d) to 3.10(f) show the case for a well separated reference hole. The determination of a tight support for the object is much easier than before.

3.3.3 Compensating the lack of specular information

Although we are able to measure the specular peak of the diffraction pattern from the *Au* aperture sample and make use of this additional information in the reconstruction procedure, the reference hole already provides enough information about the large scale shape of the sample in many cases. However, in many experimental situations the specular beam does not only contain forward scattering information but also transmission intensity. The transmitted inntensity can not be easily separated from the scattering signal. As the algorithm is based on the assumption that the input is of pure scattering nature the reconstruction may become erroneous. Therefor, we test the possibility to reconstruct the object without knowledge of the central beam.

A central beamblock is experimentally favorable to increase the detectable flux at high momentum transfer as it avoids detector saturation in the center. Of course, the information contained in the specular peak is lost. One may ask how much of the specular information can be lost while still being able to reconstruct the object. To investigate this question, the measured intensity was blocked in the center by simulation. A circular area of increasing diameter is zero-padded for that purpose as shown in Fig. 3.11(a)-(c). Next, each manipulated intensity is used as input to the reconstruction algorithm as it is described in § 3.3.1. The same support is applied (cp. Fig. 3.6). The only extension to the above algorithm occurs in the Fourier domain. The zero-padded area is free-floating in the Fourier domain, *i.e.* the calculated Fourier magnitudes are not substituted by the input intensity but maintained. Of course, the rest of the magnitudes are set to the square roots of the measured scattering pattern. Hence, successful reconstructions will recover the scattering intensity in the near specular area (cp. Fig. 3.12). The results of the phase retrieval are shown in the right column of Fig. 3.11.

The reconstruction is feasible with a lack of near specular information ($q \approx 1.5\ \mu m^{-1}$) as shown in Fig. 3.11(a). The quality of the recovered object is even better than the image with the full intensity as input (cp. Fig. 3.8). The reason may be that slight detector non-linearity for high count rates is present. Hence, the specular intensity is probably recorded erroneously. The reconstructed object becomes worse with a lack of information up to $q \approx 3.1\ \mu m^{-1}$ in in-plane momentum transfer. Blocking a momentum transfer larger than $q \approx 3.6\ \mu m^{-1}$ prevents the reconstruction from being successful[3] (see Fig. 3.11(c)). In case of successful reconstruction with applied central zero-padding the Fourier magnitude is recovered in the free-floating area as shown in Fig. 3.12.

The insets in the left column of Fig. 3.11 show the autocorrelation of the object obtained from the zero-padded scattering intensities. For a blocking of $1.5\ \mu m^{-1}$ the autocorrelation still allows to derive the support because the letters are distinctly observable. A blocking of larger momentum transfers smears the autocorrelation and makes the determination of the support difficult.

The maximum momentum transfer that can be blocked without serious disturbances of the recovered structures is about $q \approx 3\ \mu m^{-1}$ what corresponds to a real space length of almost $2\ \mu m$. All information on larger length scales is lost due to the beam block. If the beamblock size is increased and blocks a momentum transfer that corresponds to the dimension of the largest letter size then the reconstruction fails. The set of simulations demonstrates the advantage of using a known reference hole as the object shape can still be determined from the PATTERSON image, although a part of the central beam is missing.

[3]The correlation value (eqn. 4.2.1) of the "HI■" patterns of (a) to (b) is $\gamma_I = 0.81$ and the correlation of (a) and (c) is reduced to $\gamma_I = 0.60$.

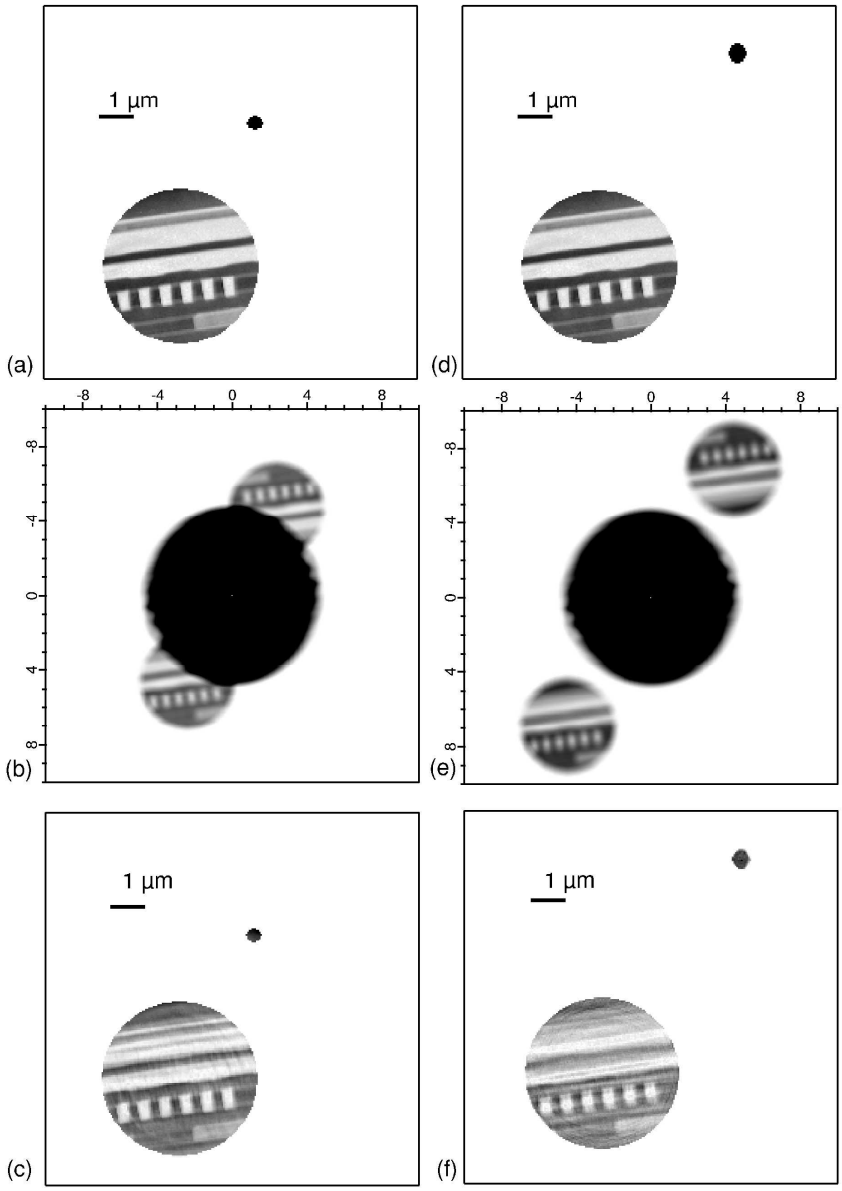

Figure 3.10: *(a) Test sample with distance of the reference hole shorter than the sample diameter. (b) Autocorrelation of (a) in µm-units of lateral displacement. The center-area cuts the object-area. The reconstructed object is shown in (c). (d) Same test sample but the distance of the reference hole is larger than the sample diameter. (e) The autocorrelation of (d) is distinct and given in µm-units of lateral displacement. (f) shows the reconstruction. The test-image is a subset of an transmission X-ray microscope image recorded from a vertical cross-section of an AMD processor unit. Courtesy of G. Schneider, BESSY 2003.*

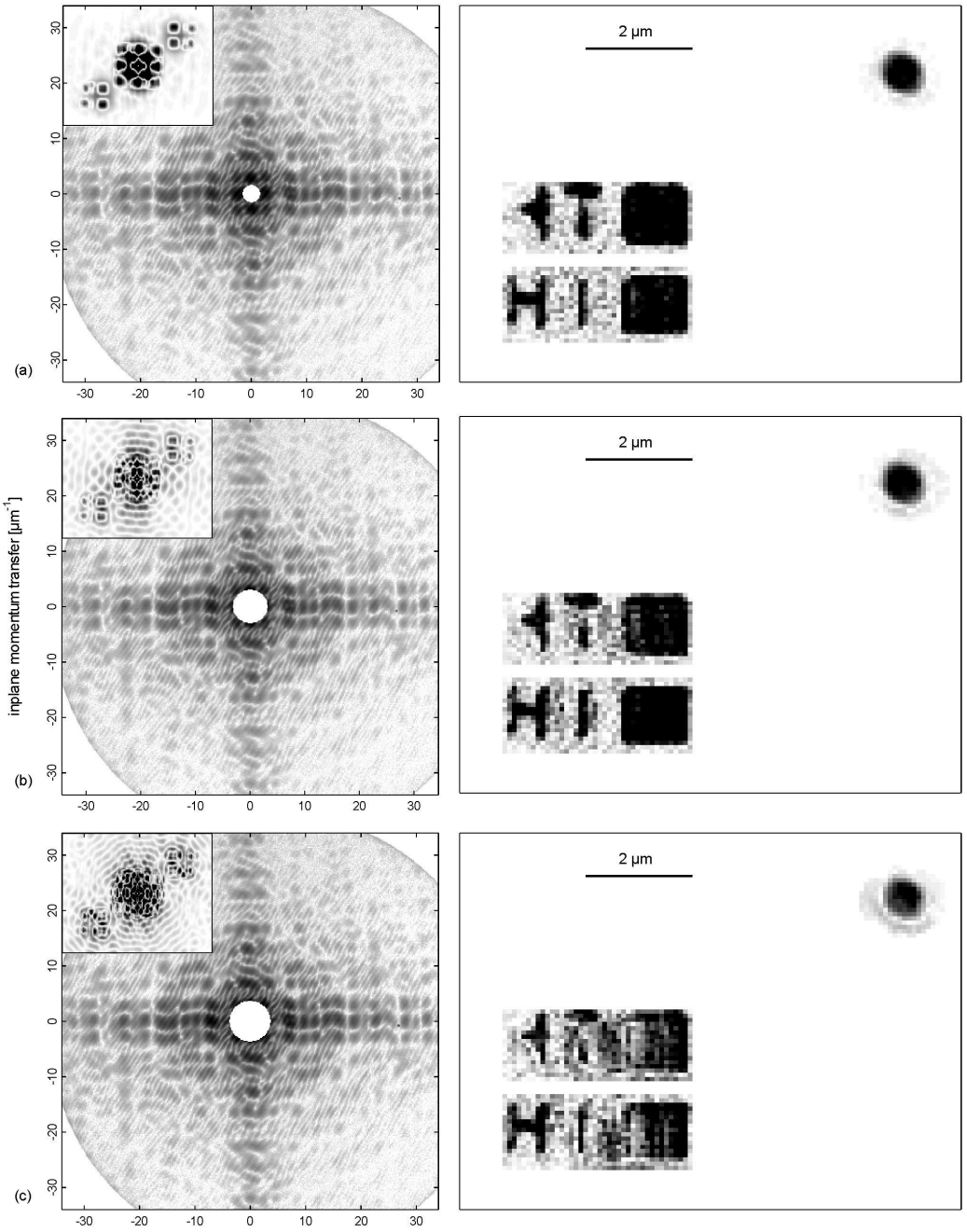

Figure 3.11: *Left column: logarithmic scale plots of scattering intensity with removed specular information increasing in diameter from (a) to (c). The maximum momentum transfer q lost due to the beamblock is (a): $q = 1.5\ \mu m^{-1}$, (b): $q = 3.1\ \mu m^{-1}$ and (c): $q = 3.6\ \mu m^{-1}$. The insets in the left upper corner of each momentum spectrum depict the corresponding autocorrelation obtained from inverse Fourier transform of the zero-padded scattering intensity. Right column: the corresponding reconstruction of the object.*

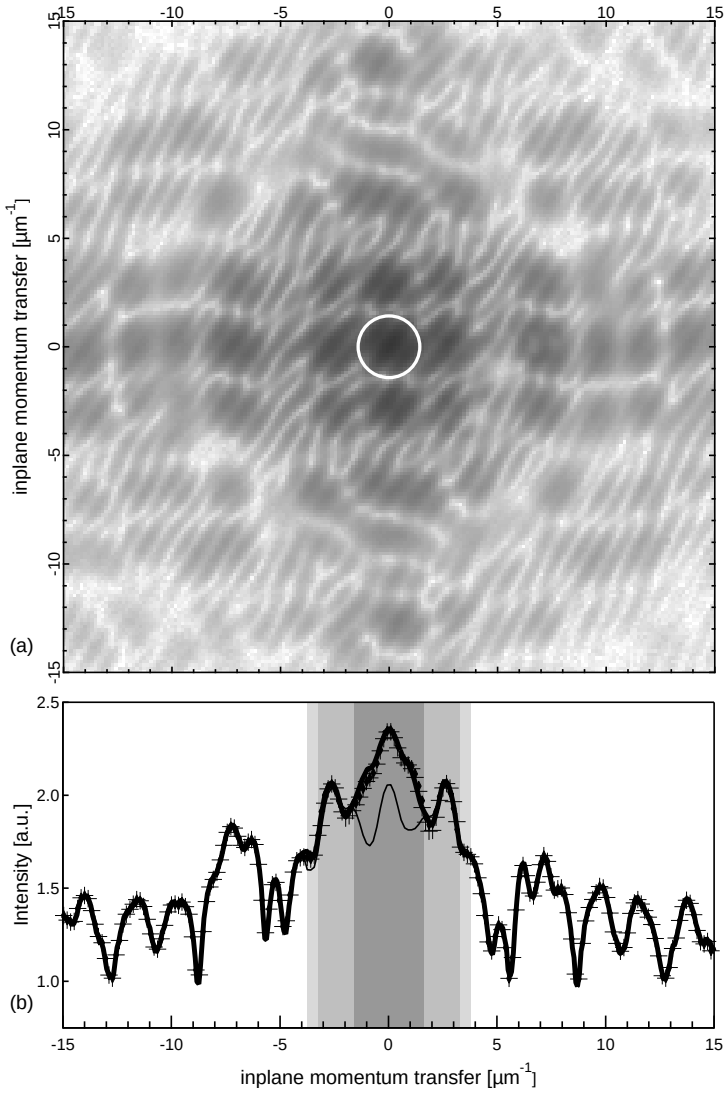

Figure 3.12: *(a) Logarithmic plot of the recovered Fourier scattering magnitude inside a blocked area of radius $q = 1.5\mu m^{-1}$ (white circle). The free-floating magnitudes are well calculated by the algorithm in comparison to the measured intensity. (b) Profiles of the scattering intensity around the specular peak in logarithmic scale. The thick line indicates the originally measured intensity. Profiles of the recovered Fourier magnitudes by reconstruction as shown in Fig. 3.11(a) and (b) are plotted with cross symbols. Only if Fourier components larger than $q = 3.1\mu m^{-1}$ are blocked (Fig. 3.11(c)) the scattering intensity cannot be re-calculated in the free-floating area (thin line).*

As described above the Fourier magnitudes inside the padded area are re-calculated by the algorithm. Fig. 3.12(a) shows the reconstructed scattering intensity initially blocked inside the white circle. The recovered magnitudes of the different blocking sizes are shown in Fig. 3.12(b) together with the actually measured intensity (thick line). The gray scaled background of the plot marks each radius of the corresponding blocked area. The cross symbols indicate the profiles of the Fourier components obtained by the algorithm for $q = 1.5\ \mu m^{-1}$- and $q = 3.1 \mu m^{-1}$-blocking. Only for larger blocking the scattering intensity is not recovered (thin line).

By applying a beamblock the intensity of the incident radiation can be increased. If the beamblock is chosen such that it is still small enough to allow for reconstruction, *e.g.* the complete central peak and part of the minor maxima is blocked (up to $q = \pm 3\ \mu m^{-1}$), then more than half of an order of magnitude in intensity can be gained until the detector is saturated by the diffuse scattering intensity

In summary, reconstruction of a non-complex object from the coherent soft x-ray scattering pattern has been demonstrated. In addition, a method based on a reference hole in the object plane has been proposed and tested. The method allows the determination of the support from the x-ray diffraction pattern. In the next chapter, the same principles are applied to more complicated specimen: magnetic domain patterns which are continuous and complex-valued objects.

Chapter 4

Reconstruction of magnetic domain structures

After the successful reconstruction of a real-valued diffracting object in chapter § 3, we focus on the problem of phase retrieval from a magnetic structure. This is a challenging task because magnetic scattering is relatively weak. Hence, it must be well separated from any other scattering or diffraction signal. Further, the reconstruction of complex-valued objects has more possible solutions (*uniqueness* problem) than from real objects [60, 63, 68]. This is why we have to carefully check the obtained results.

4.1 Experimental proof of principle

4.1.1 The test sample

The reconstruction of *magnetic* domain structure is a new challenge and so far has never been demonstrated. This requires that first a known sample structure is investigated to prove the feasibility of magnetic structure reconstruction itself. A test assembly is created consisting of a mask and a $CoPt$ multiplayer sample. After imaging both the mask and the sample-mask setup by microscopy the reconstruction experiment can be performed and the obtained result can be proven by the initial images.

Known support mask - An important prerequisite for the phase retrieval of the scattering from complex-valued objects is a known support [63, 65, 68]. Therefor, we used a sample setup with a mask containing a large circular aperture of 1.2 μm diameter for the sample (let us call it "sample hole") and a small reference hole of approximately 200 nm diameter as already proposed in § 3.1.2. The reference hole is separated 1.2 μm from the sample pinhole. The pinholes are drilled by FIB technique into a Au-film of 2 μm thickness to guaranty opaqueness [46]. This mask is placed in direct contact on a magnetic sample which can be investigated in a scattering experiment in transmission geometry. The use of the autocorrelation of the object obtained from the measured intensity allows to locate the support in the object matrix. From the known dimensions of the mask (sample hole plus reference hole) we can determine a *tight* support as it is necessary for complex-valued objects [63, 68].

Known sample structure - As sample the $CoPt$ multilayer of 50 double layers of 3 nm Co and 0.7 nm Pt sputtered on a SiN_x membrane is used. The $CoPt$ sample is prepared by O. Hellwig [44]. In order to be able to test the phase retrieval process, the sample.mask assembly has been imaged by a transmission X-ray microscope (TXM) at the Advanced Light Source (ALS) in Berkeley by P. Fischer [21]. The resulting image is presented in Fig. 4.1. The mask with the sample hole and the reference hole is clearly visible. The magnetic structure of the $CoPt$ multiplayer is recognizable within the sample hole: alternating domains arranged in stripes. Unfortunately, the reference hole shows a faint side-structure that may be the result of a misplaced focus of the ion beam. The structure is not completely drilled through the Au-film but attenuated radiation penetrates that thinned area.

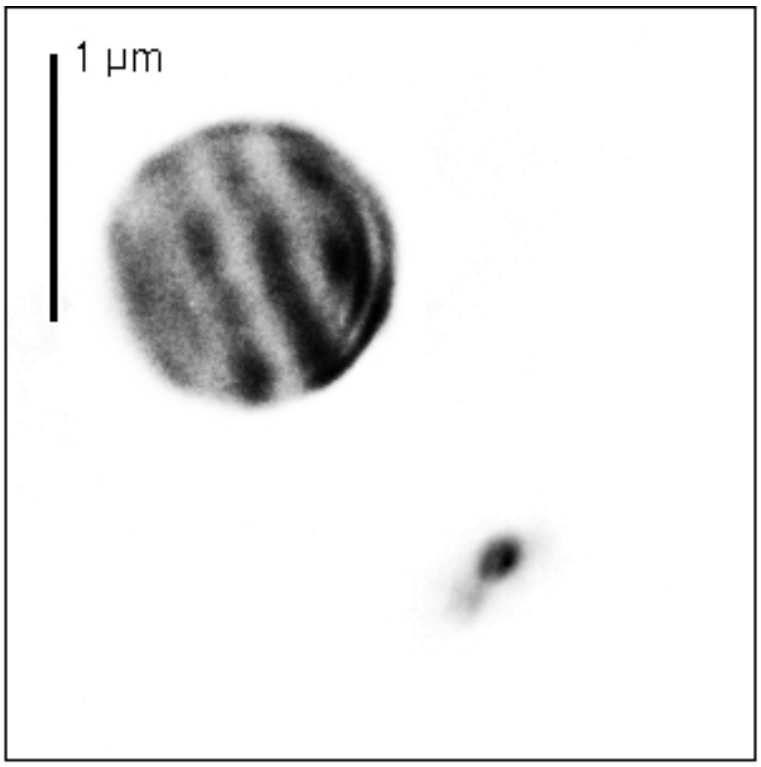

Figure 4.1: *TXM image of the CoPt membrane-mask assembly recorded at the Co L_3 absorption edge. The magnetic domains are oriented mainly parallel revealing a stripe pattern. The domain pattern and the pinholes sampled in the scattering experiment are imaged at the ALS by P. Fischer [21] to allow for comparison with the result from reconstruction.*

The magnetic multilayer is measured in transmission geometry, *i.e.* due to the perpendicular anisotropy of the sample the results from § 2.5.1 are valid. The intensity of the speckle pattern is recorded with a high-resolution (2048 × 2048)-elements CCD camera of quadratic 13.5 μm-pixel. The CCD chip is exposed directly to the soft X-ray photons with an quantum efficiency of 80% at 780 eV. For further details see § C. The camera is located 315 mm downstream of the sample, thus, the maximumF in-plane momentum transfer covered by the active area is $q_{max} = 170\ \mu m^{-1}$ allowing for a resolution of approximately $r = 40\ nm$ structures. The oversampling is large, $\Omega_{(2D)} = 1200$.

Again, the experiment is performed at the UE56/1-SGM beamline at BESSY with almost the same setup as depicted in Fig. 3.4. The $CoPt$ multilayer-mask assembly is illuminated with 778 eV photons of circular polarization to enhance the magnetic contrast due to resonant scattering (see § 2.5.2). An additional guard pinhole of 500 μm in diameter is inserted 25 mm upstream of the sample to block high order diffraction rings from the 20 μm pinhole located 723 mm upstream. Hence, only the AIRY disc and the FRAUNHOFER rings up to $4th$ order of the diffraction pattern passes to the sample. The transverse coherence length at the sample yields $\xi_{tr} = 9.2\ \mu m$. The energy resolution is $\Delta E = 0.4\ eV$ (entrance slit: 30 μm, exit slit: 50 μm) and the longitudinal coherence length is $\xi_l = 2\ \mu m$.

4.1.2 The autocorrelation obtained from intensity pattern

The measured scattering intensity obtained is shown in Fig. 4.2(a). The cumulated exposure time of the camera is 1400 s and the read-out-noise has been subtracted. Clearly observable are two satellite maxima horizontally arranged to the left and right of the central ($q = 0$)-maximum. They reveal the stripe like domain structure of the magnetic sample and their corresponding momentum transfer of $q \approx 24\ \mu m$ represents the average period of 260 nm of the magnetic domains. The diffraction rings of the sample hole are visible up to many FRAUNHOFER orders. The interference of the sample and reference hole can be recognized by a stripe pattern across the whole intensity image. The maximum in-plane momentum transfer of recognizable interference structures is $q_{max} \approx 120\ \mu m^{-1}$. Hence, the smallest spatially resolvable structure is $r \approx 52\ nm$.

By inverse Fourier transform of the intensity the autocorrelation (or PATTERSON image) is calculated and plotted in Fig. 4.2(b). The area of the sample pinhole probed by the reference hole is clearly visible. The autocorrelation shows the characteristic twin-images, each being mutually the mirror image of the other. The reference hole is located in the center of the image inside the saturated black convolution area. A clear domain structure appears in the autocorrelation function due to the reference pinhole being small compared to the area of the sample pinhole but approximately as large as the width of typical domains. The sample hole structure shows a halo that is correspondingly mirrored in both twin-images. This shadow is caused by the thinned structure of the reference hole as described above. As some radiation penetrates this structure it acts as an additional reference aperture that also probes the domain structure. For further considerations of the autocorrelation the shadow image is ignored. The number of black and white domains is the same as in the TXM image (cp. Fig 4.1). Also, the orientation of the domains is the same as in the reference image, *e.g.* the first white domain from the right is in line with the reference hole. As a result, one can state that the autocorrelation reveals already all features of the test object and can be considered as a simple reconstruction of good quality.

Determination of initial input to the algorithm - Consequently, this offers a good possibility to start the algorithm with the knowledge obtained from the autocorrelation. The idea is to use the PATTERSON map[1] as a first (good) guess of the object that has to be reconstructed. The initial input helps the algorithm to converge better towards the correct solution than with no further knowledge about the object [65]. It shall be emphasized that the *a priori* knowledge is obtained without exception from the measurement.

[1] Autocorrelation obtained from intensity measurement.

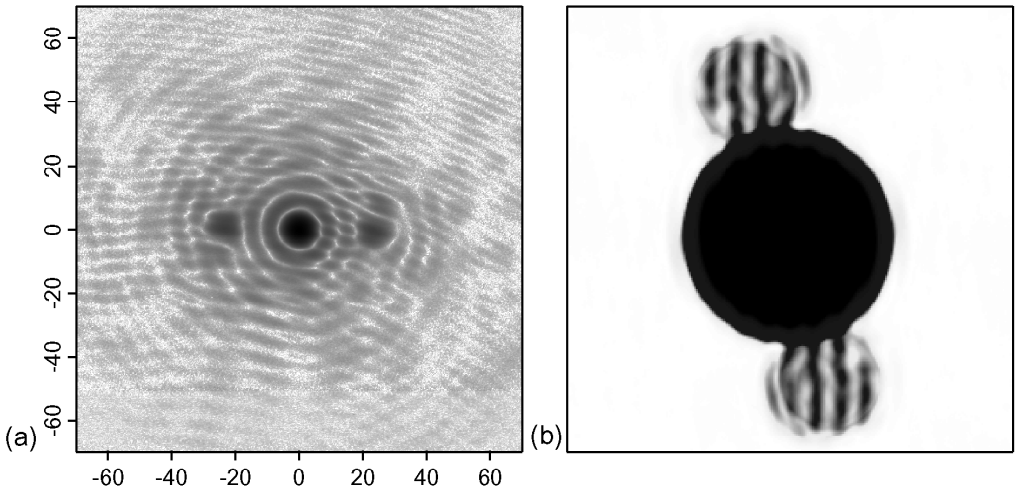

Figure 4.2: *(a) The scattering intensity from the test sample shown in Fig. 4.1. The exposure time is* 1400 *s and read-out-noise is subtracted. The image is plotted in logarithmic scale and in units of* μm^{-1}. *(b) Autocorrelation (or* PATTERSON *map) of the test sample obtained by inverse Fourier transform of the intensity. The structure of the magnetic domains is already visible due to the relatively small reference pinhole.*

Applying the tight support to the autocorrelation function cuts out the sample and the reference pinhole area. This new object is used as magnitude $|a_r(\mathbf{r})|$ of a complex wave with zero phase,

$$a_r(\mathbf{r}) = |a_r(\mathbf{r})|\, e^{i\phi_r(\mathbf{r})} = \begin{cases} |g'_{AC}(\mathbf{r})| & \mathbf{r} \in S_r(\mathbf{r}) \\ 0 & \mathbf{r} \notin S_r(\mathbf{r}) \end{cases} , \tag{4.1}$$

where g_{AC} is the autocorrelation function of the object and S_r is the support. Of course, according to the existence of twin images in the autocorrelation of the object, it is ambiguous which sample area should be chosen. It is possible to choose a support that selects both images and then let the algorithm converge with equal probability to either one or the other of the twin solutions [65,66,68]. Nevertheless, only one of the images is chosen *a priori* to avoid twin-image stagnation [66]. Hence, it is always possible that the obtained solution is the mirror image of the real space object. A forward Fourier transform of $a_r(\mathbf{r})e^{i\phi_r(\mathbf{r})}$ yields a Fourier-space magnitude $A_f(\mathbf{q})$ and phase $\phi_f(\mathbf{q})$. Before starting the error reduction (ER) algorithm in Fourier-space (see Fig. 3.1(a)) the magnitude is substituted by the square root of the measured intensity. The phase is maintained as it is a good initial guess obtained from the PATTERSON image[2]. The initial phase is plotted in Fig. 4.3(a).

4.1.3 Reconstruction procedure: Proof of principle

500 cycles of the ER algorithm are performed with just applying the support in each cycle to the object magnitude and phase but no further internal constraints. In Fourier-space the magnitude is replaced by the square root of the measurement for each cycle. The resulting object is shown in Fig. 4.3(b). The reconstruction shows the same features as the autocorrelation in Fig. 4.2(b): In the center of the image three white domains are observable where the right domain shows a little kink. The domains are oriented the same way and the right domain is aligned with the reference hole. The edges of the domains are sharper for the reconstruction than in the autocorrelation. A scan line through the magnetic domain pattern is plotted in the inset graph of image (b). High values correspond to black color in the image and low values to white, so the three white domains are three minima in the profile.

[2]citing FIENUP: "*Starting with a good initial input [...] helps*" [65].

One pixel of the image corresponds to approximately 20 nm and the smallest resolvable structure of the object is $r = 52$ nm (see § 4.1.2). As a result, the obtained reconstruction image shows more details than it is expected from the actual spatial resolution, namely, the smallest resolvable element is represented by three pixels. *I.e.* that the fuzzy domain boundaries are artifacts obtained from the algorithm procedure. Comparing the reconstruction to the microscope image in Fig. 4.1 one can state that the object is recovered from the pure measurement of its scattering intensity.

As a conclusion, the reconstruction procedure is applicable to magnetic structures. Exploiting the magnetic dichroism contrast allows for small angle scattering from the magnetic domains. The PATTERSON image of the scattering object reveals already most of the magnetic structure. The result can be improved in spatial resolution by the reconstruction procedure.

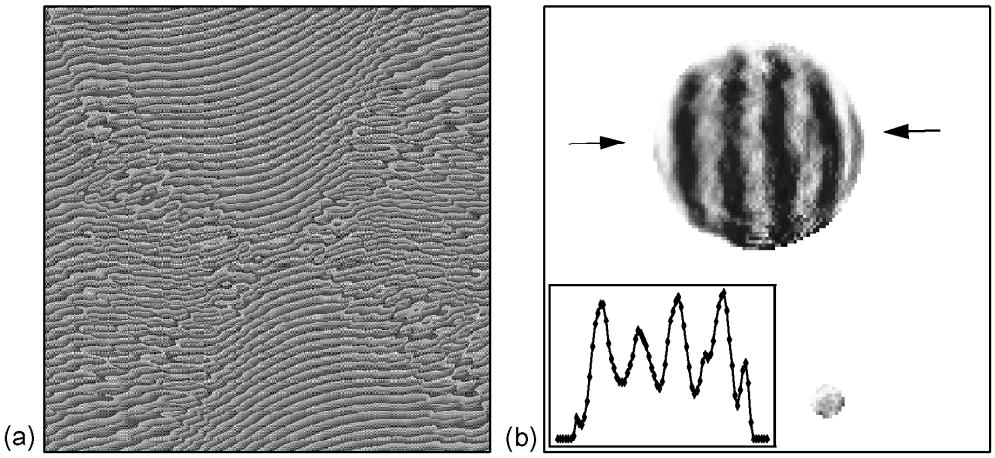

Figure 4.3: *(a) Initial phase guess obtained from forward Fourier transform of the autocorrelation. (b) Magnitude of the resulting real space object. The number of domains, their widths and the orientation coincide with the microscope image of the same sample. The inset shows a profile through the magnetic domains between the arrows.*

4.2 Result - First reconstruction of *un*known magnetic structures

After successfully reconstructing the test object with a known arrangement of magnetic domains the phase retrieval technique is applied to unknown objects. A $CoPt$ multilayer is investigated, that is grown with the same parameters as the test sample. The sample is exposed to external magnetic fields and imaged in different magnetic states. The mask used is: 1.2 μm sample pinhole, 170 nm reference pinhole and a center-to-center distance of 1.2 μm. The beamline is tuned to the scattering maximum at 778 eV with the photons being right circular polarized.

First, the sample is investigated after it was exposed to an external magnetic field with field-direction parallel to the sample surface. After removal of the field the domains are aligned in stripes [43]. Hence, the sample has a similar structure as the test sample in the former section. This is confirmed by the speckle pattern obtained from coherent scattering in transmission geometry: The intensity pattern shown in Fig. 4.4(a) clearly shows two centro-symmetrically arranged magnetic satellites around $q = \pm 25$ μm. They correspond to the period of the magnetic domains of approximately 250 m and are aligned on a axis through the specular peak ($q = 0$). This alignment indicates a stripe-like pattern of the magnetic

domains. Additionally, the FRAUNHOFER-rings from the 1.2 μm circular sample pinhole can be observed and the high-frequency modulation of the ring intensity is due to pinhole-reference hole interference.

The stripe-like domain structure is also confirmed by the autocorrelation, Fig. 4.4(b). Of course, the autocorrelation shows a twin image centro-symmetrically located around the center. But to show more details the image is zoomed to one of the twin-images. As the reference hole is smaller than the period of the domains the autocorrelation reveals the overall domain structure. Four black and three white domains are clearly observable. The distance of the reference hole from the sample hole is as large as the summed diameter of the two pinholes. Hence, the PATTERSON image shows an overlap of the sample area with the central convolution area that disturbs the lowest black domain and part of the neighbored white domain.

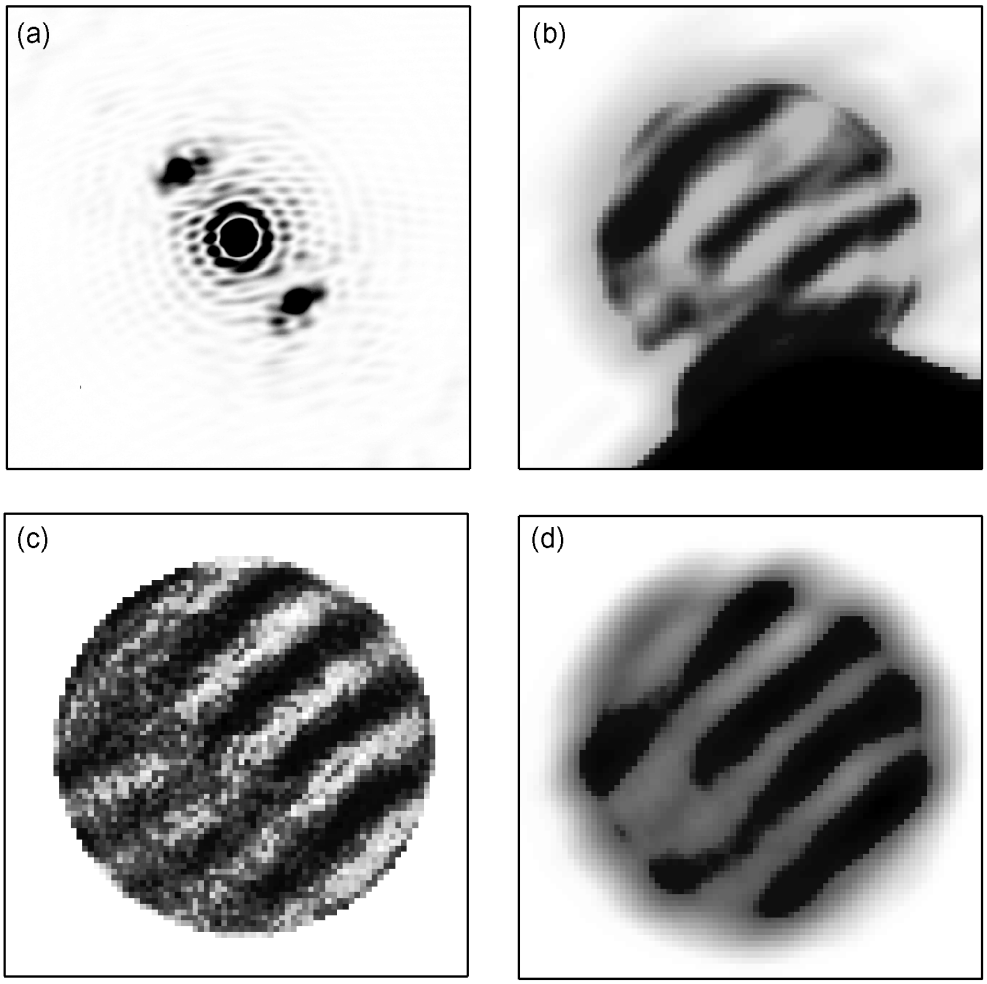

Figure 4.4: *Reconstruction of complex-valued magnetic domain sample. (a) Scattering intensity of the CoPt multilayer sample. The dimensions of the image axes are given in in-plane momentum transfer from* $-70\mu m^{-1}$ *to* $70\mu m^{-1}$ *in both directions. (b) The corresponding autocorrelation as obtained from the measured intensity. The magnetic domain pattern is visible. Only one of the twin-images is shown. (c) shows the resulting object after performing the iterative ER algorithm. The parallel structure of the domain is clearly observable. (d) The result from (c) is convolved with a disk of the size of the reference pinhole to check the consistency of the result with the image in the autocorrelation function.*

As described in the former section the autocorrelation obtained from the measured scattering intensity is considered as a good first guess of the magnetic structure. This knowledge about the sample is used as input for the reconstruction algorithm. From Fourier transform the Fourier phase is obtained and taken as starting phase. The same algorithm procedure including the same constraints as above are engaged for the following reconstruction. The result of the phase retrieval algorithm is shown in Fig. 4.4(c). The stripe domains are clearly visible. In the lower left part of the circular area the stripes are fringed and have less sharp edges than in the right part. The resolvable sample structure is about $r = 52\ nm$. Each pixel of the reconstruction image covers a square of 20 nm lateral size. This is 2.5 times smaller than the possible resolution. This might cause artifacts by the reconstruction procedure like the fuzzy domain boundaries. The four black domains that are already visible in the PATTERSON map are sharply recovered by the algorithm. The overlap region shown in the PATTERSON image has been removed and an additional white domain appears in the reconstructed magnetic structure.

Applying an external magnetic field perpendicular to the $CoPt$ multilayer surface by saturating the domain magnetization and removing the field causes the domains to decay into a labyrinth structure (*e.g.* cp. Fig. 2.4(c)) [14, 43]. This change in magnetic domain arrangement is also observed by the following coherent scattering experiment. A permanent magnet of approximately 1 T is manually approached close to the $CoPt$ sample membrane such that the stray field saturates the magnetization in direction of the surface normal. The saturation field of the $CoPt$ domains is $> 1.1\ T$ [14]. After removal of the $NdFeB$-magnet the magnetization returns to its remanent state while rearranging the domain pattern. This is confirmed by the scattering intensity taken from the domain pattern and plotted in Fig. 4.5(a). In contrast to the two aligned satellites in Fig. 4.4(a) the magnetic intensity is distributed more homogeneously in the circular area. This indicates that any orientation of the domains can be found in the sample structure like it is the case for labyrinthine arrangements. Again, the FRAUNHOFER diffraction rings of the sample hole are visible and the interference fringes of the reference and the sample hole can be observed.

The average width of domains arranged in stripes is smaller than the one for randomly arranged domains [43]. This has also been measured in the presented scattering experiments. In Fig. 4.6 a radial profile of the speckle pattern is plotted for the stripe-like arrangement (solid line) and the worm-like arrangement (dotted line). The scattering maximum of the domains is visible revealing a certain width that indicates a distribution of domain periods and widths. For the parallel aligned domains the magnetic scattering peak is slightly moved towards higher momentum transfer, *i.e.* smaller real space structure, compared to the profile of the worm-domain scattering.

The autocorrelation obtained from the intensity measurement shows the new domain pattern (Fig. 4.5(b)). The domains are clearly arranged in different directions. The width of the domains is approximately 150 nm. The PATTERSON image is used for reconstruction of this object by calculating the initial Fourier phase as described in the former section. The reconstructed result is plotted in Fig. 4.5(c). In the center of the image the domain structure reveals bent shapes and only a few parallel structures at the boundary of the image are left. One can find slight similarity to the autocorrelation. The fringed edges of the domains in the center cannot be expected to reflect the real structure. The reason is that rough domain wall surfaces increase the static energy. Therefore, rough interfaces are less stable than smooth boundaries. Again, the fuzzy boundaries may be artifacts caused by the algorithm that reconstructs each pixel with a spatial dimension of 20 nm whereas actually the smallest resolvable structure is approximately $r = 52\ nm$. *I.e.* an uncertainty of approximately 3×3 pixel remains in the reconstructed object.

Finally, a 1.6 T field is applied perpendicular to the sample surface because the magnetization might not be saturated with the former 1 T permanent magnet. After returning into remanent state the domains are measured again, Fig. 4.7(a). This time the magnetic domains are disordered. From the intensity measurement the autocorrelation of the domains structure is calculated and shown in Fig. 4.7(b). The arrangement of the domains is different to that of the former magnetization process (cp. Fig. 4.5(b)). The reconstruction is plotted in Fig. 4.7(c).

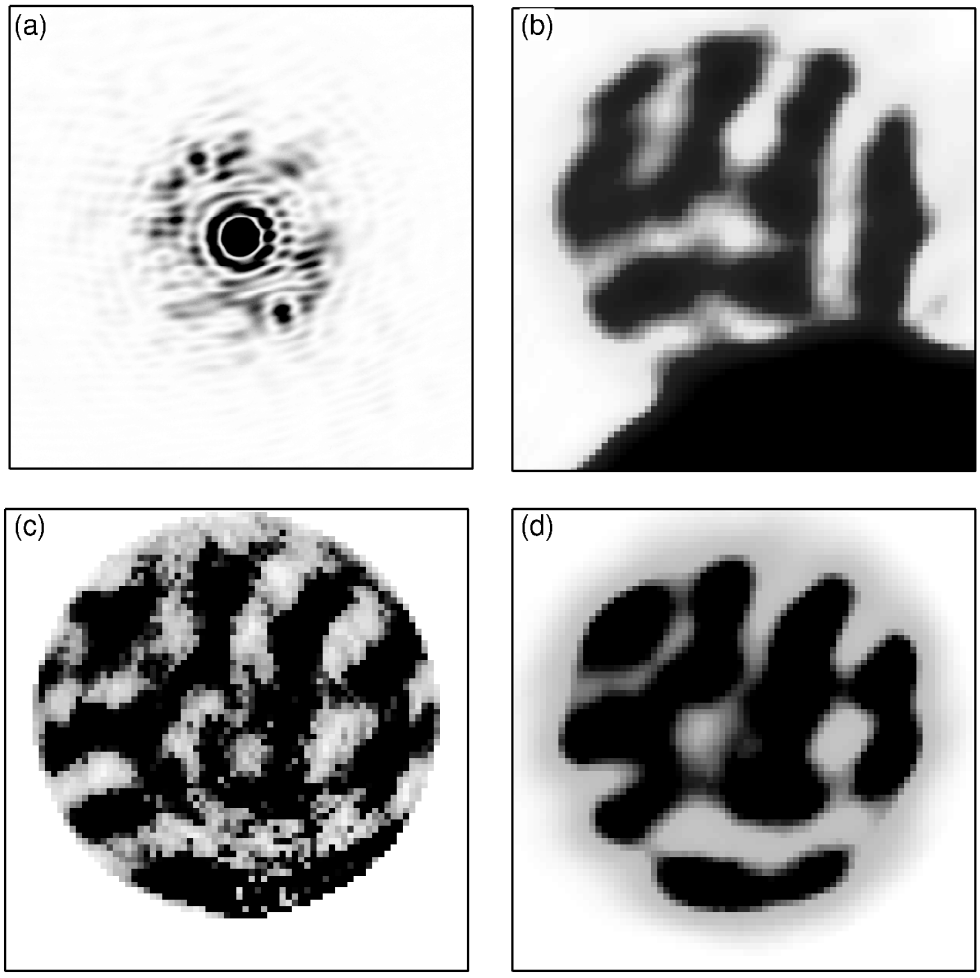

Figure 4.5: *(a) Scattering intensity after temporarily exposing the sample to a* 1 T *magnetic field perpendicularly applied to its surface. Units: in-plane momentum transfer from* $-70\mu m^{-1}$ *to* $70\mu m^{-1}$ *in both axes. (b) The corresponding autocorrelation as obtained from the intensity. The magnetic domain pattern is visible. (c) The reconstructed object after* 500 *cycles of the ER algorithm. (d) The convolution of the result with the disk corresponding to the size of the reference hole.*

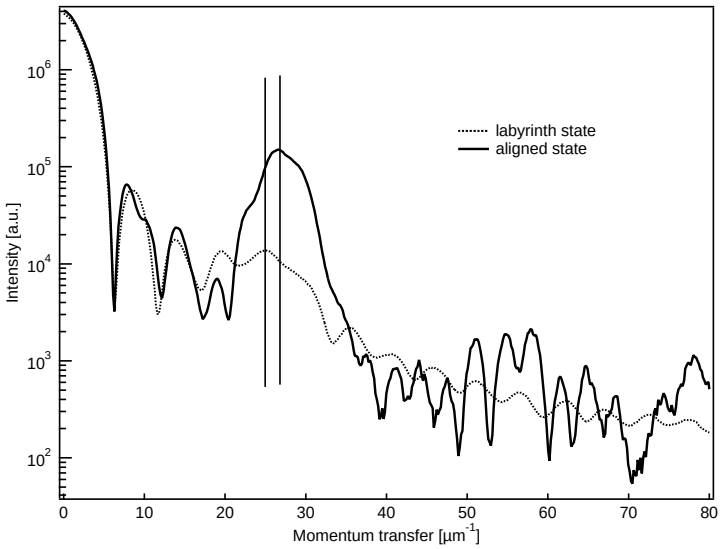

Figure 4.6: *Small angle scattering from aligned (solid line) and labyrinthine (dotted line) CoPt domain patterns. The scattering is obtained from the measured two-dimensional scattering patterns: Aligned domain state (solid) by profile cut through image shown in Fig. 4.4(a); Labyrinth state (dotted) by angular integration of the pattern shown in Fig. 4.5(a). For the stripe domain sample* 3 *orders of the magnetic scattering are observable. The peaks is slightly shifted towards higher q than for the worm-like state indicating the smaller domain width.*

Conclusion - the scattering experiments and results of reconstruction confirm all the behaviour of the *CoPt* multilayer domains: The application of a saturating field perpendicular to the sample surface causes the domains to decay into a labyrinth structure. The domain period is different for stripe and worm domains as it has been seen in the scattering pattern.

4.2.1 Discussion and uniqueness problem of the solution

In general, the reconstruction of complex-valued objects has multiple solutions (uniqueness problem) [60, 68]. One feature to reduce the number of possible solutions is the knowledge of a *tight* support as it was used in the reconstructions presented. It has been shown that a tight support can force the algorithm to the correct solution [68]. Upon the presentation of the images of the magnetic structures obtained by the phase retrieval algorithm one must ask whether the solutions are unique and reliable. Thus, a reliability criterion is proposed in this section and discussed.

The size of the reference hole is smaller than the average width of two oppositely magnetized domains. Consequently, the autocorrelation reveals the main shapes of the real space structure. The autocorrelation can be considered as the convolution of the magnetic domain structure with the reference hole. If the result of the phase retrieval algorithm is convolved with a structure that corresponds to the reference hole then it should be similar to the autocorrelation. This idea is realized in plot (d) of each figure, Fig. 4.4 to Fig. 4.7 where the reconstruction is convolved with a disk that corresponds to the size of the reference hole.

The convolved result in Fig. 4.4(d) and the autocorrelation in (b) show good congruence. The reliability is given for this object. The number of stripes and their orientation are consistent in (b) and (d). The object is reconstructed although there may be doubts about the fine structure. To present a numerical estimate of the congruence, the pattern correlation of the convolved reconstruction image

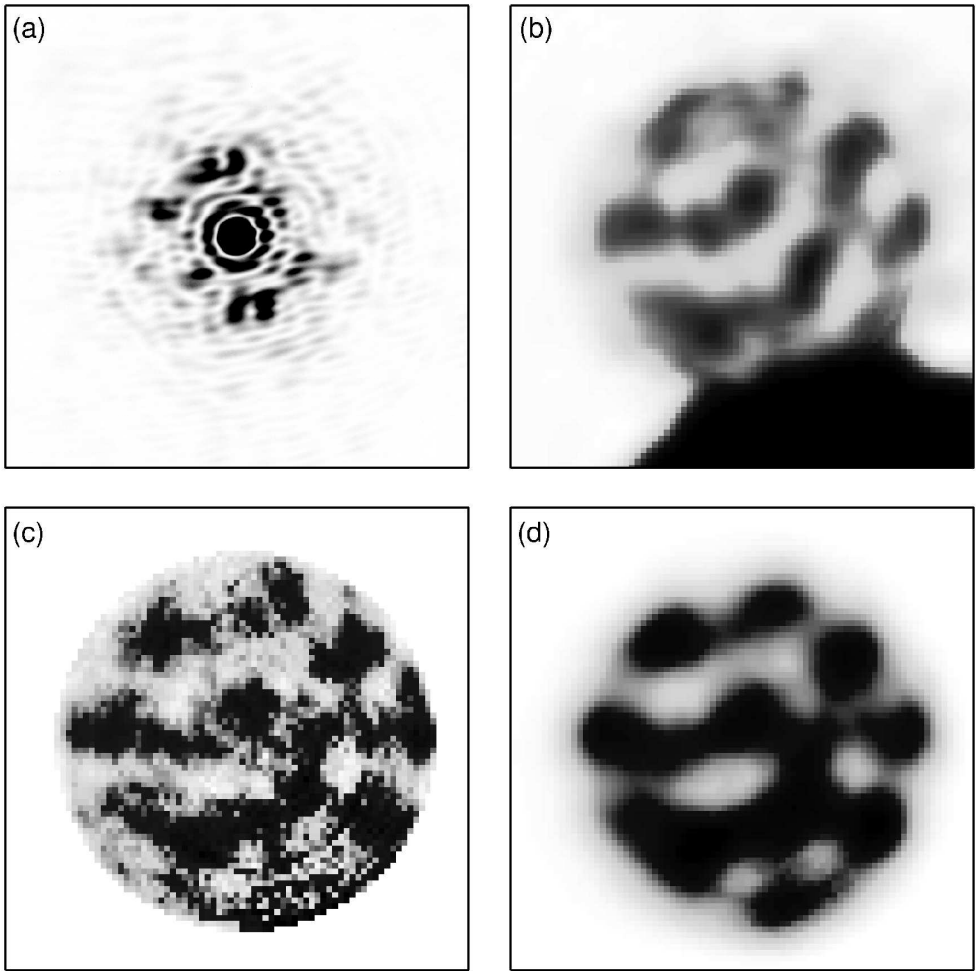

Figure 4.7: *(a) Scattering intensity after temporarily exposing the domains to a* 1.6 T *magnetic field. This time the scattering pattern is relatively spreaded. Units: in-plane momentum transfer from* $-70\mu m^{-1}$ *to* $70\mu m^{-1}$ *in both axes. (b) The corresponding autocorrelation as obtained from the intensity. The magnetic domain pattern is visible. (c) The resulting object after* 500 *cycles of the ER algorithm. (d) The convolution of the reconstructed object.*

and the PATTERSON map is calculated according to:

$$\gamma_I = \frac{\sum_{h,k}(M_{hk} - \bar{M}_{hk})(N_{hk} - \bar{N}_{hk})}{\left[\sum_{h,k}(M_{hk} - \bar{M}_{hk})^2 \cdot \sum_{h,k}(N_{hk} - \bar{N}_{hk})^2\right]^{1/2}},$$

where M_{hk} and N_{hk} are the corresponding pattern matrices. The correlation of the Fourier transform image and the phase retrieval pattern is $\gamma_I = 0.95$, confirming the congruence.

The next domain structure shown in Fig. 4.5 is more complex than the first one. The convolution of the result with the reference structure (Fig. 4.5(d)) corresponds to the autocorrelation obtained from the scattering intensity. The correlation value is $\gamma_I = 0.90$. Most part of the convolved domain pattern show the same features as the PATTERSON map. However, some deviations can be observed. For example, the autocorrelation (b) shows a U-shaped black domain in the upper left region whereas the convolved reconstruction just shows the lower and right branch of that U-form.

For the last reconstruction the convolution Fig. 4.7(d) shows some similarity with the autocorrelation but cannot clearly be declared as coinciding. For example, the autocorrelation shows a closed white domain coming from the center of the left side and being bent to the upper edge of the image. The result as well as the convolution (d) contain the horizontal part of that domain but it ends in the center of the circle. Nevertheless, the numerical correlation is $\gamma_I = 0.93$. The high value indicates a good agreement between both patterns. That can be ascribed to the same correlation width of the domains in both resulting images, *i.e.* the patterns are similar on a certain lengths scale that corresponds to the domain width.

Finally, on one hand the results given here show successful reconstruction for simple structures and the obtained object is reliable. On the other hand artificial structures are induced by the reconstruction algorithm. Whether the correct solution has been obtained can be tested by comparison of the autocorrelation pattern and the reference-hole convolved reconstruction pattern. A numerical correlation value could be calculated for the solution. This value could also be used as a criterion to test a series of solutions. If the reconstruction procedure is varied by *e.g.* different values of β (the HIO parameter, see eqn. 3.5) or used with different supports during runtime, the result may be different each time. Whether one of the obtained possible solutions is the correct one can then be tested by a maximum of the correlation value.

For all experiments the autocorrelation obtained from the measured scattering intensity by inverse Fourier transform is very reliable revealing already the main structures. The resolution of the PATTERSON image is only limited by the size of the reference hole.

For further experiments the microstructuring techniques may be engaged to create non centro-symmetric supports, *e.g.* a non-equilateral triangular or a circle with lateral bulges. Centro-symmetric supports may cause stagnation of the reconstruction algorithm and, hence, prevent from obtaining the correct result. The reason for stagnation is that for centro-symmetric shapes the actual image $a_r(\mathbf{r})$ and the translated twin-image $a_r(\mathbf{r} - \mathbf{r}_0)$ are equally probable. This may cause the reconstructed result to be a mixure of both [68].

In a way, the results of this magnetic reconstructions are preliminary. The size of the reference hole used in these experiments allows for considering the autocorrelations of the objects to be reliable. They show a blurred image of the actual objects. Further reconstruction procedures generally increase the resolution of the images but at the cost of less reliability of the obtained object. More effort has to be done in decreasing the size of the reference hole to come closer to the limit of holography where the phase information is encoded in a fringe pattern of the scattering intensity [68]. Then the object is easily obtained from one inverse Fourier transform.

Chapter 5

Summary

The main subject of this work is the reconstruction of the real-space structure of ferromagnetic domain patterns from their coherent magnetic scattering intensity. Exploiting the X-Ray magnetic circular dichroism (XMCD) effect, a contrast between oppositely magnetized domains of $CoPt$ multilayers is induced to obtain small angle scattering (SAS) from the spatial domain distribution. The $CoPt$ multilayer system reveals an magnetic anisotropy that is perpendicular to the film surface and, hence, allows for strong dichroism effects in transmission geometry, *i.e.* with perpendicular incidence of the radiation. Using coherent Soft X-rays permits to record a Speckle intensity pattern that contains all information about the individual domain structure beyond statistical information that is already obtained from incoherent small angle scattering. An algorithmic reconstruction procedures allows for calculating the spatial domains structure from the scattering intensity pattern by solving the known phase lost problem. The reliability of the procedure is tested by retrieval of an aperture pattern that is drilled into an opaque Au-film. After the successful test the procedure is extended to the magnetic domain pattern. First reconstruction results of ferromagnetic domains are obtained and it is shown that the domain arrangement changes by temporary and consecutive exposures to an external magnetic field.

In the first part of the thesis the pre-requisites for successful reconstruction of magnetic domain patterns are introduced: *coherence* and *resonant magnetic scattering*. Coherence has to be produced befor starting the experiments. The method of spatial and spectral filtering is demonstrated and quantitatively shown. Statistical properties of Speckle patterns - the granular structure of scattering intensity patterns from coherently illuminated objects - have been introduced and illustrated by own experimental results.

The basic dependencies of the resonant magnetic scattering amplitude are investigated concerning variation of polarization and energy. The interaction of pinhole diffraction and magnetic domain scattering depends strongly on the state of polarization of the incident light. Circular polarized X-Rays cause strong interference effects between both the diffraction from the large sample shapes (the pinhole) and the small angle scattering from magnetic domains. The individual scattering pattern is different for right (RCP) and left circular polarized (LCP) light and the sum of both yields the same pattern as it can be recorded if linear polarized light is used. Furthermore, the strong interference effects vanishes for linear polarization and, likewise, for the sum of the scattering patterns using RCP and LCP light.

The magnetic scattering patterns that are obtained by consecutively adjusting the wavelength of the incident soft X-ray photons across the Co L_3 absorption edge remain unchanged. To get a quantitative measure of a potential change in the Speckle pattern, a pattern correlation value is calculated as function of energy. Pure magnetic scattering reveals constant values upon energy variation across the L_3 resonance. Only interference between the pure magnetic scattering and the pinhole diffraction cause a change of the pattern.

The second part of the work is dedicated to the reconstruction of real-space structures from their diffraction or scattering pattern. This technique emerges as lensless imaging that allows to image nanostructures with the use of a simple experimental setup. The term "lensless" expresses the fact that

no imaging lenses are used in contrast to microscopes. The reconstruction of diffracting objects like a pattern of apertures in an opaque film is successful. The use of a reference hole that is drilled into the same plane as the rest of the pattern turns out to be very helpful in the phase retrieval procedure. The diffraction from the reference hole interferes with the diffraction of the aperture pattern. Hence, the first inversion of the diffraction pattern by Fourier transform reveals already the rough shape of the structures that have to be reconstructed. This "knowlegde" about the real-space structure is used to drive the algorithm and supports it to converge towards the correct solution.

The use of the reference hole is established as a general approach also for reconstructing the magnetic domain pattern. First, a test sample of parallel aligned domains is used to check the algorithm. As the test domains are imaged by a transmission X-ray microscope it is possible to compare the result from the phase retrieval procedure with the actual structure. The same reconstruction algorithm is then applied to unknown magnetic structures. The first scattering pattern of the sample reveals a parallel alignment of the domains because of special arrangement of the scattering maxima. Due to the existance of the reference hole the first Fourier transform inversion shows already the correct number and orientation of the domains. This low resolution PATTERSON image is included into the algorithm to force convergence. After several hundred iteration cycles the result is obtained. It shows a higher resolution than the former PATTERSON map but unfortunately some artifacts that are caused by the algorithmic procedure.

The same sample is temporarly exposed to a saturating external magnetic field. After being in remanent state the scattering reveals a new domain arrangement as it is expected from literature. The PATTERSON image confirms this impressively. The following reconstruction procedure enhances the spatial resolution but also induces artifacts that may limit its reliability.

Consequently, the reconstruction of magnetic objects from their coherent scattering pattern is shown to be possible. Further effort has to be put on enhancing the quality of the resulting images. A promising approach is the use of a reference hole. With shrinking diameter of the hole this method can be recognized as Fourier transform holography. Recent results from our workgroup demonstrate the successful holography of magnetic domains with structure sizes in the nanometer range but the results are not subject of this work. The use of coherent scattering patterns to extract the real-space structure could find application in microscopy by enhancing the spatial resolution of microcopes. To achieve this a scattering pattern of the object is recorded with high scattering angles. To force convergence, a microscopy image is used as input to the algorithm that calculates the highly resolved real-space structure from the Speckle pattern.

Appendix A

Intensity Function of a Double Pinhole

A.1 Fraunhofer diffraction from a single pinhole

The diffraction pattern from a circular aperture of diameter $d = 2a$ can analytically be described by [18, 20, 49],

$$I(q) = 2\left(\frac{2J_1(qa)}{qa}\right)^2 \tag{A.1}$$

where J_1 is the Bessel function of first kind (see Fig. A.1). This is only valid for the so called Fraunhofer limit where the distance L of the observation plane from the aperture is large compared to the size of the pinhole, namely [20, 49],

$$a^2 \ll \lambda L \tag{A.2}$$

The minima and maxima of the Bessel-function are shown in Tab. A.1,

qa	$\left(\frac{2J_1(qa)}{qa}\right)^2$	
0	1	Max.
1.220π	0	Min.
1.635π	0.0175	Max.
2.233π	0	Min.
2.679π	0.0042	Max.
3.238π	0	Min.
3.699π	0.0016	Max.

Table A.1: Maxima and minima of the Bessel-function of first kind J_1 [20].

The radii of the first Fraunhofer minima follow to be [20],

$$\omega_0 = 0.610\frac{\lambda}{a}, \quad \omega_1 = 1.116\frac{\lambda}{a}, \quad \omega_2 = 1.619\frac{\lambda}{a}. \tag{A.3}$$

The zero-order maximum with radius ω_0 is called Airy-disc.

A.2 Fraunhofer diffraction from a double pinhole

The diffraction pattern of two point sources separated by D is proportional to $I(q) \propto \cos(qD/2)$ (see Fig. A.1). To derive the diffraction pattern of two circular apertures of diameter d and separation D

the two point sources are substituted by the circular apertures. Then the resulting diffraction intensity is a modulation of the sinusoidal intensity distribution by the BESSEL-function eqn. (A.1) [20],

$$I(q) = 2\left(\frac{2J_1(qa)}{qa}\right)^2 (1 + |\mu_{12}|\cos(qD))\,, \tag{A.4}$$

where $|\mu_{12}|$ is the mutual degree of coherence that is unity for perfect coherence. Eqn. (A.4) is plotted in Fig. A.1. The degree of coherence is subject to the next section.

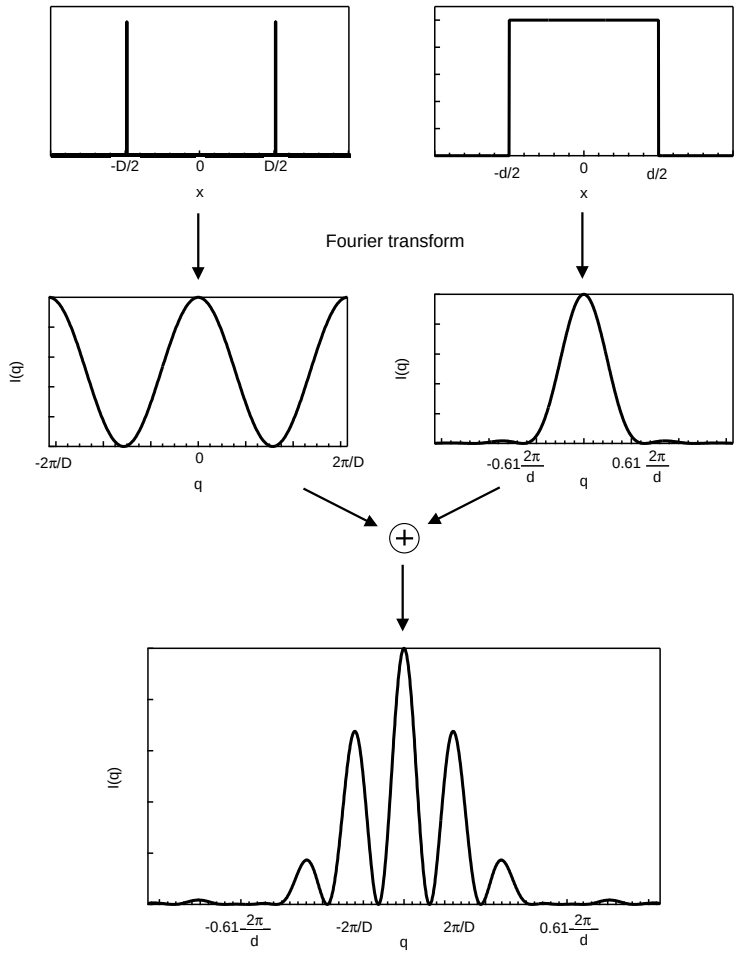

Figure A.1: *Left column: two point sources separated by D and their diffraction pattern. Right column: circular aperture of diameter d and its* FRAUNHOFER *pattern. The sinusoidal diffraction intensity from the two point sources is modulated by the* BESSEL*-function upon substituting the point sources by two circular apertures.*

A.3 Complex degree of coherence

Coherent light sources can also be characterized by transverse correlation of the wave amplitudes in the observation plane. The correlation may be expressed as following [18, 20, 22],

$$\mu_{12} = \frac{\langle E^*(\mathbf{r}_1)E(\mathbf{r}_2)\rangle}{\{\langle|E(\mathbf{r}_1)|^2\rangle\langle|E(\mathbf{r}_2)|^2\rangle\}^{1/2}}, \tag{A.5}$$

where the scalar electric fields are

$$E_1 \simeq \frac{E_\xi e^{ikz} e^{ik\xi^2/2z}}{z} \tag{A.6}$$

and

$$E_2 \simeq \frac{E_\xi e^{ikz} e^{ik\xi^2/2z} e^{i\psi} e^{-ik\xi\theta}}{z}. \tag{A.7}$$

ξ is the coordinate in the source plane and z the distance from the source plane to the detection plane (see Fig. A.2). ψ is the phase difference between two possible paths and θ is the diffraction angle. For large distances z compared to the source size and the detection area the denominator of eqn. (A.5) simplifies to,

$$\sqrt{\langle |E(\mathbf{r}_1)|^2 \rangle} \simeq \sqrt{\langle |E(\mathbf{r}_2)|^2 \rangle} \simeq \frac{|E_\xi|}{z}. \tag{A.8}$$

Hence, the mutual degree of coherence or the mutual correlation function for a single point source can be written as,

$$\mu_{12} = \frac{|E_\xi|^2 e^{i\psi} e^{-ik\xi\theta}}{|E_\xi|^2}. \tag{A.9}$$

Extended light sources can be considered as the incoherent sum of single point sources, simply, by integrating over the area of the source and the degree of coherence for quasi-monochromatic extended light sources becomes,

$$\mu_{12} = \frac{\int\int d\xi d\eta I(\xi,\eta) e^{-ik(\xi\theta_x + \eta\theta_y)}}{\int\int d\xi d\eta I(\xi,\eta)} e^{i\psi}, \tag{A.10}$$

where $I \propto |E|^2$. This is the result of the known VAN CITTERT-ZERNIKE theorem. Hence, the mutual degree of coherence can be considered as the normalized two-dimensional Fourier transform of the source intensity distribution of uncorrelated point sources [18, 20, 22, 49].

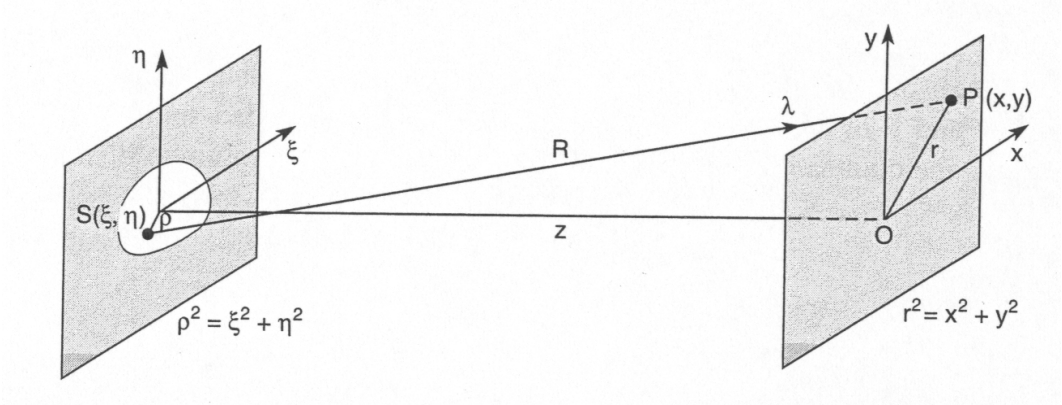

Figure A.2: *Geometry for the calculation of the* VAN CITTERT-ZERNIKE *theorem.* (ξ, η) *are the coordinates in the source plane and* (x, y) *are the coordinates in the detection plane [18].*

Point source: Going back to a single point source eqn. (A.10) reduces to,

$$\mu_{12} = e^{i\psi}. \tag{A.11}$$

Thus, for a point source the degree of coherence is $|\mu_{12}| = 1$, *i.e.* the waves have a perfect phase relation ψ across the observation plane.

Circular aperture: A circular distribution of radius a of incoherent point sources has the following degree of coherence,

$$\mu_{12} = \frac{2J_1(ka\theta)}{ka\theta} e^{i\psi}. \tag{A.12}$$

The circular area of uncorrelated point sources is equivalent to a incoherently illuminated pinhole of the same size [18].

Double pinhole: A nice application for the degree of coherence can be found for two apertures separated laterally by distance D and illuminated by an extended source of radius ρ. Born and Wolf derived the corresponding degree of coherence [20],

$$|\mu_{12}| = \left| \frac{2J_1(\nu)}{\nu} \right|, \tag{A.13}$$

where

$$\nu = k\frac{\rho D}{L}, \tag{A.14}$$

and L is the distance between the two pinholes and the light source. In Fig. A.3 the degree of coherence is plotted as function of the separation D for the two apertures. Hence, the two pinholes can be used as a coherence detector if D can experimentally be varied.

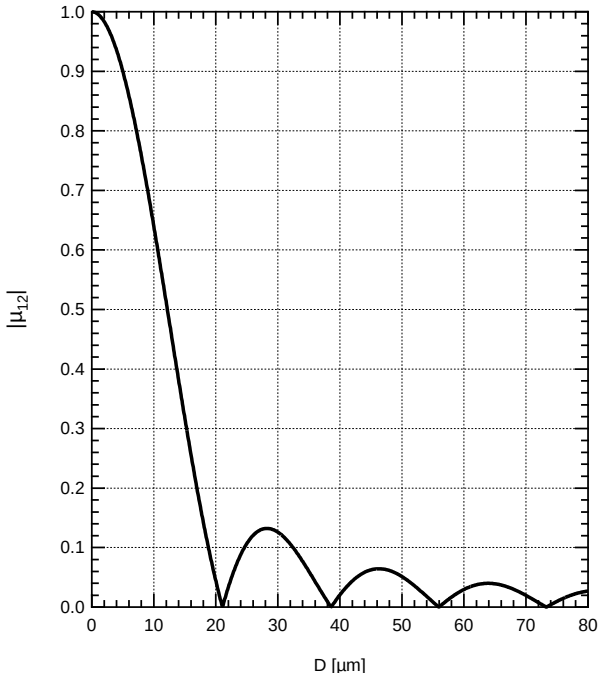

Figure A.3: *Plot of the degree of coherence for an extended light source. $|\mu_1|$ is plotted as function of the separation D of the two scanning apertures.*

In Fig. A.4 the diffraction intensity from two pinholes eqn. (A.4) is plotted for various degrees of coherence. With decreasing transverse coherence length at the site of the two pinholes the visibility of the high-frequency interference also decreases.

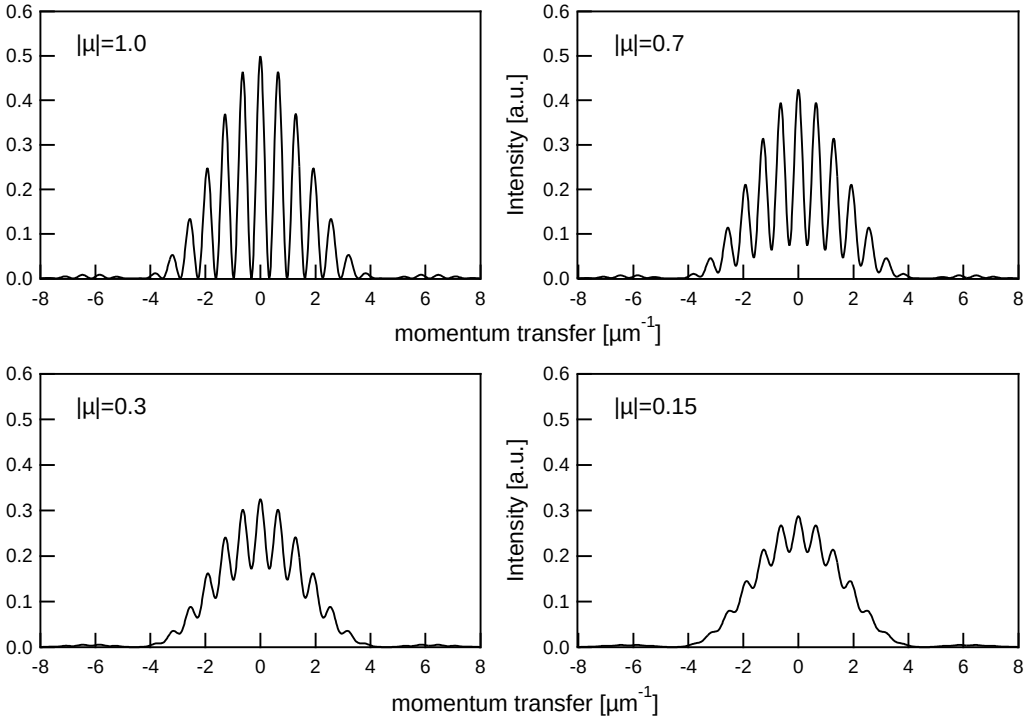

Figure A.4: *Diffraction patterns from a set of two pinholes illuminated from a light source of decreasing degree of coherence* $1.0 \geq |\mu| \geq 0.15$.

Appendix B

$CoPt$ multilayer

The main property of the $CoPt$ multilayer systems is their magnetic anisotropy to be perpendicular to the layer surface [41, 43, 69]. To reduce magnetostatic energy this magnetic films form stripe domains of characteristic width which is determined by the film thickness. The structure of the domains is influenced by their magnetic field history and a perpendicular applied field causes a labyrinth of worm-like domains with random orientation (cp. Fig. B.1). The average domain width of the aligned state is smaller than for the labyrinth state [43].

To allow transmission experiments the $CoPt$ multilayers are sputtered onto a transparent SiN membrane coated on a Si-wafer. The wafer is provided with a etched facet forming a μm^2-size aperture. Typically, an 200 Å underlayer of Pt is applied before the actual $CoPt$ multilayer stack is sputtered. For most experiments presented in this thesis the Co layer has a thickness of 30 Å and the Pt layer is 7 Å thick. Finally, a 20 Å Pt caplayer protects the stack from oxidation [43]. A sketch of a typical sample is shown in Fig. B.1.

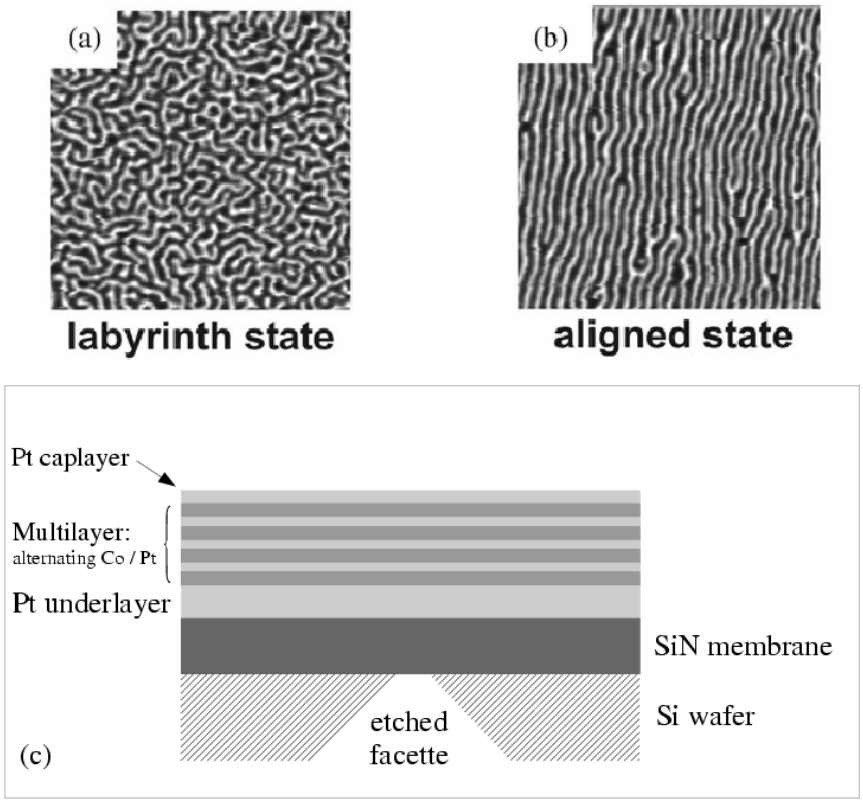

Figure B.1: *(a) Labyrinth and (b) aligned state of the magnetic CoPt domains. The images are taken by magnetic force microscopy (MFM) [43]. (c) Sketch of the CoPt sample layer stack. A Si wafer is etched to form the facet. The SiN membrane is coated onto the wafer, thus, allowing transmission at the facet site. Typically, a Pt underlayer is applied followed by alternating layers of Co and Pt. Finally, the multilayer is capped by a thin Pt film [43].*

Appendix C

Experimental devices

C.1 The UE56-1/SGM beamline setup at BESSY

The Research Center Jülich has built an own beamline branch at the BESSY II synchrotron facility. The radiation source is a helical undulator with a magnet period of 56 mm and 30 of such magnet pairs. The two rows of magnets can be shifted against each other to provide linear polarization vertically and horizontally to the storage ring plane as well as circular polarized x-rays (see Fig. C.1). A switching mirror unit (SMU) at 17 m downstream of the undulator allows to select which branch of the two possible beamline branches is fed with the undulator radiation (see Fig. C.1). The monochromator unit consists of an entrance slit, the grating stage and an exit slit. The VFM focusses the source radiation onto the entrance slit and the spherical monochromator grating focusses the beam to the exit slit.

C.2 The Micro-Channel Plate Detector

The position sensitive micro-channel plate (MCP) detector that has been used for the experiments is a 3300 MCP/RAE Sensor operated with a Position Anaylzer Model 2401[1]. The detector is sensitive to single-event counting of charged-particles and (EUV, soft X-ray) photons. A photon conversion plate coated with CsI initiates the electron cascade that is amplified in the MCPs. We used the 5 channel-plate option for the detector that allows for 400×400 resolvable elements across the 40 $mm \times 40$ mm active area of the resistive anode (RAE). The position is calculated by measuring the ratio of the charge pulse amplitude at the four edges of the anode plate.

Two consecutive events can be separated by the detector system if they occur with a time lag of at least the effective dead time of 10 μsec (see Fig. C.3). The advantage of this type of detector is the fast acquisition time with single-event counting. It can also be used as total yield detecotr to allows for fluorescence spectroscopy experiments. The transmission and scattering spectra presented in this work are acquired in the corresponding total yield mode.

An disadvantage is the relatively low spatial resolution. Furthermore, the electronic system can generate distortion of the measured spatial intensity distribution by possible errorneous calculation of the spatial position of each event. Also the detector system including the channel plates and the CsI photon conversion plate are very sensitive to humidity and excessive intensity of radiation. Both can rapidly destroy the detection capabilities.

C.3 The Charge-Coupled Device Camera

The CCD camera[2] used for the experiments is a Princeton Instruments device, model *PI•SX:2048*. The camera chip is of Marconi CCD42-40 type. It is back-illuminated and sensitive to (soft) x-rays with a quantum efficiency of 80% for 800 eV photons. The chip provides 2048×2048 pixels of $13.5\ \mu m \times 13.5\ \mu m$

[1] All specifications from: www.quantar.com

[2] The reference for all camera specifications is: www.roperscientific.com

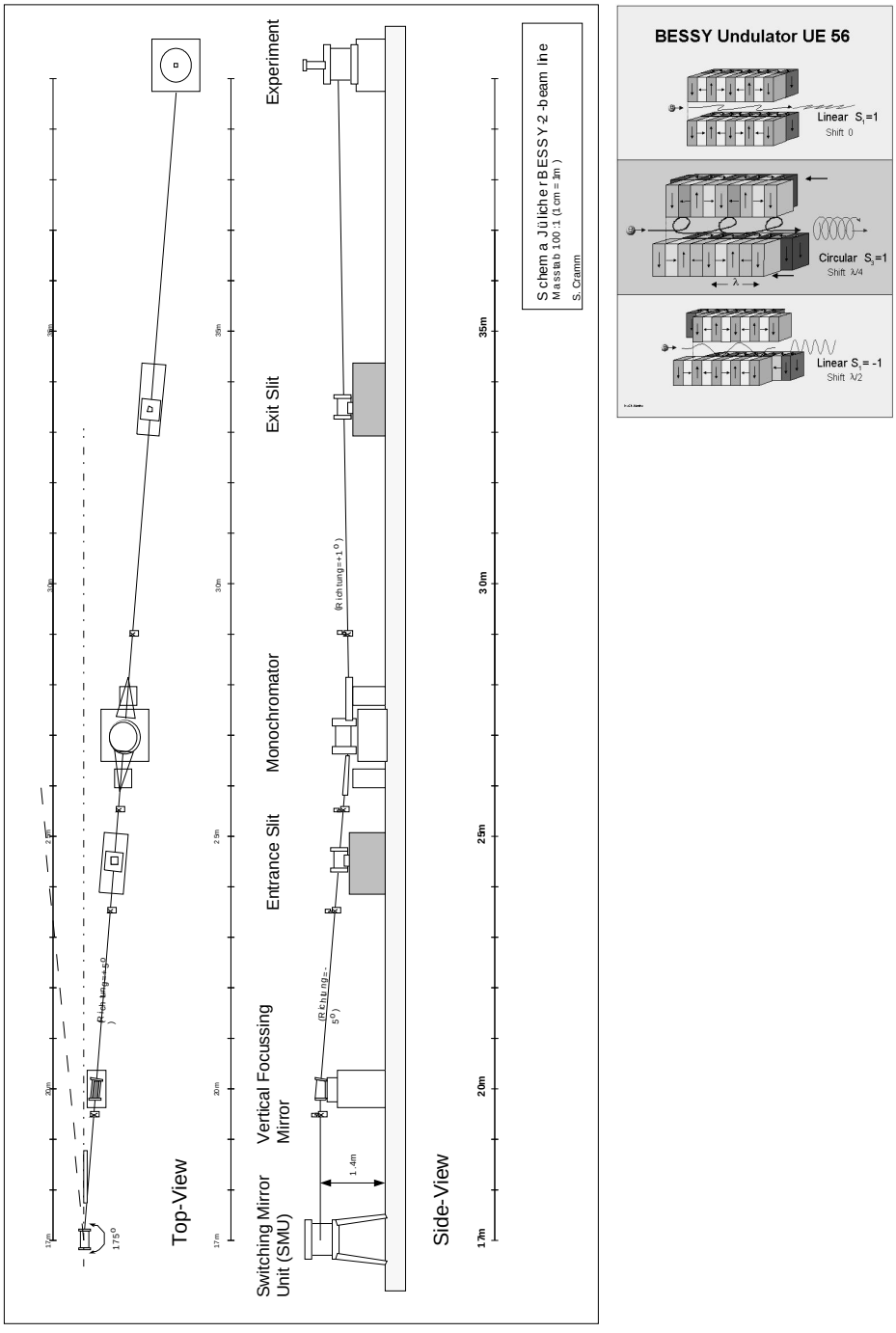

Figure C.1: *Scheme of the UE56/1 SGM beamline of BESSY II. The distances on the scale are given with respect to the site of the undulator. Courtesy of S. Cramm, Research Center Jülich. The small image shows a scheme of the modes of the UE56/1 undulator at BESSY II. It provides horizontal and vertical linear polarization as well as circular polarization. The image is taken from BESSY information pages on www.bessy.de.*

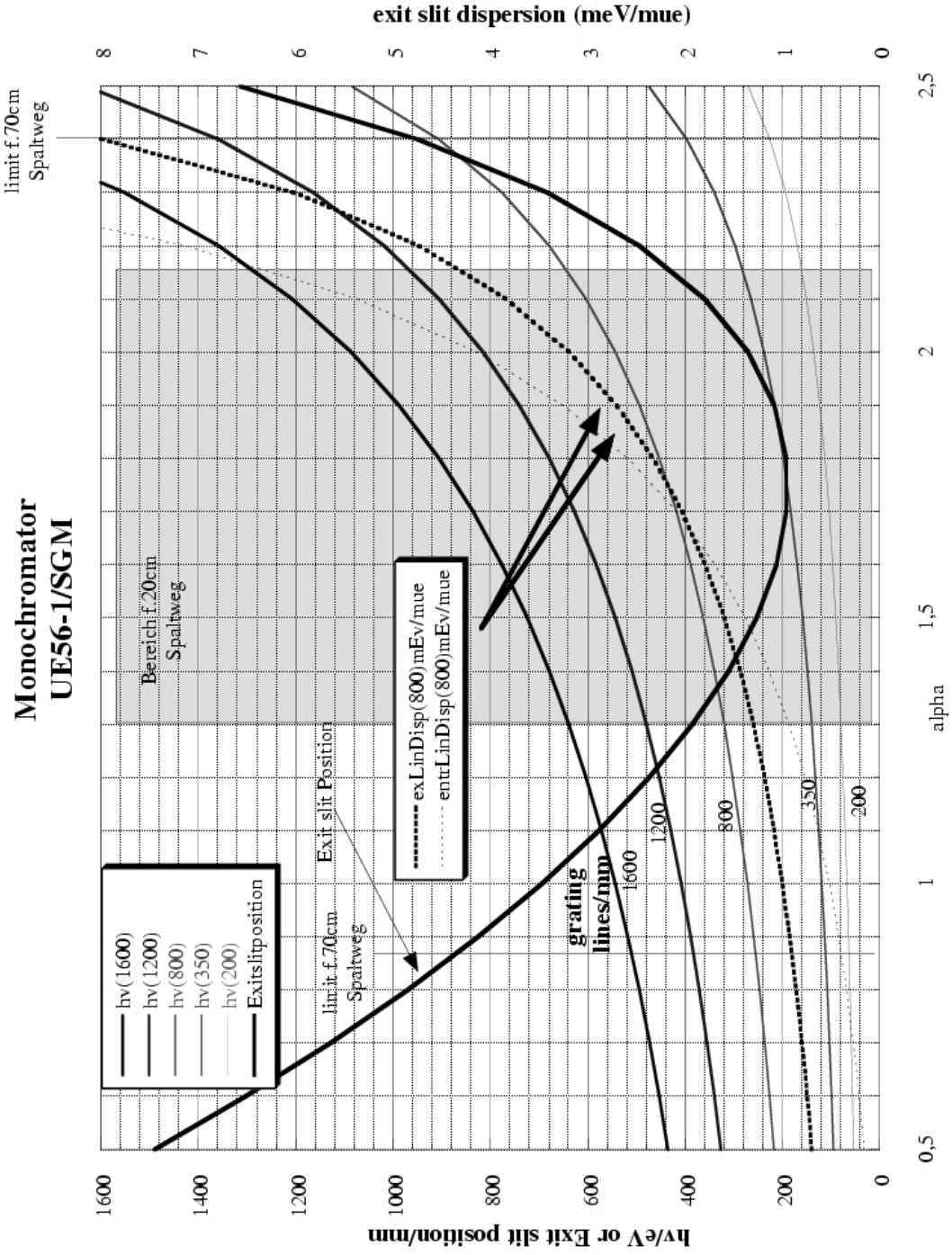

Figure C.2: *Dispersion of the monochromator of beamline UE56/1 SGM at BESSY II. "alpha" is the incident angle of the beam on the monochromator grating. From the left axis the desired energy of the photons is read. For the corresponding energy the angle "alpha" can be determined for each grating. With the value of "alpha" of the illuminated grating the slit dispersion in meV/μm can be extracted from the dotted lines. Courtesy of S. Cramm, FZJ.*

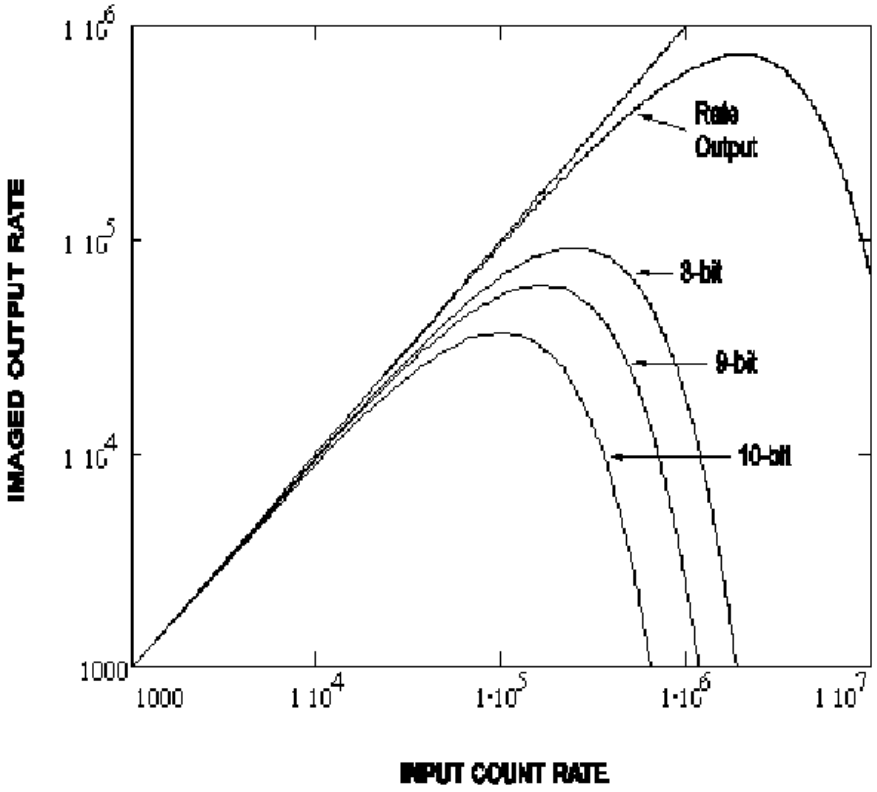

Figure C.3: *Input rate (counts per second in Hz) versus output rate of the* 5 *micro channel plate detector with* 10 *bit analog-digital converts (ADC). At* 10^5 Hz *the detector dead time limits the time-lag between two consecutive events. Image is taken from www.quantar.com.*

size. The dynamic range is 16 *bit* digitization. To reduce noise the chip is thermo-electrically cooled to $-75°C$ with a dark current of 14 electrons per pixel and hour.

The camera is mounted on a $CF63$ conflat flange permitting high vacuum experiments. Data acquisition is realized using an external controller unit and PRINCETON INSTRUMENTS computer software.

Appendix D

The matrix formalism of the state of polarization

D.1 Stokes-Vector and Poincaré's representation of polarization

The basic idea of POINCARÉ's representation for the polarization is to create a cartesian system with the STOKES parameter P_1, P_2 and P_3 as coordinates
[1]

([10,70]). The resulting vector $\mathbf{P}$ is called the *polarization vector*. Its length represents the degree of polarization, *i.e.* for $\mathbf{P} = 0$ the light is completely unpolarized and fully polarized light yields to $\mathbf{P} = 1$. The three parameters describe each a different state of polarization with respect to the scattering plane (Fig. D.1).

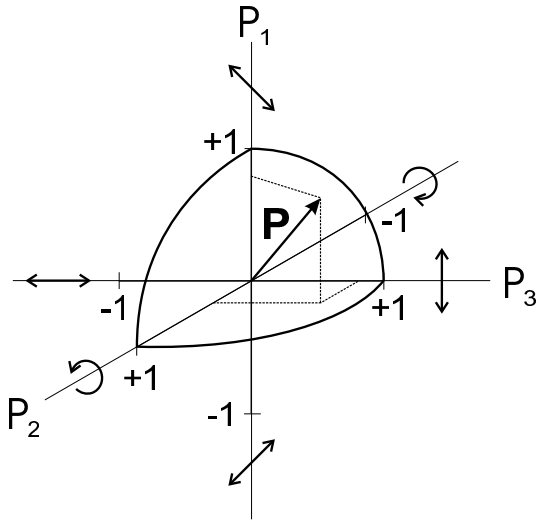

Figure D.1: *The Poincaré sphere. The polarization is completely described by the Stokes parameter P_1,P_2 and P_3, and by definition $|\mathbf{P}| \leq 1$. [33]*

P_3 represents the perpendicular or σ ($P_3 = +1$) and parallel or π ($P_3 = -1$) component of the polarization regarding the scattering plane. P_2 stands for the circular polarization. Completely right-circular polarized light yields to $P_2 = +1$ whereas completely left-circular polarized light yields to $P_2 = -1$. The first parameter describes the contribution of 45°-linear polarization.

[1] It shall be emphasized that the three coordinate axes do not correspond to real-space directions.

Now, let us consider what happens to the polarization vector $\mathbf{P}$ if linear polarized light interacts with a magnetized sample ([70]). The sample shall be characterized by a filter-matrix $\tilde{\mathbf{F}}$[2]. It takes into account the asymmetry of absorption A and the difference in phase velocity ϵ for right- and left-circular polarized light. Both variables are depending on the path length of the light through the sample. The linear polarized light is described by a superposition of two partial waves with opposite helicity and its polarization vector is: $\mathbf{P} = (0, 0, 1)$. The resulting polarization is:

$$\mathbf{P}' = (\sqrt{1 - A^2}\sin\epsilon, A, \sqrt{1 - A^2}\cos\epsilon).$$

It is instructive to consider the case where the asymmetry vanishes $A = 0$. Then the polarization precesses in the (P_1, P_3)-plane: $\mathbf{P}' = (\sin\epsilon, 0, \cos\epsilon)$. The state of polarization remains linear and the plane of polarization rotates. Now, we assume that there is no different phase velocity, $\epsilon = 0$ and the asymmetry is maximum, $A \to 1$. Then the resulting vector is $\mathbf{P}' = (0, 1, 0)$, *i.e.* the light is perfectly circular polarized after the interaction.

In general, both asymmetry and different phase velocities apply. Thus, during the interaction with the magnetic sample the polarization moves from the plane of linear polarization to the pole of circular polarization describing a spiral. Between the "linear" plane and the pole of the POINCARÉ-sphere the vector $\mathbf{P}$ represents elliptical polarized light. As a result, both effects, for example, FARADAY rotation and an increasing elliptical component of the light polarization can be recognized.

D.2 Density Matrix

To make easy the calculation of the polarization depending cross-section we use the formalism of the density matrix μ [10,33]. In a short way, the necessary equations shall be proposed here.

The density matrix is a 2×2-matrix and represents all states of polarization if written as:

$$\mu = \frac{1}{2}(\mathbf{1} + \mathbf{P}\cdot\sigma), \tag{D.1}$$

where $\mathbf{1}$ is the unit matrix, $\mathbf{P}$ the polarization vector (cp. Fig.D.1) and σ represents the Pauli matrices: $\sigma_1 = \begin{pmatrix} 0 & 1 \\ 1 & 0 \end{pmatrix}$, $\sigma_2 = \begin{pmatrix} 0 & -i \\ i & 0 \end{pmatrix}$ and $\sigma_3 = \begin{pmatrix} 1 & 0 \\ 0 & -1 \end{pmatrix}$. This defines μ,

$$\mu = \frac{1}{2}\begin{pmatrix} 1 + P_3 & P_1 - iP_2 \\ P_1 + iP_2 & 1 - P_3 \end{pmatrix}. \tag{D.2}$$

The polarization $\mathbf{P}$ can be calculated by

$$\mathbf{P} = tr(\sigma\mu) \tag{D.3}$$

namely

$$P_1 = tr(\sigma_1\mu) \tag{D.4}$$
$$P_2 = tr(\sigma_2\mu) \tag{D.5}$$
$$P_3 = tr(\sigma_3\mu). \tag{D.6}$$

If the state of polarization of the radiation, $|\psi\rangle$ is known within a probability p then the expectation value of a matrix operator $\tilde{\mathbf{M}}$ is [33]:

$$\left\langle \psi \left| \tilde{\mathbf{M}} \right| \psi \right\rangle = tr(\mu\tilde{\mathbf{M}}) \tag{D.7}$$

The scattering cross-section $\frac{d\sigma}{d\Omega} = |f|^2$ can then be calculated by [10,33]:

[2] for details see [70]

$$\frac{d\sigma}{d\Omega} = tr(\tilde{\mathbf{M}}\mu\tilde{\mathbf{M}}^{\dagger}). \tag{D.8}$$

Finally, the new polarization with eqn. (D.3) is

$$\frac{d\sigma}{d\Omega}P' = tr(\sigma\mu'), \tag{D.9}$$

where $\mu' = \tilde{\mathbf{M}}\mu\tilde{\mathbf{M}}^{\dagger}$.

D.3 Derivation of matrix representation of the polarization dependent scattering factor

It is very common to describe the state of polarization in a basis of two orthogonal vectors $\hat{\mathbf{e}}_\sigma$ and $\hat{\mathbf{e}}_\pi$. $\hat{\mathbf{e}}_\sigma$ is perpendicular to the scattering plane spanned by the initial and final wavevector $\hat{\mathbf{q}}$ and $\hat{\mathbf{q}}'$, respectively (cp. Fig. 2.1), while $\hat{\mathbf{e}}_\pi$ lies in this plane. In this basis it is possible to write eqn. (2.4) in a matrix-form as proposed by DE BERGEVIN and BRUNEL ([2])

$$\hat{\mathbf{e}}' \cdot \hat{\mathbf{e}} = \begin{pmatrix} \hat{\mathbf{e}}'_\sigma \cdot \hat{\mathbf{e}}_\sigma & \hat{\mathbf{e}}'_\sigma \cdot \hat{\mathbf{e}}_\pi \\ \hat{\mathbf{e}}'_\pi \cdot \hat{\mathbf{e}}_\sigma & \hat{\mathbf{e}}'_\pi \cdot \hat{\mathbf{e}}_\pi \end{pmatrix} \tag{D.10}$$

An equivalent expression is given for $\hat{\mathbf{e}}' \times \hat{\mathbf{e}}$. With this form we have an easy representation for the 4 possible scattering channels:

$$\begin{pmatrix} \sigma \to \sigma & \pi \to \sigma \\ \sigma \to \pi & \pi \to \pi. \end{pmatrix} \tag{D.11}$$

The chosen geometry (Fig. 2.1) causes $\hat{\mathbf{e}}_\sigma$ and $\hat{\mathbf{e}}'_\sigma$ to be always parallel, thus: $\hat{\mathbf{e}}'_\sigma \cdot \hat{\mathbf{e}}_\sigma = 1$, $\hat{\mathbf{e}}'_\sigma \times \hat{\mathbf{e}}_\sigma = 0$. The two in-plane vectors enclose an angle of $\theta + \theta'$. Finally, some geometric considerations lead to [10,32]:

$$\begin{aligned} f_n^{res} &= \frac{3}{4q}\left\langle \begin{pmatrix} 1 & 0 \\ 0 & \hat{\mathbf{q}} \cdot \hat{\mathbf{q}}' \end{pmatrix} \right\rangle [F^1_{+1} + F^1_{-1}] \\ &\quad -i\frac{3}{4q}\left\langle \begin{pmatrix} 0 & \hat{\mathbf{q}} \\ -\hat{\mathbf{q}}' & \hat{\mathbf{q}}' \times \hat{\mathbf{q}} \end{pmatrix} \right\rangle \cdot \hat{\mathbf{m}}_n [F^1_{+1} - F^1_{-1}]. \end{aligned} \tag{D.12}$$

$\hat{\mathbf{m}}_n = (m_1, m_2, m_3)$ is the direction of the magnetization. Let us introduce matrix operators for the charge and magnetic term,

$$\left\langle \tilde{\mathbf{M}}_c \right\rangle = \left\langle \begin{pmatrix} 1 & 0 \\ 0 & \cos\theta' \end{pmatrix} \right\rangle F^{(0)} \tag{D.13}$$

$$\left\langle \tilde{\mathbf{M}}_m \right\rangle = -i\left\langle \begin{pmatrix} 0 & m_3 \\ -m_1 * \sin\theta' - m_3 * \cos\theta' & -m_2 \sin\theta' \end{pmatrix} \right\rangle F^{(1)}, \tag{D.14}$$

where the $\hat{\mathbf{q}}$ and $\hat{\mathbf{q}}'$ terms are evaluated using the transmission scattering geometry in Fig. 2.1 and the abbreviations $F^{(0)} = [F^1_{+1} + F^1_{-1}]$ and $F^{(1)} = [F^1_{+1} - F^1_{-1}]$ are used. Then eqn. (D.12) can be written in a compact form,

$$f_n^{res} = \frac{3}{4q}\left(\left\langle \tilde{\mathbf{M}}_c \right\rangle + \left\langle \tilde{\mathbf{M}}_m \right\rangle\right). \tag{D.15}$$

Shall ϵ_σ and ϵ_π be a 2-dimensional basis of linear polarized light. Then $\epsilon_\sigma = \begin{pmatrix} 1 \\ 0 \end{pmatrix}$ represents perpendicular and $\epsilon_\pi = \begin{pmatrix} 0 \\ 1 \end{pmatrix}$ represents parallel polarization with respect to the scattering plane. A linear combination of the basis vectors allows to define the state of polarization: $|\psi\rangle = \mu_1 \begin{pmatrix} 1 \\ 0 \end{pmatrix} + \mu_2 \begin{pmatrix} 0 \\ 1 \end{pmatrix}$. Now, we can easily calculate the contribution of each partial wave to the scattering process.

Let us assume the polarization to be perpendicular to the scattering plane, thus: $|\psi\rangle = \begin{pmatrix} 1 \\ 0 \end{pmatrix}$. Furthermore, a polarization filter allows to select the same partial wave after the scattering process, *i.e.* we have $\sigma \rightarrow \sigma'$ scattering. Now the scattering cross-section $\frac{d\sigma}{d\Omega} = \left|\langle\psi'| \sum_n e^{i\mathbf{Q}\mathbf{r}_n} f_n |\psi\rangle\right|^2$ reduces to:

$$\frac{d\sigma}{d\Omega} = \left(\frac{3}{4q}\right)^2 \left|\sum_n e^{i\mathbf{Q}\mathbf{r}_n} [F^1_{+1} + F^1_{-1}]\right|^2 . \tag{D.16}$$

The scattered intensity is only depending on the charge term and the magnetization of the sample is not involved in the process.

Now, the polarization analyzer shall be turned to detect the π-light, only. For $\sigma \rightarrow \pi$ scattering we get:

$$\frac{d\sigma}{d\Omega} = \left(\frac{3}{4q}\right)^2 \left|\sum_n e^{i\mathbf{Q}\mathbf{r}_n} \left(\hat{\mathbf{q}}' \cdot \hat{\mathbf{m}}_n\right) [F^1_{+1} - F^1_{-1}]\right|^2 . \tag{D.17}$$

This time the charge scattering is surpressed and *magnetic* scattering can be observed.

D.3.1 Applying the density matrix

The scattering cross-section for known states of polarization before and after the scattering process

$$\frac{d\sigma}{d\Omega} = \left|\left\langle \psi'| \sum_n e^{i\mathbf{Q}\mathbf{r}_n} f_n^{res} |\psi \right\rangle\right|^2$$

may be transformed with eqn.(D.7), (D.8) and (D.12)into:

$$\begin{aligned}
\frac{d\sigma}{d\Omega} &= \left(\frac{3}{4q}\right)^2 tr \left(\sum_n e^{i\mathbf{Q}\mathbf{r}_n} \right. \\
&\quad \left. \left\{ \left\langle \tilde{\mathbf{M}}_c + \tilde{\mathbf{M}}_m \right\rangle \mu \left\langle \tilde{\mathbf{M}}_c + \tilde{\mathbf{M}}_m \right\rangle^\dagger \right\} \right) \\
&= \left(\frac{3}{4q}\right)^2 tr \left(\sum_n e^{i\mathbf{Q}\mathbf{r}_n} \right. \\
&\quad \left\{ \left\langle \tilde{\mathbf{M}}_c \right\rangle \mu \left\langle \tilde{\mathbf{M}}_c^\dagger \right\rangle + \left\langle \tilde{\mathbf{M}}_m \right\rangle \mu \left\langle \tilde{\mathbf{M}}_m^\dagger \right\rangle \right. \\
&\quad \left. \left. + \left\langle \tilde{\mathbf{M}}_m \right\rangle \mu \left\langle \tilde{\mathbf{M}}_c^\dagger \right\rangle + \left\langle \tilde{\mathbf{M}}_c \right\rangle \mu \left\langle \tilde{\mathbf{M}}_m^\dagger \right\rangle \right\} \right) .
\end{aligned} \tag{D.18}$$

The first and second term represent the charge and pure magnetic scattering, respectively. The last two terms describe the interference of charge and magnetic scattering.

Bibliography

[1] M. Brunel and F. DeBergevin, "Diffraction of x-rays by magnetic materials .2. measurements on anti-ferromagnetic fe2o3," *Acta Crystallographica Section A*, vol. 37, no. May, pp. 324–331, 1981.

[2] F. DeBergevin and M. Brunel, "Diffraction of x-rays by magnetic materials .i. general formulas and measurements on ferromagnetic and ferrimagnetic compounds," *Acta Crystallographica Section A*, vol. 37, no. May, pp. 314–324, 1981.

[3] B. T. Thole, G. Vanderlaan, and G. A. Sawatzky, "Strong magnetic dichroism predicted in the m4,5 x-ray absorption-spectra of magnetic rare-earth materials," *Physical Review Letters*, vol. 55, no. 19, pp. 2086–2088, 1985.

[4] J. P. Hannon, G. T. Trammell, M. Blume, and D. Gibbs, "X-ray resonance exchange scattering," *Physical Review Letters*, vol. 61, pp. 1245–1248, SEP 5 1988.

[5] G. Schutz, W. Wagner, W. Wilhelm, P. Kienle, R. Zeller, R. Frahm, and G. Materlik, "Absorption of circularly polarized x-rays in iron," *Physical Review Letters*, vol. 58, pp. 737–740, FEB 16 1987.

[6] C. Kao, J. B. Hastings, E. D. Johnson, D. P. Siddons, G. C. Smith, and G. A. Prinz, "Magnetic-resonance exchange scattering at the iron lii and liii edges," *Physical Review Letters*, vol. 65, pp. 373–376, JUL 16 1990.

[7] G. Vanderlaan and B. T. Thole, "Strong magnetic x-ray dichroism in 2p absorption-spectra of 3d transition-metal ions," *Physical Review B*, vol. 43, pp. 13401–13411, JUN 1 1991.

[8] C. C. Kao, C. T. Chen, E. D. Johnson, J. B. Hastings, H. J. Lin, G. H. Ho, G. Meigs, J. M. Brot, S. L. Hulbert, Y. U. Idzerda, and C. Vettier, "Dichroic interference effects in circularly polarized soft x-ray resonant magnetic scattering," *Physical Review B*, vol. 50, pp. 9599–9602, OCT 1 1994.

[9] J. Stohr, "X-ray magnetic circular dichroism spectroscopy of transition metal thin films," *Journal of Electron Spectroscopy and Related Phenomena*, vol. 75, pp. 253–272, DEC 15 1995.

[10] S. Lovesey and S. Collins, *X-Ray Scattering and Absorption by Magnetic Materials*. Oxford series on synchrotron radiation, Oxford University Press Inc., New York, 1996.

[11] J. Stohr and R. Nakajima, "Magnetic properties of transition metal multilayers studied with x-ray magnetic circular dichroism spectroscopy," *IBM Journal of Research and Development*, vol. 42, pp. 73–88, Jan. 1998.

[12] J. W. Freeland, V. Chakarian, K. Bussmann, Y. U. Idzerda, H. Wende, and C.-C. Kao, "Exploring magnetic roughness in cofe thin films," *Journal of Applied Physics*, vol. 83, no. 11, pp. 6290–6292, 1998.

[13] H. A. Durr, E. Dudzik, S. S. Dhesi, J. B. Goedkoop, G. van der Laan, M. Belakhovsky, C. Mocuta, A. Marty, and Y. Samson, "Chiral magnetic domain structures in ultrathin fepd films," *Science*, vol. 284, pp. 2166–2168, JUN 25 1999.

[14] J. B. Kortright, S. K. Kim, G. P. Denbeaux, G. Zeltzer, K. Takano, and E. E. Fullerton, "Soft-x-ray small-angle scattering as a sensitive probe of magnetic and charge heterogeneity," *Physical Review B*, vol. 6409, pp. art. no.–092401, SEP 1 2001.

[15] K. Chesnel, M. Belakhovsky, S. Landis, J. C. Toussaint, S. P. Collins, G. van der Laan, E. Dudzik, and S. S. Dhesi, "X-ray resonant magnetic scattering study of the magnetic coupling in co/pt nanolines and its evolution under magnetic field," *Physical Review B*, vol. 66, JUL 1 2002.

[16] A. Rahmim, S. Tixier, T. Tiedje, S. Eisebitt, M. Lorgen, R. Scherer, W. Eberhardt, J. Luning, and A. Scholl, "Interference between magnetism and surface roughness in coherent soft x-ray scattering," *Physical Review B*, vol. 65, pp. art. no.–235421, JUN 15 2002.

[17] C. Spezzani, P. Torelli, M. Sacchi, R. Delaunay, C. F. Hague, F. Salmassi, and E. M. Gullikson, "Hysteresis curves of ferromagnetic and antiferromagnetic order in metallic multilayers by resonant x-ray scattering," *Physical Review B*, vol. 66, pp. art. no.–052408, AUG 1 2002.

[18] D. T. Attwood, *Soft x-rays and extreme ultraviolet radiation : principles and applications*. Cambridge, U.K. ; New York : Cambridge University Press, 2000.

[19] B. Lengeler, "Coherence in x-ray physics," *Naturwissenschaften*, vol. 88, pp. 249–260, June 2001.

[20] M. Born and E. Wolf, *Principles of Optics*. Pergamon Press, Oxford, 1959.

[21] G. Denbeaux, P. Fischer, G. Kusinski, M. Le Gros, A. Pearson, and D. Attwood, "A full field transmission x-ray microscope as a tool for high-resolution magnetic imaging," *Ieee Transactions on Magnetics*, vol. 37, no. 4, p. 2764, 2001.

[22] J. Goodman, *Laser speckle and related phenomena*. Topics in applied physics, Springer, 2nd, enlarged ed. ed., 1984.

[23] D. L. Abernathy, G. Grubel, S. Brauer, I. McNulty, G. A. Stephenson, S. G. J. Mochrie, A. R. Sandy, N. Mulders, and M. Sutton, "Small-angle x-ray scattering using coherent undulator radiation at the esrf," *Journal of Synchrotron Radiation*, vol. 5, pp. 37–47, JAN 1 1998.

[24] O. K. C. Tsui, S. G. J. Mochrie, and L. E. Berman, "Statistical analysis of x-ray speckle at the nsls," *Journal of Synchrotron Radiation*, vol. 5, pp. 30–36, JAN 1 1998.

[25] W. Weber and B. Lengeler, "Diffuse scattering of hard x-rays from rough surfaces," *Physical Review B*, vol. 46, pp. 7953–7956, SEP 15 1992.

[26] T. Salditt, H. Rhan, T. H. Metzger, J. Peisl, R. Schuster, and J. P. Kotthaus, "X-ray coherence and ultra-small angle resolution at grazing-incidence and exit angles," *Zeitschrift fur Physik B - Condensed Matter*, vol. 96, pp. 227–230, Dec. 1994.

[27] M. Adamcyk, S. Eisebitt, A. Karl, C. Nicoll, T. Pinnington, R. Scherer, T. Tiedje, and W. Eberhardt, "Surface roughness and resonant scattering effects in soft x-ray speckle from random semiconductor interfaces," *Surface Review and Letters*, vol. 6, no. 6, p. 1121, 1999.

[28] D. L. Abernathy, J. Nielsen, S. B. Dierker, R. M. Fleming, G. Grubel, R. Pindak, K. Ploog, and I. K. Robinson, "1d x-ray speckle patterns: A novel probe of interfacial disorder in semiconductor superlattices," *Solid-State Electronics*, vol. 40, no. 1-8, pp. 531–535, 1996.

[29] J. L. Libbert, R. Pindak, S. B. Dierker, and I. K. Robinson, "Speckle in coherent x-ray reflectivity from si(111) wafers," *Physical Review B*, vol. 56, pp. 6454–6457, SEP 15 1997.

[30] M. Blume, "Magnetic scattering of x-rays," *Journal of Applied Physics*, vol. 57, no. 8, pp. 3615–3618, 1985.

[31] J. Stohr, Y. Wu, B. D. Hermsmeier, M. G. Samant, G. R. Harp, S. Koranda, D. Dunham, and B. P. Tonner, "Element-specific magnetic microscopy with circularly polarized x-rays," *Science*, vol. 259, pp. 658–661, JAN 29 1993.

[32] J. P. Hill and D. F. McMorrow, "X-ray resonant exchange scattering: Polarization dependence and correlation functions," *Acta Crystallographica Section A*, vol. 52, pp. 236–244, MAR 1 1996.

[33] M. Blume and D. Gibbs, "Polarization dependence of magnetic-x-ray scattering," *Physical Review B*, vol. 37, pp. 1779–1789, FEB 1 1988.

[34] J. B. Kortright and S. K. Kim, "Resonant magneto-optical properties of fe near its 2p levels: Measurement and applications," *Physical Review B*, vol. 62, pp. 12216–12228, NOV 1 2000.

[35] H. C. Mertins, F. Schafers, X. Le Cann, A. Gaupp, and W. Gudat, "Faraday rotation at the 2p edges of fe, co, and ni," *Physical Review B*, vol. 61, pp. R874–R877, JAN 1 2000.

[36] H. C. Mertins, O. Zaharko, A. Gaupp, F. Schafers, D. Abramsohn, and H. Grimmer, "Soft x-ray magneto-optical constants at the fe 2p edge determined by bragg scattering and faraday effect," *Journal of Magnetism and Magnetic Materials*, vol. 240, pp. 451–453, Feb. 2002.

[37] M. J. Freiser, "A survey of magnetooptic effects," *IEEE Transactions on Magnetics*, vol. MAG4, no. 2, p. 152, 1968.

[38] J. Stohr, H. A. Padmore, S. Anders, T. Stammler, and M. R. Scheinfein, "Principles of x-ray magnetic dichroism spectromicroscopy," *Surface Review and Letters*, vol. 5, pp. 1297–1308, Dec. 1998.

[39] J. Stöhr, *NEXAFS spectroscopy*, vol. 25 of *Springer series in surface sciences*. Springer, 1992.

[40] J. F. MacKay, C. Teichert, D. E. Savage, and M. G. Lagally, "Element specific magnetization of buried interfaces probed by diffuse x-ray resonant magnetic scattering," *Physical Review Letters*, vol. 77, pp. 3925–3928, OCT 28 1996.

[41] J. B. Kortright, O. Hellwig, D. T. Margulies, and E. E. Fullerton, "Resolving magnetic and chemical correlations in coptcr films using soft x-ray resonant scattering," *Journal of Magnetism and Magnetic Materials*, vol. 240, pp. 325–330, Feb. 2002.

[42] S. Eisebitt, M. Lörgen, W. Eberhardt, J. Lüning, J. Stöhr, C. Rettner, O. Hellwig, E. Fullerton, and G. Denbeaux, "Polarization effects in coherent scattering from magnetic specimen: Implications for x-ray holography, lensless imaging and correlation spectroscopy," *Physical Review B*, vol. 68, no. 10, p. 104419, 2003.

[43] O. Hellwig, G. P. Denbeaux, J. B. Kortright, and E. E. Fullerton, "X-ray studies of aligned magnetic stripe domains in perpendicular multilayers," *Physica B - Condensed Matter*, vol. 336, pp. 136–144, Aug. 2003.

[44] O. Hellwig and E. Fullerton, "Sample design and preparation, ibm corp., almaden research center, 650 harry rd, san jose, ca-95120."

[45] S. K. Sinha, E. B. Sirota, S. Garoff, and H. B. Stanley, "X-ray and neutron-scattering from rough surfaces," *Physical Review B*, vol. 38, pp. 2297–2311, AUG 1 1988.

[46] C. Rettner, "The pinhole was fabricated by c.t. rettner at ibm corp., almaden research center, 650 harry rd, san jose, ca-95120."

[47] D. Schondelmaier, "Herstellung und Charakterisierung von gekoppelten IrMn/CoFe Schichtsystemen," PhD thesis, University of Cologne, 2003.

[48] M. Lörgen, "Streuung kohärenter weicher Röntgenstrahlung an Magnetischen Schichtsystemen,", Diploma thesis, Research Center Jülich, August 2000.

[49] J. W. Goodman, *Introduction to Fourier optics*. McGraw-Hill series in electrical and computer engineering, New York: McGraw-Hill, 2nd ed. ed., 1996.

[50] R. Gerchberg and W. Saxton, "A practical algorithm for the determination of phase from image and diffraction plane pictures," *Optik*, vol. 35, no. 2, pp. 237–246, 1972.

[51] J. R. Fienup, "Reconstruction of an object from modulus of its fourier-transform," *Optics Letters*, vol. 3, no. 1, pp. 27–29, 1978.

[52] J. N. Cederquist, J. R. Fienup, J. C. Marron, and R. G. Paxman, "Phase retrieval from experimental far-fiels speckle data," *Optics Letters*, vol. 13, pp. 619–621, Aug. 1988.

[53] J. W. Miao, P. Charalambous, J. Kirz, and D. Sayre, "Extending the methodology of x-ray crystallography to allow imaging of micrometre-sized non-crystalline specimens," *Nature*, vol. 400, no. 6742, p. 342, 1999. Times Cited: 28 Article English Cited References Count: 20 219ch.

[54] J. Pitney, I. Vartaniants, and I. Robinson, "Phase retrieval in coherent diffraction from cu3au antiphase domains," *Digital Image Recovery and Synthesis IV*, vol. 3815, pp. 199–207, 1999.

[55] I. K. Robinson, I. A. Vartanyants, G. J. Williams, M. A. Pfeifer, and J. A. Pitney, "Reconstruction of the shapes of gold nanocrystals using coherent x-ray diffraction," *Physical Review Letters*, vol. 87, no. 19, p. 195505, 2001.

[56] I. A. Vartanyants and I. K. Robinson, "Partial coherence effects on the imaging of small crystals using coherent x-ray diffraction," *Journal of Physics-Condensed Matter*, vol. 13, no. 47, p. 10593, 2001.

[57] J. Miao, T. Ohsuna, O. Terasaki, K. O. Hodgson, and M. A. O'Keefe, "Atomic resolution three-dimensional electron diffraction microscopy," *Physical Review Letters*, vol. 89, no. 15, p. 155502, 2002.

[58] H. He, S. Marchesini, M. Howells, U. Weierstall, G. Hembree, and J. C. H. Spence, "Experimental lensless soft-x-ray imaging using iterative algorithms: phasing diffuse scattering," *Acta Crystallographica Section A*, vol. 59, pp. 143–152, Mar. 2003.

[59] H. He, S. Marchesini, M. Howells, U. Weierstall, H. Chapman, S. Hau-Riege, A. Noy, and J. C. H. Spence, "Inversion of x-ray diffuse scattering to images using prepared objects," *Phys. Rev. B*, vol. 67, p. 174114, 2003.

[60] J. Miao, D. Sayre, and H. N. Chapman, "Phase retrieval from the magnitude of the fourier transforms of nonperiodic objects," *Journal of the Optical Society of America A - Optics Image Science and Vision*, vol. 15, pp. 1662–1669, June 1998.

[61] R. H. T. Bates, "Fourier phase problems are uniquely sslvable in more than one dimension .1. underlying theory," *Optik*, vol. 61, no. 3, pp. 247–262, 1982.

[62] W. R. Fright and R. H. T. Bates, "Fourier phase problems are uniquely solvable in more than one dimension .3. computaional examples for 2 dimensions," *Optik*, vol. 62, no. 3, pp. 219–230, 1982.

[63] U. Weierstall, Q. Chen, J. C. H. Spence, M. R. Howells, M. Isaacson, and R. R. Panepucci, "Image reconstruction from electron and x-ray diffraction patterns using iterative algorithms: experiment and simulation," *Ultramicroscopy*, vol. 90, pp. 171–195, 2002.

[64] S. Eisebitt, M. Loergen, W. Eberhardt, J. Luening, S. Andrews, and J. Stoehr, "A scalable approach for lensless imaging at x-ray wavelengths," *submitted to APL*, 2004.

[65] J. Fienup, "Phase retrieval algorithm - a comparison," *Applied Optics*, vol. 21, no. 15, p. 2758, 1982.

[66] J. R. Fienup and C. C. Wackerman, "Phase retrieval stagnation problems and solutions," *Journal of the Optical Society of America A - Optics Image Science and Vision*, vol. 3, pp. 1897–1907, Nov. 1986.

[67] J. Miao, T. Ishikawa, E. H. Anderson, and K. O. Hodgson, "Phase retrieval of diffraction patterns from noncrystalline samples using the oversampling method," *Physical Review B*, vol. 67, MAY 1 2003.

[68] J. Fienup, "Reconstruction of a complex-valued object from the modulus of its fourier transform using a support constraint.," *J. Opt. Soc. Am. A*, vol. 4, no. 1, pp. 118–123, 1987.

[69] O. Hellwig, S. Maat, J. B. Kortright, and E. E. Fullerton, "Magnetic reversal of perpendicularly-biased co/pt multilayers," *Physical Review B*, vol. 65, APR 1 2002.

[70] H.-C. Siegmann, "Introduction to spin polarized electrons and magnetism." Lecture, 2001.

Publication List

"Streuung kohärenter weicher Röntgenstrahlung an magnetischen Schichtsystemen",
M. Lörgen, Diploma thesis, Forschungszentrum Jülich, August 2000.

"Interference between magnetism and surface roughness in coherent soft x-ray scattering",
A. Rahmim, S. Tixier, T. Tiedje, S. Eisebitt, M. Lörgen, R. Scherer, W. Eberhardt, J. Lüning, and A. Scholl, *Physical Review B*, Vol. 65, pp.235421, 2002.

"Polarization effects in coherent scattering from magnetic specimen: Implications for x-ray holography, lensless imaging and correlation spectroscopy",
S. Eisebitt, M. Lörgen, W. Eberhardt, J. Lüning, J. Stöhr, C. Rettner, O. Hellwig, E. Fullerton, and G. Denbeaux, *Physical Review B*, vol. 68, 2003.

"A scalable approach for lensless imaging at x-ray wavelengths",
S. Eisebitt, M. Lörgen, W. Eberhardt, J. Lüning, S. Andrews, and J. Stöhr,*submitted to APL*, 2004.

Acknowledgement

This work is the result of many experiments, analysis and discussions during the years 2000 to 2003. After my diploma thesis I continued at the Institute of Solid State Research (IFF) of the Research Center Jülich in the group of Prof. Eberhardt. In the year 2001, I had the opportunity to stay at the Stanford Synchrotron Radiation Laboratory in the group of Prof. Stöhr where a lot of theoretical elaboration and planning of a new scattering chamber has been realized. Finally, from 2002 on I was a staff member of BESSY. During the years I met a lot of exciting and excited people to whom I want to express my appreciation.

First, I would like to thank Prof. Wolfgang Eberhardt for enabling to work in his research group both at the Research Center Jülich and later at the Berliner Elektronenspeicherring-Gesellschaft für Synchrotron Strahlung m. b. H. (BESSY). He greatly supported my work during the last years and he found time for many discussions.

Further, I thank Prof. Peter Zimmermann for his kind disposition to read and appraise this thesis.

I appreciate much the invitation by Prof. Joachim Stöhr to visit his exciting group at the Stanford Synchrotron Radiation Laboratory (SSRL). Personally and scientifically it was very fruitful to work within his group and I benefited a lot from discussions with him and his group members last but not least during the friday group meetings.

Very grateful appreciation merits Dr. Stefan Eisebitt for his supervision, his continuous and untiring support in all kinds of questions and problems that eventually came up through the last years. He was always available for fruitful discussions and for carefully reviewing this thesis. It was a great pleasure to work with him and to benefit from his experience.

Special thanks go to Dr. Jan Lüning from SSRL for all the discussions and the support during all the long beamtime sessions. He was always open for questions and ideas concerning the reconstruction how-to. With him I got an idea of 24h-around-the-world work.

Many thanks to Dr. Olav Hellwig for the preparation of the magnetic samples and for making them available almost day and night.

I also appreciate the support by Scott Andrews and William F. Schlotter from SSRL for spending a lot of time on goldfilm fibbing and for the fearless pinhole mask preparation.

Some special thanks go to Dr. Daniel Schondelmaier for spending at least some nights out there in Berlin even though with a slight focus on a weird pub in Friedrichshain. Ah, I almost forgot, there was a beamtime in May 2001: thanks for staying the course with me.

I also would like to express a general thank to everybody of the BESSY staff who facilitated my work by providing technical and administrative support. Without their help a lot of things would have been harder.

I would like to thank my parents for paving my way to university in many respects.
Finally, I am deeply grateful to my wonderful *novia* Claudia Weilbach, for her love and support.